Waveguide-Integrated Germanium Photodetector Design and Optimization for Sensing and Telecom Applications

by

Hasan Fırat Yıldız

A Dissertation Submitted to the
Graduate School of Sciences and Engineering
in Partial Fulfillment of the Requirements for
the Degree of

Master of Science

in

Electrical and Electronics Engineering

KOÇ ÜNİVERSİTESİ

August 18, 2021

Waveguide-Integrated Germanium Photodetector Design and Optimization for Sensing and Telecom Applications

Koç University
Graduate School of Sciences and Engineering

This is to certify that I have examined this copy of a master's thesis by

Hasan Fırat Yıldız

and have found that it is complete and satisfactory in all respects,
and that any and all revisions required by the final
examining committee have been made.

Committee Members:

____
Assist. Prof. Mehmet Cengiz Onbaşlı (Advisor)

____
Assist. Prof. Emir Salih Mağden

____
Assoc. Prof. Onur Ferhanoğlu

Date: August 18, 2021

Dedicated to the two most precious women

Müge Yıldız

and

Ümit Yıldız

ABSTRACT

Waveguide Integrated Germanium Photodetector Design and Optimization for Sensing and Telecom Applications

Hasan Fırat Yıldız

Master of Science in Electrical and Electronics Engineering

August 18, 2021

With the developing technology, electronics has become unable to reach the high speeds and high efficiency required by new applications. Silicon photonic integrated circuit technology has been proposed to solve this problem. As part of silicon photonics, photodetectors are one of the cornerstones of silicon photonics technology. In the early years of silicon photonics, photodetectors were mainly designed for fiber optical telecom applications. Silicon photonics and photodetectors can be used in many other applications such as sensors, cameras, LIDAR, and photovoltaics. In this thesis, geometric optimization of waveguide integrated Ge VPIN photodetectors has been studied. Two different photodetector designs were developed with simulations for two different application types. The first design is a photodetector having ultra-high responsivity ($1.17\ AW^{-1}$) and ultra-low noise ($48.38\ nW$ NEP) at $0V$ bias operation that can be used in optical time domain reflectometer sensor applications. This photodetector adopts a $500\ nm$-thick, $2.5\ \mu m$-wide and $100\ \mu m$-long Ge layer. It has a wide dynamic range ($55.76\ dB$) and could allow for high contrast readout in long-haul OTDR applications. The second photodetector adopts a $300\ nm$-thick, $2\ \mu m$-wide, and $10\ \mu m$-long Ge layer showing a $0.972\ AW^{-1}$ responsivity with a bandwidth of 84.26 GHz at -2V bias. Due to having ultra-high bandwidth, high responsivity, and low dark current ($8.67\ nA$), it could be suitable for state-of-the-art telecom applications such as the 400G-BASE-DR4 ethernet standard. These designs and our design guidelines could pave the way for optimized silicon waveguide-integrated germanium photodetectors with superior and refined performance in sensing, telecom, and imaging applications.

ÖZETÇE

Dalgakılavuzu ile Tümleşik Germanyum Fotodedektörlerin Sensör ve Telekom Uygulamaları için Tasarım ve Optimizasyonu

Hasan Fırat Yıldız

Elektrik ve Elektronik Mühendisliği, Yüksek Lisans

18 Ağustos 2021

Gelişen teknoloji ile birlikte elektronik donanımlar, yeni uygulamaların gerektirdiği yüksek hızlara ve yüksek verimliliğe ulaşamaz hale gelmiştir. Bu problemin çözümü için silikon fotonik tümleşik devre teknolojisi öne sürülmüştür. Bu alanda fotodedektörler silikon fotonik teknolojisinin temel taşlarından biridir. Silikon fotoniğin ilk yıllarında fotodedektörler esas olarak fiber optik telekom uygulamaları için tasarlanmıştır. Silikon fotoniği ve fotodedektörler sensörler, kameralar, LIDAR ve fotovoltaikler gibi başka birçok uygulamada kullanılabilir. Bu tezde, dalgakılavuzu ile tümleşik germanium VPIN fotodedektörlerin geometrik optimizasyonu üzerine çalışılmıştır. İki farklı uygulama alanı için iki farklı fotodedektör tasarımı simülasyonlarla birlikte geliştirilmiştir. İlk tasarım, optik zaman alanında yansıtıcı sensör uygulamalarında kullanılabilen, 0V gerilimli çalışmada ultra yüksek duyarlılığa ($1.17\,AW^{-1}$) ve ultra düşük gürültüye ($48.38\,nW$ NEP) sahip bir fotodedektördür. Bu fotodedektör, $500\,nm$ kalınlığında, $2.5\,\mu m$ genişliğinde ve $100\,\mu m$ uzunluğunda bir Ge katmanına sahiptir. Geniş bir dinamik aralığa ($55.76\,dB$) sahiptir ve uzun mesafeli OTDR uygulamalarında yüksek kontrastlı okumaya izin verebilir. İkinci fotodetektör, -2V ters gerilimde $84.26\,GHz$ bantgenişliği ile $0.972\ AW^{-1}$ duyarlılığı gösteren $300\,nm$ kalınlığında, $2\,\mu m$ genişliğinde ve $10\,\mu m$ uzunluğunda Ge katmanına sahiptir. Ultra yüksek bant genişliğine, yüksek duyarlılığa ve düşük karanlık akıma ($8.67\,nA$) sahip olması nedeniyle, 400G-BASE-DR4 ethernet standardı gibi son teknoloji telekom uygulamaları için uygundur. Bu tasarımlar ve tasarım yönergelerimiz, sensör, telekom ve görüntüleme uygulamalarında üstün ve rafine performansa sahip, optimize edilmiş silikon dalga kılavuzu ile entegre germanyum fotodedektörlerin yolunu açabilir.

ACKNOWLEDGEMENTS

This thesis is the product of the last two years of study with emotional ups and downs. It is a work that started with lucky coincidences, continued with both disappointments and encouragement from time to time, and was completed thanks to the people who supported me even though it coincided with a global pandemic time.

First of all, I would like to give my deepest gratitude to my advisor, Assist. Prof. Mehmet Cengiz Onbaşlı. None of this work would have been possible without his support and guidance. He patiently supported me to develop my knowledge in the field of photonics and to produce this work. He guided me in getting the necessary training and accelerating my development day by day. Without his vision, the work in this thesis would not have found such appropriate applications.

I would also like to thank Altuğ Somay and Buse Ebrem Bilgin whom I have been working with for the last year. Thanks to their technical and moral support in difficult times, I was able to solve some of the problems I encountered much more easily. Especially, Altuğ's quick problem-solving skills in software tools have given me valuable time to write this thesis.

This work would not have been possible without the moral support of my dearest family. I am grateful for their eternal support and love. I am thankful to my father for the things he has done for me, and the encouragement he has given to do things on my own. I would also like to express my gratitude to my brother and sister, who have been a role-model and companion for me in coming to these days.

Last but not least, I am grateful to Uğur and Günsun for their endless love and support during my studies and for giving birth to the most beautiful woman in the world. I like to express my sincerest gratitude to my dear wife Müge who supported me not only during my thesis but also in my most difficult times.

TABLE OF CONTENTS

LIST OF TABLES

LIST OF FIGURES

ABBREVIATIONS

BER	Bit Error Rate
BOX	Buried Oxide
CMOS	Complementary Metal-Oxide-Semiconductor
CPU	Central Processing Unit
CW	Continuous Wave
DWDM	Dense Wavelength Division Multiplexing
FDTD	Finite Difference Time Domain
FPGA	Field Programmable Gate Array
FSO	Free-Space Optics
Gbps	Gigabits per second
Ge-on-Si	Germanium on Silicon
GPU	Graphics Processing Unit
IEEE	Institute of Electrical and Electronics Engineers
LED	Light-Emitting Diode
MA	Main Amplifier
MZI	Mach-Zehnder Interferometer
NRZ	Non-return-to-zero
OLED	Organic Light-Emitting Diode
OSNR	Optical Signal-to-Noise Ratio
OTDR	Optical Time Domain Reflectometry
PAM	Pulse Amplitude Modulation
PD	Photodetector
PIC	Photonic Integrated Circuit
Q-Factor	Quality Factor
RC	Resistive-Capacitive
SNR	Signal-to-Noise Ratio
SOI	Silicon on Insulator
TIA	Transimpedance Amplifier
VPIN	Vertical p-i-n junction
WDM	Wavelength Division Multiplexing

Chapter 1:
INTRODUCTION

This chapter introduces some of the initial driving forces behind the advent of silicon photonics and talks about the importance of Ge photodetectors within the field of silicon photonics. Next, it introduces several applications where the performance of Ge photodetectors may vary including sensing (optical time domain reflectometry), and telecom applications. Then, we question the required photodetector characteristics based on each application to maximize the figure-of-merit. Next, the chapter explores the-state-of-the-art germanium photodetector designs and their performance metrics. Finally, outlines the thesis organization in the subsequent chapters is presented.

1.1 Background and Motivation

When we examine today's information technologies, especially in terms of hardware, the source of all is based on perhaps the most effective invention in 1948, the transistor [1, 2]. After the demonstration of the first 2-transistor integrated circuit in 1959, CMOS technology has developed rapidly [3]. Transistor gate lengths have shrunk from micrometer scale to 5 nm nodes in 2020 [4]. As the transistors got smaller and smaller over time, the number of transistors per unit area increased as in Figure 1 [4]. Therefore, the processing power increased continuously enabling abundance of applications that we use in our daily lives. Moreover, realizing the fact that the fabrication quality of the chip is very effective and important in chip performance, many chip manufacturers automated their production lines in order to maximize production volume, yield, and repeatability and to minimize the possibility of human error in fabrication. As a result of this scaling, the production cost per transistor has dropped dramatically. In numerical terms, there has been a decline from $30 per transistor to roughly one of a billionth over the last 50 years [5].

Another way of speeding up the chips that CMOS industry has successfully implemented was to increase the clock frequency. Similar to the integration density, clock speeds have also risen dramatically from a few MHz up to 4 GHz between 1985 and 2000 [6]. As shown in Figure 2, in fact, clock frequency of processors has not been further increased. This stalling is due to the fact that increasing clock speeds also increases the power consumption and cooling the chips become infeasible [6, 7].

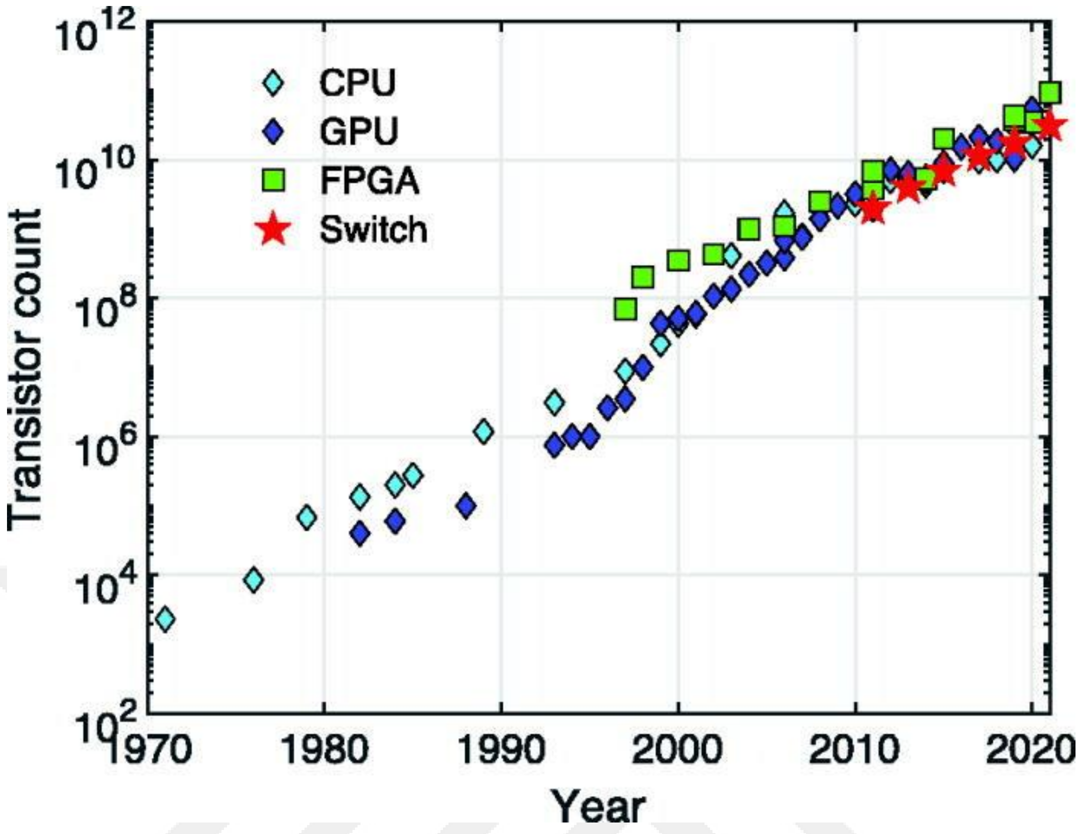

Figure 1: Number of transistors in CPU, GPU, FPGA and Switch [4].

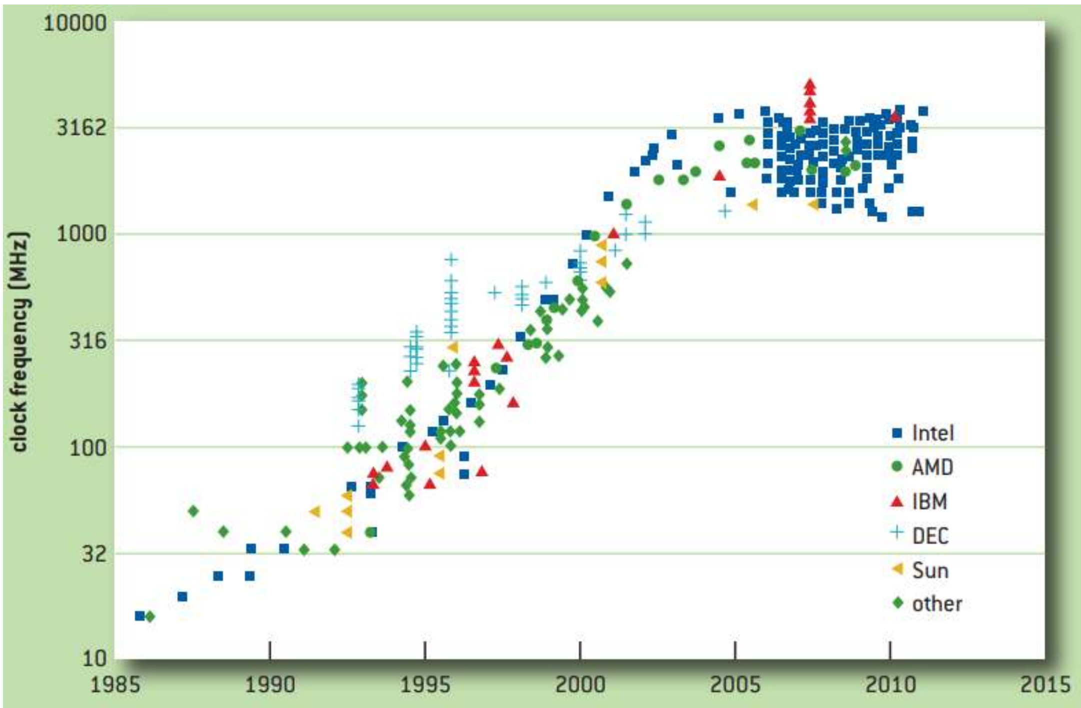

Figure 2: Processor clock frequency over time [6].

As a result, processor architectures became multi-core on silicon chips, so that they can work in parallel in order to perform simultaneous tasks. However, performing simultaneous tasks on a chip has some drawbacks. As the number of cores increases, the number of interconnections required for communication between the cores and peripherals significantly increases [8, 9]. Therefore, the total length of metal interconnects is required to increase proportionally, which results in increasing total capacitance and total resistance of the circuit [10] and is similar to adding a simple RC filter [9, 11]. Consequently, this RC delay determines the maximum speed the circuit can reach, independent of the switching speeds of the logic gates in the microelectronic circuit. As a result, the calculation time is not simply inversely proportional to the number of cores. Propagation delays along interconnects increase computing time and create a bottleneck in terms of the processing speed and throughput.

Minimizing the power consumption and noise levels in communication circuits is important [8]. Many development methods have been applied in CMOS technology to reduce the resistance and capacitance. For example, using Al interconnects instead of Cu or using low-k dielectrics can be shown as examples of some of the studies in this direction [12-14]. While these changes improve the quality of interconnects, doing more than that is now a very costly and power dissipation density can no longer increase for any feasible circuit. For this reason, current technology is approaching its limits in evolving into a new method.

1.2 Silicon Photonics

There is a fundamental difference between electrons and photons in physics. Electrons are good for computing, because two electrons cannot be in the same place, at the same time with the same quantum number due to Pauli's Exclusion Principle. Photons, on the other hand, are not restricted by this constraint since they are bosonic wave-particles which obey Bose-Einstein statistics. Many photons can be in the same place, at the same time and do not undergo electrostatic or exchange interactions with each other as electrons do. As photons have much higher carrier frequencies than electrons and do not lead to Joule dissipation, photons offer significant advantages for low power consumption, high bandwidth, and fiber optical integration. These differences make photons perfect candidates for data transmission. Since much broader band information can be encoded using photons than electrons, using optical interconnects instead of metal interconnects can be reasonable. However, rather than conventional fiber optical cables, similar functions are required to be performed on chip. Silicon photonics is a technology that uses the same fabrication techniques of a CMOS electronics fab to create high-density photonic integrated circuits (PICs) with advanced functionalities. As silicon photonics technology leverages from the existing CMOS technology, it is ideally positioned to produce low-cost and high-yield PICs, while scaling to large commercial volumes [15-18].

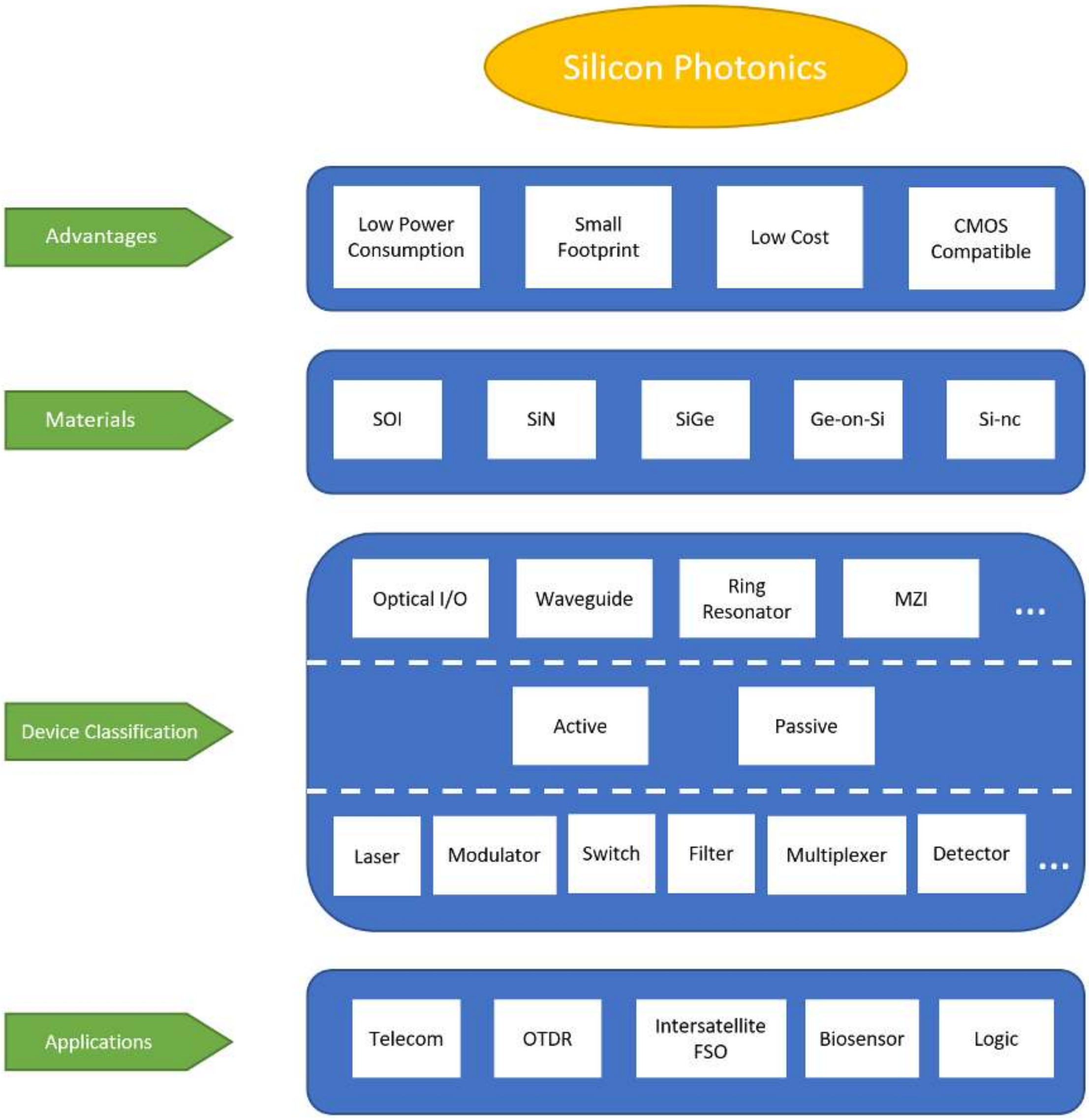

Figure 3: Advantages, materials, device classification and applications of silicon photonics [19].

Figure 3 visualizes the advantages, materials being used, device classifications and applications in the silicon photonics domain at a glance [19]. Silicon-on-insulator (SOI), SiN, GeSi, Ge-on-Si, and silicon nanocrystal (Si-nc) are materials commonly used in silicon photonics, where SOI is the most widely used platform among them. Each of these different materials are best suited for different applications. For example, SiN is the most suitable material for passive devices and some sensors as it has ultra-low loss (at several dB/m [19]) as well as long evanescent mode field tail. SiGe can be used for fabricating low energy electro-absorption modulators, where Ge-on-Si is generally used for high speed photodetectors [17, 19].

The physical dimensions of the devices have reached levels comparable to the wavelength of the light, and today one can fit hundreds of devices into a mm^2 footprint. The main reasons for this are the material properties of silicon. Silicon is an excellent material for developing low-loss passive optical components because of its transparency in the telecommunications wavelength ranges near 1310 and 1550 nm [20]. Due to the high index contrast between silicon core and its highly stable silicon-dioxide cladding, making nm-scale waveguides with very small bending radius in telecommunication bands became feasible. Figure 4 visualizes a typical Si waveguide commonly used in photonic integrated circuits (PICs).

Moreover, as a semiconductor material, silicon can be doped to change its electrical characteristics. Today, integration of components such as resistors, capacitors and diodes into silicon photonic devices and control of electrical variables in a circuit with the help of precise implantation techniques have been demonstrated [21-24]. In doing so, one can design and implement devices that can share information between electrical and optical domains. Some examples of these devices are shown in Figure 5 including modulators, detectors, resonators, couplers, and multiplexers/de-multiplexers.

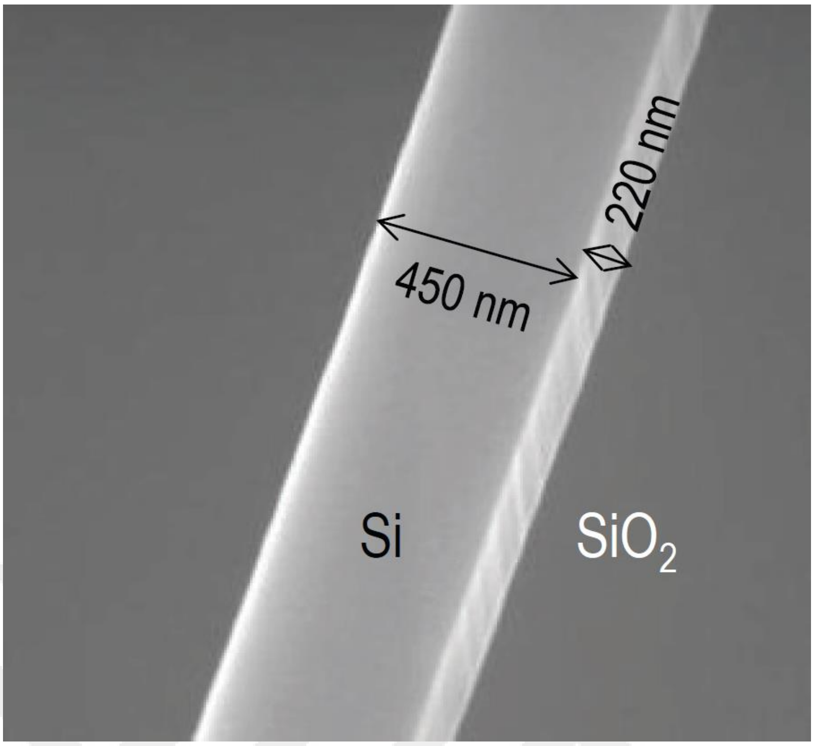

Figure 4: A Si photonics waveguide with Si as core and SiO2 as cladding [25].

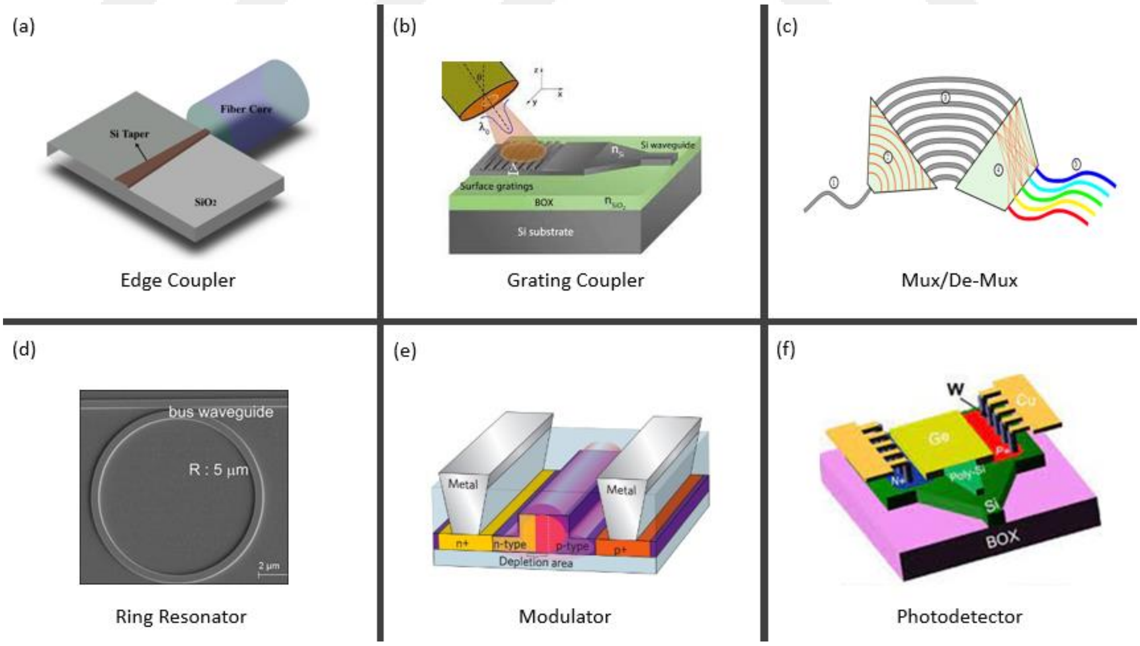

Figure 5: Example silicon photonic devices [25-30].

Grating couplers and edge couplers are used for fiber-to-chip optical coupling (Fig. 5(a) and (b)). Although edge couplers have a broader bandwidth and are polarization insensitive in contrast to grating couplers, they require precise alignment for high coupling efficiency [31]. By using techniques such as wavelength division multiplexing (WDM), transmitted data streams on independent wavelengths can be multiplexed into a single fiber using a multiplexer (Fig. 5(c)). Then the wavelengths are demultiplexed at the demultiplexer and forwarded to the corresponding receivers. In doing so, they allow fiber links to maximize the efficient use of the available bandwidth [32]. A ring resonator is composed of a waveguide that is looped back on itself as shown in Fig. 5(d). The optical resonance occurs when the optical path length of the resonator is equal to an integer multiple of the wavelength $\left(2\pi r \times n_{eff} = m \times \lambda,\ where\ m = 1,2,3\ldots\right)$ [33]. It is preferred for many applications to have a large spacing between resonance peaks that is called free spectral range (FSR). This can be achieved by rings with smaller radius. Modulators are used for electro-optical modulation by utilizing free carrier plasma dispersion effect in the form of a pn junction (Fig. 5(e)). The depletion region width is modulated by an electrical signal and as a result the refractive index of the waveguide is controlled accordingly [34]. They are one of the key devices in high-speed interconnect technology along with the photodetectors. A modulator with high extinction ratio and high bandwidth is preferred. Photodetectors are the devices used for transforming optical signal into electrical signal. Responsivity, bandwidth, and dark current are the fundamental performance metrics of a photodetector. Responsivity is the measure of how well the optical power is transformed into photocurrent. Bandwidth quantifies how fast the detector responds to changes in optical power. Dark current is the current generated by the photodetector when there is no light. It is an unwanted feature because, it contributes to photodetector noise.

Figure 6 shows a cartoon of typical devices can be fabricated on a silicon photonics platform. The first silicon photonics circuit integrated with a microprocessor was reported in 2015 which indicates a trend of the development in the semiconductor industry [35].

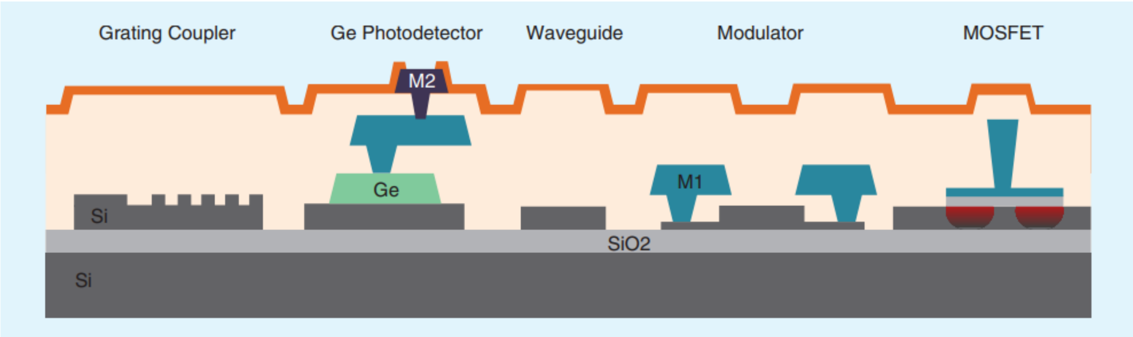

Figure 6: Grating coupler, Ge Photodetector, waveguide, modulator and MOSFET on a SOI wafer [36].

Despite the fact that silicon photonics dates back to the late 1980s, it was not until 2007 that Luxtera's transceivers for datacenter communication hit the market and became a mass-produced silicon photonics product as shown in Figure 7 [17]. Especially with the rapid breakthrough in the last fifteen years, silicon photonics has become one of the most suitable platforms for integrated optics thanks to its low power consumption, low cost, small footprint and most importantly CMOS compatibility [37]. Creating very low-cost photonic devices using the mature IC industry is the fundamental source of motivation for the researchers. From datacom and telecom to sensors like LIDARs, gyroscopes, biosensors, and spectrometers, silicon photonics offers a wide range of applications [4].

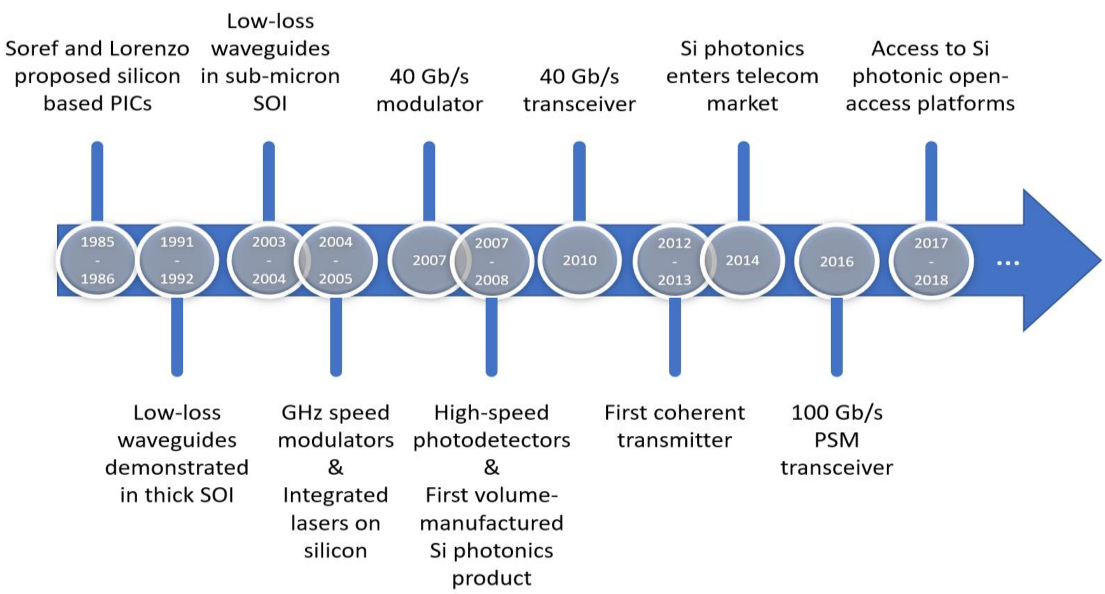

Figure 7: Major milestones in silicon photonics for telecommunication applications [17].

Silicon PICs are being manufactured commercially today in 200 and 300mm CMOS foundries with a nm-level accuracy and reproducibility, unprecedented from a photonics perspective. If we assume a large volume of demand similar to a serial production, and $5 \times 5\ mm^2$ area for a PIC, with the current potential in silicon photonic fabs cost per chip can be as low as 2.5 € as shown in Figure 8.

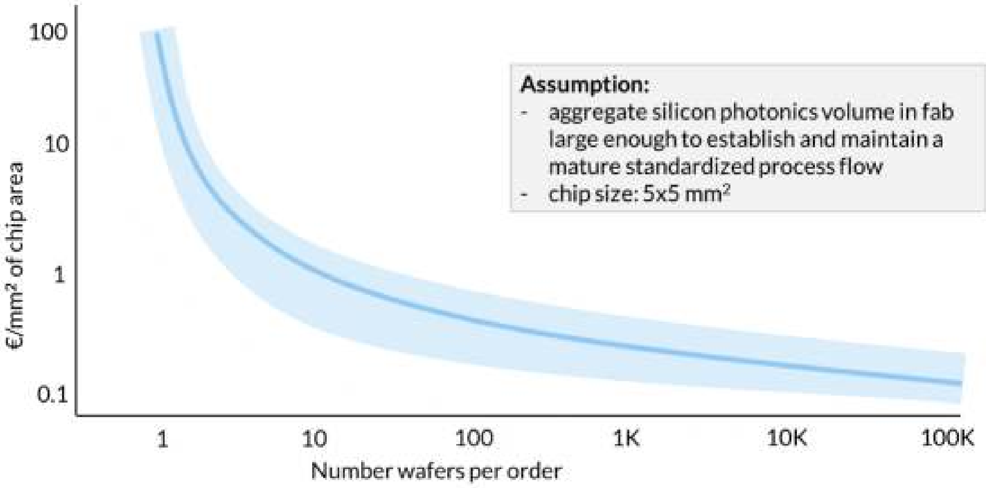

Figure 8: Price per unit mm^2 for a silicon photonics chip manufactured in a CMOS fab [38].

1.3 Optical Transceivers

Fiber optical data links operate simply as shown in Figure 9(a), where at one end of the fiber is the transmitter circuit and the other end is the receiver circuit. Most systems work in full duplex mode by transmitting data in one direction on one fiber and in the opposite direction on the other. The transmitter side takes an electrical input and generates an optical output signal by a laser diode or LED. The light from the transceiver is transferred back and forth to the fiber via fiber optical couplers. Light from the end of the fiber is converted into an electrical signal through a photodetector and then coupled to a receiver where it is properly conditioned for use by the receiving equipment. A cartoon of a commercial optical transceiver is illustrated in Figure 9(b).

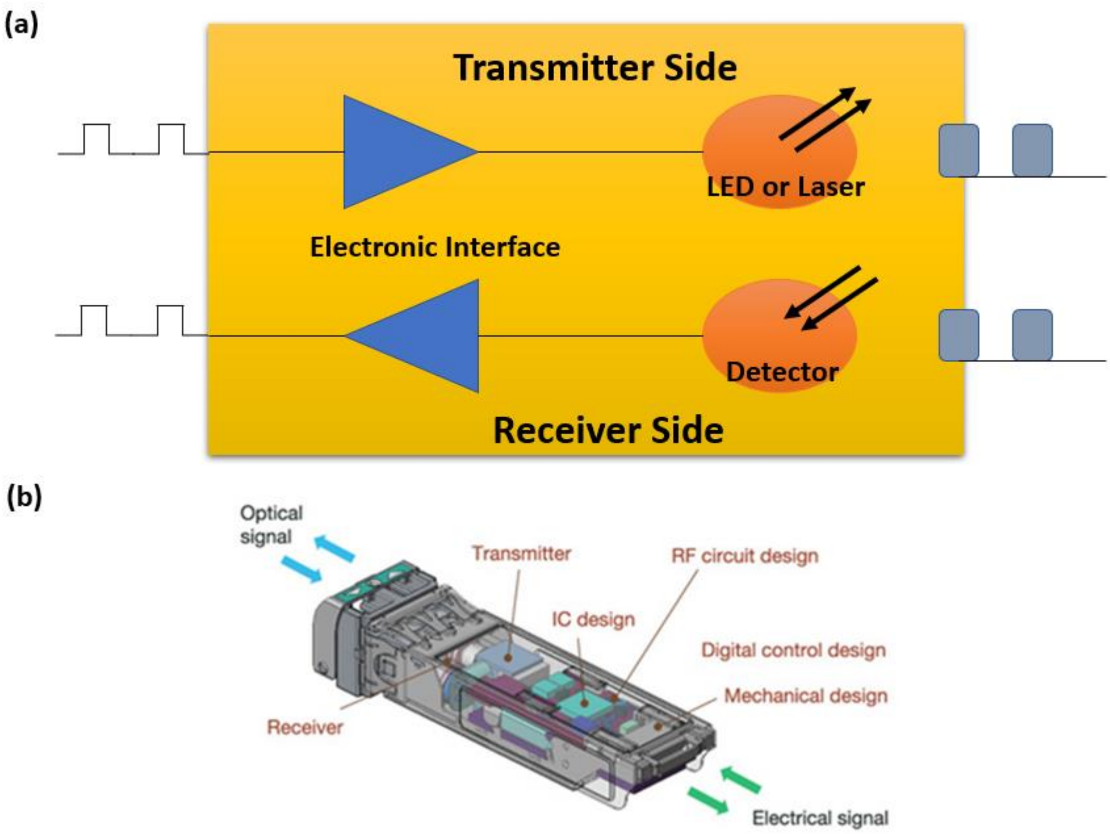

Figure 9: Optical transceiver (a) functional block diagram, (b) commercial example [25].

As previously mentioned, there are a number of applications in which silicon photonics can be a solution. The most common application is data communication which requires high bandwidth digital communications [39]. Typical high bandwidth fiber optical transmission systems nowadays employ a variety of ways to multiplex a large number of electrical data streams at 10, 28, and 40 Gbps onto single fibers [36]. Wavelength division multiplexing is a telecommunications technology in which each color of light is modulated independently and then merged into a single fiber [40]. Other approaches use coherence to encode information in phase, amplitude, and polarization independently, allowing for the transmission of several bits per symbol [41]. As a result, it becomes possible to build systems transmitting terabits of data in a single fiber without using any electronics faster than 40 Gbps [36].

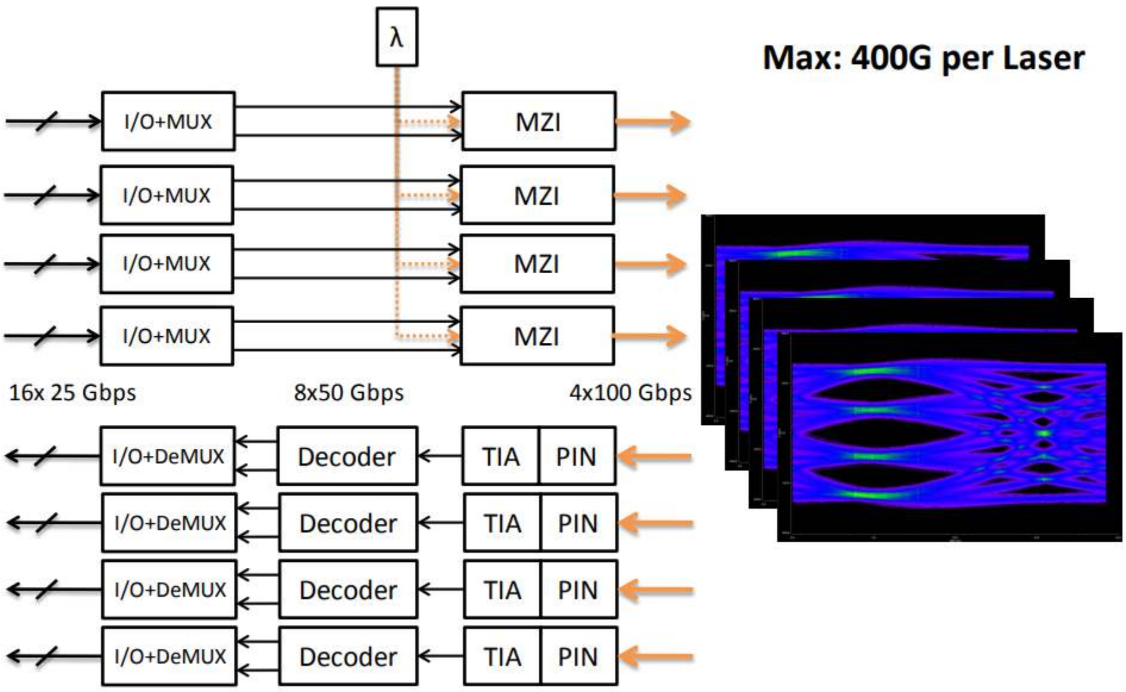

Figure 10: 400G-PSM4 architecture composed of four parallel fibers and PAM4 modulation [42].

Figure 10 shows the architecture of the 400G-PSM4 silicon photonics optical transceiver designed by Luxtera composing of 4 parallel lines with a single line rate of 100 Gbps [42]. In order to achieve such a high baud-rate in a single line, high speed Ge photodetectors are required in the receiver side.

On the other hand, beyond data communications new applications are being explored in both the commercial and academic worlds for silicon photonics technology [39]. For example, for a sensing application such as optical time-domain reflectometer (OTDR), high speed performance of the photodetector may not be the key parameter, but the responsivity and dark current are. A simple OTDR circuit is shown in Figure 11, where the modulated laser signal is sent via transmitter and backscattered through the kilometers long fiber and detected by the photodetector. As the losses are increased through the fiber due to connectors, splices and fiber loss itself, the reflected signal would be quite small and in practice depending on the range, the received optical power may be as much as 50 dB lower than the optical input signal [43].

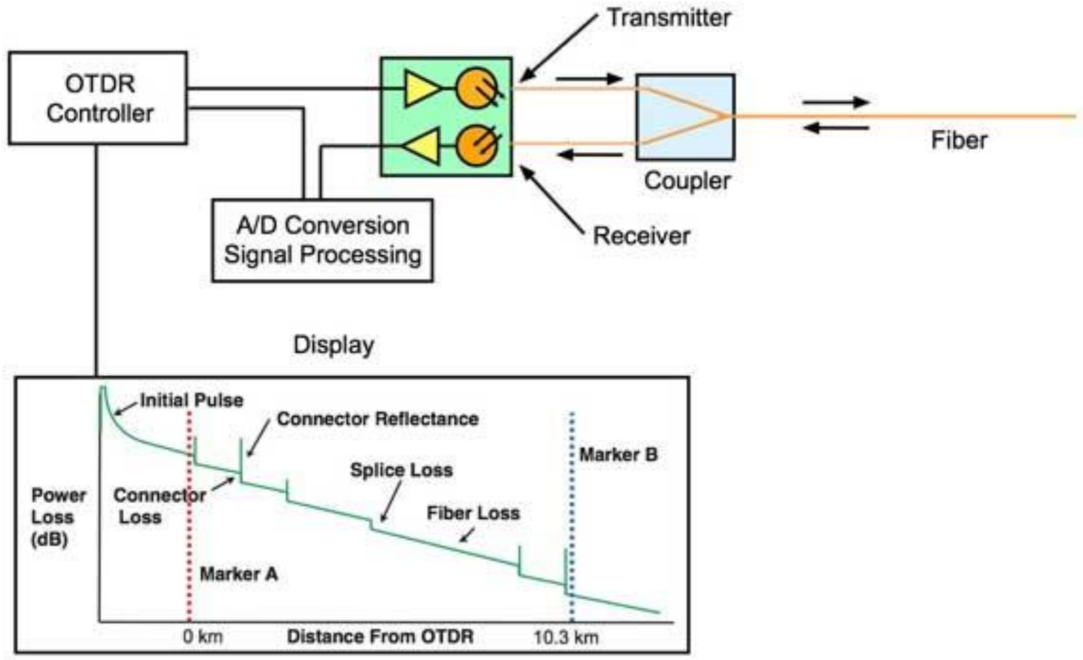

Figure 11: OTDR circuit and output signal [44].

In the optical domain, photodetectors determine the electro-optical conversion efficiency of the whole system and SNR characteristics of the systems are directly affected by the performance of the photodetectors. Moreover, in order to utilize the high bandwidth features of photonics, photodetectors need to be designed in proper geometry with suitable materials. Because of its significant optical absorption in the fiber optical communication window (C-band and O-band), germanium is well suited for highly sensitive near-infrared optical detectors [25]. Furthermore, most leading integrated circuit manufacturers already use germanium in the chip making process to improve transistor performance, thus it is relatively easy to include germanium to enhance optical performance as well [45].

Therefore, depending on the application, different requirements force us to design photodetectors optimized over different figures of merit. While in a telecom and datacom application the bandwidth of the photodetector is the most crucial parameter, for an OTDR application sensitivity can be much more important and using photodetectors with high bandwidth may not necessarily be an advantage. Designing different photodetectors with different geometries and optimal operation characteristics for telecom and sensing applications constitutes the motivation behind this thesis.

1.4 Literature Review: Ge-on-Si Photodetectors

Photodetectors are one of the most important components used in the receiver side of an optical communication link [46, 47]. They convert optical signal into photocurrent, and therefore directly affect the signal-to-noise ratio (SNR) of the communication signal with their noise floor, responsivity and device architectures [48]. Semiconductor p-n or p-i-n junction photodiodes are commonly used because their electronic bandgaps match the photon energies of interest (i.e., for 1310 and 1550 nm) and yield higher SNR. Insulators or metals are not used alone for photodetection because their electronic bandgaps are too wide and non-existent, respectively. Hence, these two types of materials do not absorb the incident photons unless they are used in conjunction with other semiconductor layers.

The photoelectric effect in semiconductors is the basis of working principle of photodetectors as depicted in Figure 12. They convert the optical energy of photons absorbed by the active region of the semiconductor junction and produce free charge carriers. An applied reverse bias voltage sweeps charge carriers out of active region which creates a measurable change in current [48]. An ideal photodetector would have high responsivity, low dark current and high bandwidth.

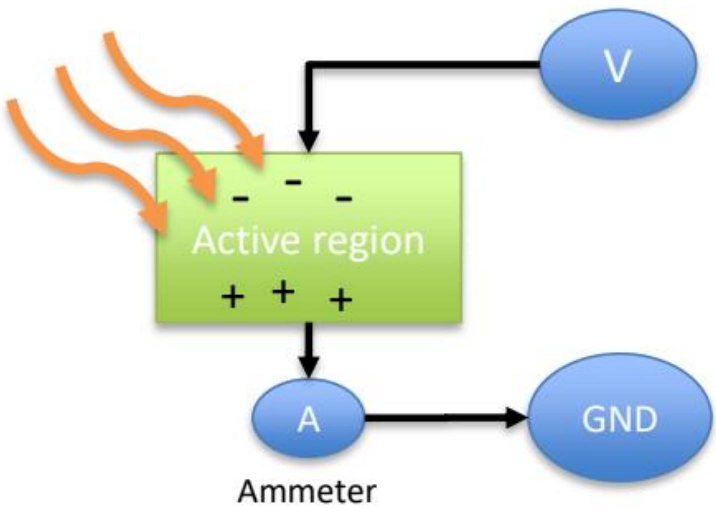

Figure 12: Working principle of photodetectors. The photoelectric effect.

As previously mentioned, silicon does not absorb photons with wavelengths longer than 1100 nm and at telecom wavelengths (i.e., 1310 and 1550 nm). Its high refractive index and no loss at telecom wavelengths make silicon the most common choice for waveguide core material. Due to silicon's bandgap, telecom wavelengths cannot be absorbed. To absorb light, different techniques have been developed in silicon photonics including epitaxial germanium growth, III-V bonding, plasmonic absorption, sub-bandgap detection, and surface state absorption [49-59]. Epitaxially grown germanium-on-silicon photodetectors have emerged as the most practical detectors [39, 60-62]. Due to their characteristics such as having a small footprint, being highly responsive, fast, and low power, epitaxial germanium photodetectors are the most popular approach for silicon photonics.

Originally, high-performance Ge-on-Si photodetectors were normal-incidence detectors with light entering the detectors via fiber coupling or free space [63-71]. Later on, waveguide-integrated Ge-on-Si detectors have advanced rapidly in the recent decade to enable compact circuits on a silicon chip [62, 72-90]. Figure 13 shows the cross sections of normal-incidence and waveguide-integrated photodetectors.

Geometric dimensions of normal-incidence detectors are crucial. The larger detector area can increase capacitance and dark current, therefore limiting the bandwidth and sensitivity [63]. Also as shown in Figure 13(a), the thickness between anode and cathode contacts constitutes the absorbing region and its thickness determines the total absorbed power, and therefore affects the responsivity. However, it also reduces the carrier drift velocity at a given reverse bias and limits the bandwidth. In contrast to normal-incidence detectors, waveguide-integrated detectors have a longer absorption length in the direction of the light. The collection path of generated photo-carriers and the light propagation path are orthogonal with waveguide integration, which is a significant benefit over normal-incidence devices [91]. Therefore, the trade-off between responsivity and bandwidth for normal-incidence detectors diminishes [19, 72]. As a result, waveguide-integrated photodetectors may operate at high-speed while maintaining high responsivity. Likewise, since waveguide-integrated photodetectors have a substantially smaller device footprint than normal-incidence detectors, the dark current levels can be relatively kept low enough for application requirements [19, 72].

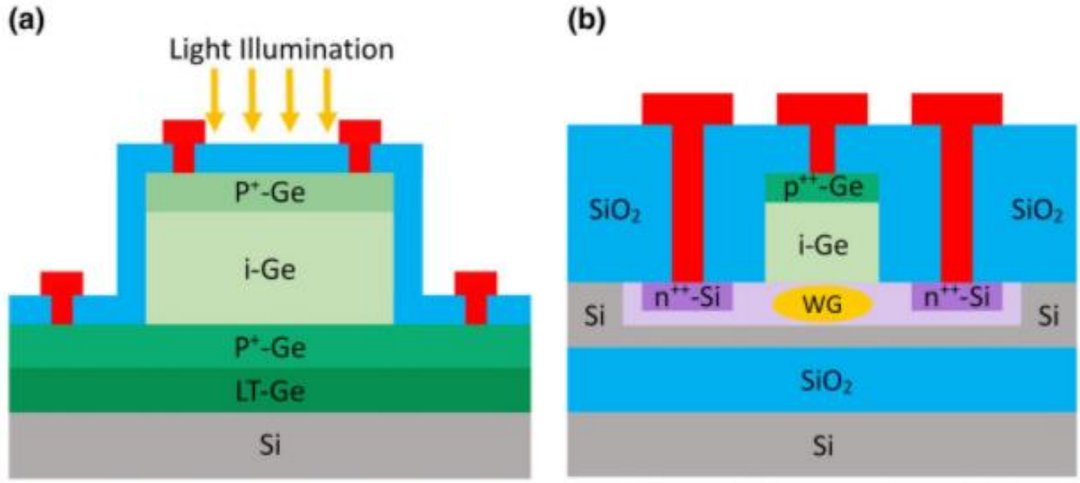

Figure 13: Cross section of (a) normal incidence vs (b) waveguide integrated photodetector [92].

The performance of silicon photonic detectors has significantly improved since the first discovery of waveguide-integrated photodetectors. Table 1 highlights many demonstrations of waveguide-based Ge-on-Si detectors that have been published. Based on the relative position of the silicon waveguide and Ge detector region, three coupling strategies between silicon waveguide and Ge detector are available in the literature [63]:

1. Silicon waveguide is placed on top of the Ge detector (top-coupled),
2. Silicon waveguide is placed beneath the Ge detector (bottom-coupled),
3. Butt-coupling,

In the first two coupling method, the light is evanescently coupled from silicon waveguide into Ge detector. However, in the bottom-coupled design, silicon waveguide is required rather than SiN or SiON, because the germanium requires a crystalline template for epitaxial growth [63]. Figure 14 demonstrates bottom-coupling and butt-coupling configurations from a vertical cross section perspective. Despite the high coupling efficiency of butt-coupling, the second configuration is the most common due to its ability to integrate in a CMOS process [63]. This design choice can also be seen in Table 1, as the majority of the recently demonstrated Ge detectors are in the bottom-coupled configuration.

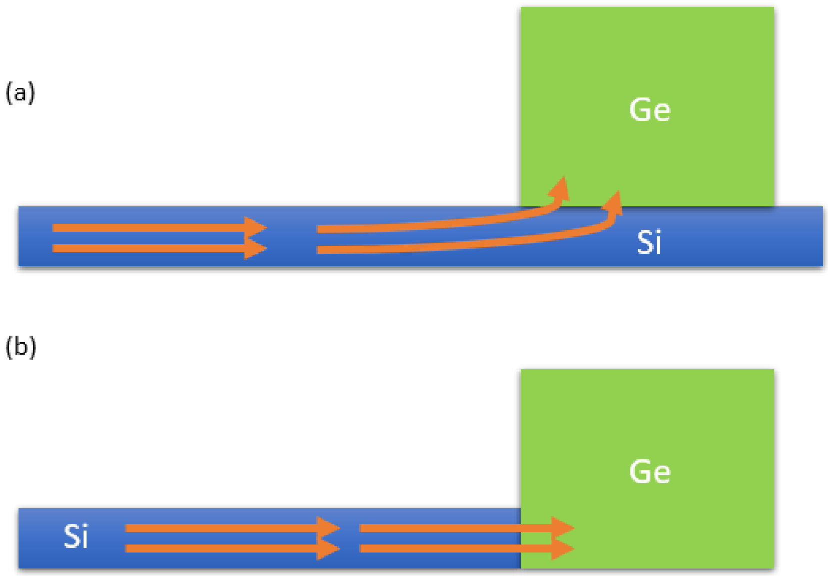

Figure 14: (a) Bottom-coupled, (b) butt-coupled waveguide integration from vertical cross section.

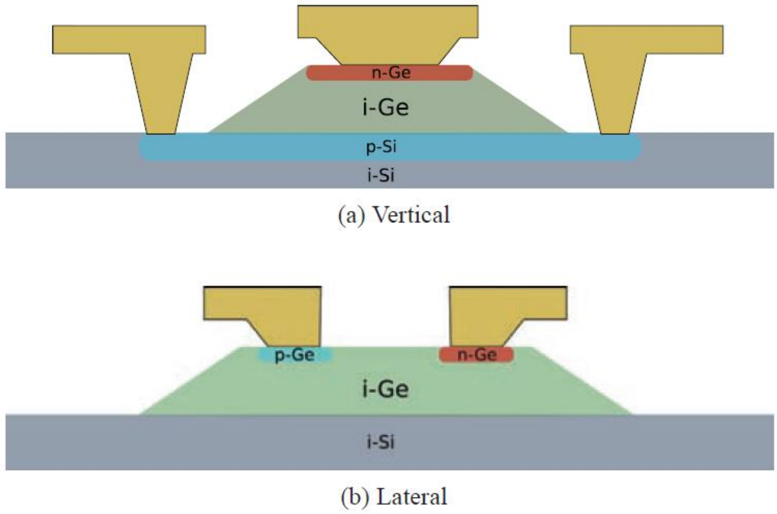

Figure 15: Vertical cross section of two types of PIN junction orientation. (a) Vertical, (b) Lateral [39].

Furthermore, as shown in

Figure 15 there are vertical and lateral p-i-n Ge detectors available in the literature depending on the orientation of the doping regions. In the vertical junction orientation, the photocurrent must pass from the silicon-germanium interface while travelling from cathode to anode. Therefore, due to interfacial defects, in this orientation higher dark current and lower responsivity is expected. On the other hand, the lateral junction does not suffer from interfacial defects, but in order to sweep the carriers from the active region quickly, this orientation requires higher reverse voltage levels [39].

Table 1: Comparison of waveguide-integrated Ge-on-Si photodetectors.

Year	Responsivity	Bandwidth	Dark Current	Coupling	Orientation	Ref.
2006	1 A/W	4.5 GHz @3V	0.2nA @1V	Butt	Vertical	[74, 84]
2006	0.22 A/W	1.5 GHz @4V	-	Bottom	Vertical	[84]
2007	1.08 A/W	7.2 GHz @1V	1μA @1V	Top	Vertical	[72]
2007	0.89 A/W	31.3 GHz @2V	169nA @2V	Bottom	Vertical	[89]
2008	0.85 A/W	26 GHz @1V	3μA @2V	Bottom	Lateral	[85]
2009	1.1 A/W	32 GHz @1V	1.3μA @1V	Butt	Lateral	[80]
2009	1 A/W	42 GHz @1V	18nA @1V	Butt	Vertical	[87]
2011	0.95 A/W	36 GHz @1V	46nA @1V	Bottom	Vertical	[82]
2012	0.8 A/W	120 GHz @2V	4μA @1V	Butt	Lateral	[88]
2013	0.75 A/W	60 GHz @2V	3μA @1V	Bottom	Vertical	[62]
2015	0.85 A/W	60 GHz @4V	61nA @0.5V	Bottom	Vertical	[76]
2015	1 A/W	>70 GHz @1V	0.1μA @1V	Bottom	Lateral	[83]
2016	0.74 A/W	67 GHz @1V	4nA @1V	Bottom	Lateral	[77]
2016	1.09 A/W	42.5 GHz @2V	3.5μA @1V	Bottom	Vertical	[79]
2017	0.72 A/W	31.7 GHz	7nA	Bottom	Vertical	[78]
2018	0.75 A/W	17 GHz @4V	150nA	Bottom	Vertical	[90]
2019	1.2 A/W	7 GHz	100nA	Butt	Lateral	[75]
2020	0.82 A/W	29GHz @4V	1.6nA @1V	Bottom	Vertical	[81]

A range of device configurations have been developed for germanium waveguide p-i-n photodetectors integrated on Si photonics platform. The state-of-the-art germanium-on-silicon p-i-n photodetectors reported in the previous 15 years are listed in Table 1 with their performance metrics including responsivity, bandwidth and dark current with respect to reverse bias voltage. It is important to minimize the reverse-bias voltage of Ge photodetectors in order to both reduce the dark current and to be applicable to CMOS integration. Different design geometries yield different responsivity, bandwidth, and dark current values. Theoretically, a photodetector with a responsivity of 1.25 A/W at 1550 nm is achievable for unity quantum efficiency. Also, by decreasing the detector area, high-speed detectors offering bandwidths beyond 100 GHz are achievable. However, due to the design tradeoff between these figures of merits, it is difficult to maximize both of them at the same time. Therefore, in order to compare different designs responsivity-bandwidth product is a commonly used metric [91]. The highest responsivity-bandwidth product for a waveguide integrated germanium detector is reported by Vivien et al. with a responsivity of 0.8 AW^{-1} and 120 GHz bandwidth at 2V reverse-bias [88].

Liu et al. developed the first vertical oriented p-i-n photodetector with a dark current lower than 1 μA [84]. This butt-coupled device adopts a 0.6μm-thick, 0.6μm-wide and 50μm-long Ge layer showing a 1 AW^{-1} responsivity with a bandwidth of 4.5 GHz at -3V bias. Then, Yin et al. demonstrated the first germanium photodetector with an optical bandwidth exceeding 30 GHz [89]. This vertical-oriented and bottom-coupled device has an active region with a thickness of 0.8 μm, a width of 7.4 μm and length of 50 μm. It showed an optical bandwidth of 31.3 GHz at -2V bias with a responsivity of 0.89 A/W and 169nA dark current. In 2009, Vivien et al. reported a photodetector exceeding an optical bandwidth of 40 GHz [87]. This vertical p-i-n detector has an active region with 15μm length, 3μm width and 0.4μm thickness. The optical bandwidth is 42 GHz with a responsivity of 1 AW^{-1} at -4V bias. In 2012 Vivien et al. and in 2015 Lischke et al. showed that using lateral orientation in p-i-n photodiode performance of the detector can approach the theoretical limits [83, 88].

However, despite the success of prototype designs, the fabrication of the lateral p-i-n photodiodes is more complex than their vertical counterparts and to mass produce chips with lateral detectors may be very inefficient and lead to low yield. More photo mask levels are required for lateral photodetectors, and ion implantation stages cannot be eliminated [93]. A major advantage in vertical photodetector fabrication process is that the fully relaxed high-quality germanium is away from the silicon-germanium interface. This always guarantees a higher level of performance and opens a wider process window for manufacturability [93].

As photodetector designs mature, the research focus in designing vertical photodetectors is shifting to studying metal contacts, inductive-gain peaking, or wire bonding to optimize device bandwidth rather than optimizing geometric device lengths [62, 76, 79]. However, this is true only for photodetectors designed for telecom and datacom applications. There is a great research space for designing other application-specific photodetectors such as sensing.

In this thesis, the design limits for waveguide integrated vertical p-i-n germanium photodetectors are examined in terms of bandwidth, responsivity, and dark current. It is shown that ultra-high bandwidth photodetectors for telecom applications can reach up to 84 GHz bandwidth with 0.97 AW^{-1} responsivity and ultra-high responsivity photodetectors for sensing (OTDR) applications can reach 1.17 AW^{-1} at 0V bias.

1.5 Organization of This Thesis

This thesis is organized as in the following chapters:

- In Chapter 2, I present the working principles of photodetector devices. I started by briefly analyzing the absorption process in p-i-n photodiodes. Then, the effects of changing the geometry of the active region of the detector is analyzed. Next, the performance metrics of p-i-n photodetectors and the noise characteristics in optical receivers are examined. Finally, I calculated the received power characteristics of some applications.

- In Chapter 3, I design and analyze a vertical p-i-n germanium-on-silicon waveguide integrated photodetector with 10μm length, 4μm width and 1μm thickness as a baseline device. In doing so, I used Lumerical software tools to design and simulate the photodetector and analyze the performance metrics. Then, the baseline device is simulated along with the other opto-electronic components to analyze its performance in a typical receiver circuit. In the final part, several simulations performed by changing the device geometry in three dimensions and the results are discussed in terms of optimal performance metrics. As a result, design guidelines for waveguide-integrated photodetectors are presented as a summary.

- In Chapter 4, based on the results obtained from the previous chapter, new photodetector design geometries are examined in order to satisfy the requirements of telecom and OTDR (sensing) applications. The obtained performance metrics for telecom detector are 84 GHz bandwidth with 0.97 AW^{-1} responsivity and 8.67 nA dark current at -2V bias. The performance metrics of OTDR detector are 1.17 AW^{-1} responsivity and 25.73 GHz bandwidth at 0V bias.

- In Chapter 5, the thesis is finalized with a conclusions and future work part.

Chapter 2:
MATERIALS AND METHODS

2.1 *Photodetector Basics*

A photodetector is an optoelectronic device that converts photon energy into an electrical signal. The operation of a photodetector is based on photon absorption in a semiconductor by electrons and their excitation from valence to conduction band. In a semiconductor photodetector, optical signal detection can be divided into three steps [48]:

- Absorption of light and electron-hole (carrier) generation,
- Carrier transportation through the absorbing region under an electric field or built-in bias,
- Photocurrent generation.

In this section, the fundamental definitions on the absorption characteristics, detector geometry, and the figures of merit metrics and methodology for investigating p-i-n photodetectors are presented.

A great portion of optoelectronic devices are created by using semiconductor materials that possess a p-n or a p-i-n junction. The electrical characteristics of a p-n junction at thermal equilibrium can be shown as in Figure 16. When n-doped and p-doped layers form a junction, a diffusion current is generated due to different charge concentration levels and chemical potential gradient. The electrons diffuse from n-doped region to p-doped region whereas the holes diffuse p-doped region to n-doped region, conversely. The total diffusion current can be expressed as in equation (1.1) where D_n and D_p are the electron and hole diffusion coefficients and ∇n and ∇p are the gradients of electron and hole concentrations, respectively [94].

$$J_{diff} = J_{diff,n} + J_{diff,p} = qD_n \nabla \mathrm{n} + qD_p \nabla \mathrm{p} \tag{1.1}$$

The area closed to junction becomes depleted due to diffused electrons and holes. Therefore, the atoms in this region lose their electrical neutrality and become charged ions. This region that consists of positively charged ions in the n-doped region and negatively charged ions in the p-doped region is called the depletion region, W_D, as shown in Figure 16(a). The spatial distribution of the depletion region satisfies the neutrality condition as in equation (1.2) where W_{D_p} and W_{D_n} are the diffusion reach in the p-type and n-type materials and N_A and N_D are the acceptor and donor impurity concentrations, respectively [94].

$$N_A W_{D_p} = N_D W_{D_n} \tag{1.2}$$

Therefore, the electric potential is created in the depletion region due to ionized atoms that is called ψ_{bi}, the built-in potential. This built-in potential opposes the further diffusion of electrons and holes. It also produces a drift current due to electric field caused by ψ_{bi}. Typical ψ_{bi} values are 0.3V for germanium and 0.7V for silicon diodes [95].

The total drift current is the sum of drifted electrons and holes as in equation (1.3) where μ_n and μ_p are the electron and hole mobilities, n and p are the electron and hole concentrations and $\vec{E}$ is the drift electric field, respectively [94].

$$J_{drift} = J_{drift,n} + J_{drift,p} = q\mu_n n\vec{E} + q\mu_p p\vec{E} \tag{1.3}$$

The total current that is the sum of drift and diffusion currents are given in compact form by the equation (1.4) where i represents the type of carrier (n or p) and $\frac{dE_F}{dx}$ is the gradient of the intrinsic Fermi level across the junction.

$$J_i = q\mu_i i\vec{E} + qD_i \nabla \mathrm{i} = \mu_i i \frac{dE_F}{dx} \tag{1.4}$$

Applying external bias voltage to the p-n junction unbalances the drift-diffusion equilibrium via the relation $\psi_{bi} - V$ resulting with a non-zero total current, J_i. A forward bias increases diffusion current and decreases the width of depletion region, whereas a reverse bias increases the depletion region width and decreases the diffusion current until a breakdown occurs in the diode [96]. The width of the depletion layer in a p-n junction can be expressed as in equation (1.5) [94].

$$W_D = \sqrt{\frac{2\varepsilon_r\varepsilon_0(N_A + N_D)}{qN_AN_D}(\psi_{bi} - V)} \tag{1.5}$$

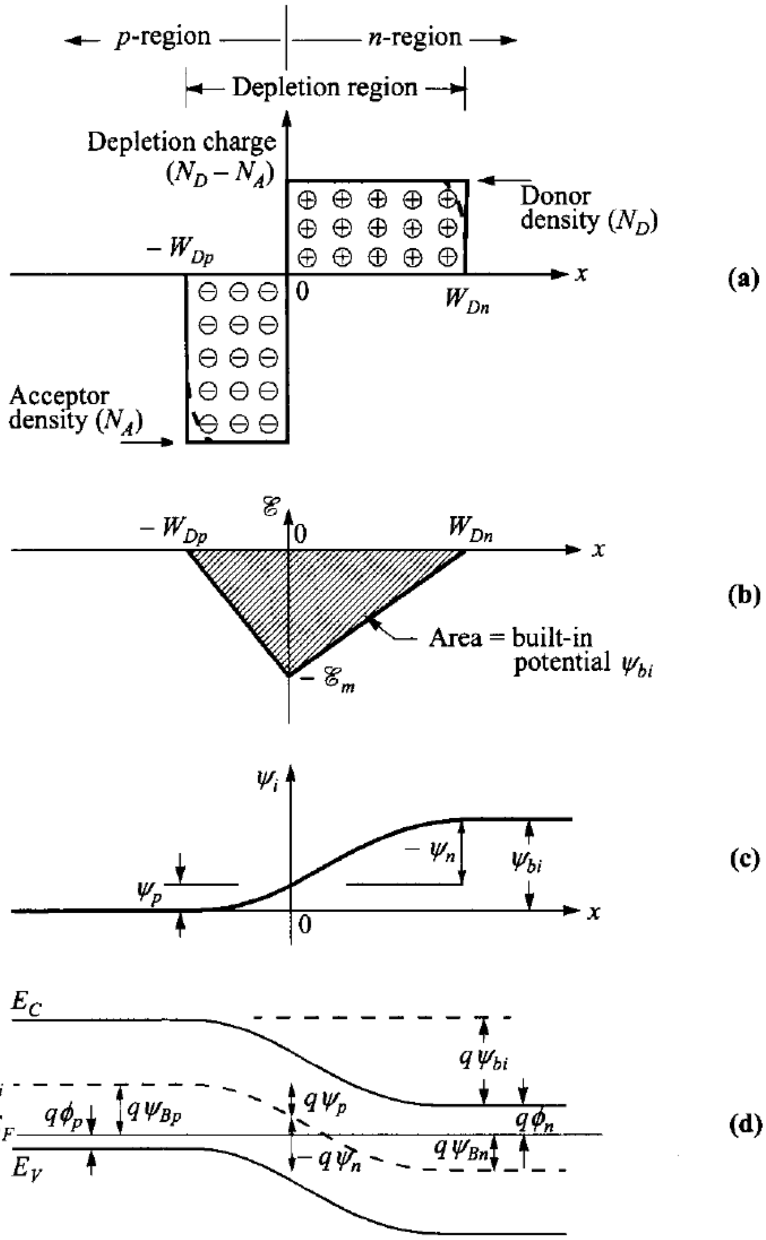

Figure 16: A p-n junction in thermal equilibrium [94]. (a) Spatial charge distribution. Dashed lines on the corners indicate corrections to depletion approximation. (b) Electric field distribution. (c) Potential distribution where ψ_{bi} is the built-in potential. (d) Energy band diagram. At thermal equilibrium, Fermi energy level, E_F is same for each side of the junction. However, Fermi levels are split into two distinct quasi-Fermi levels by applying an external voltage bias.

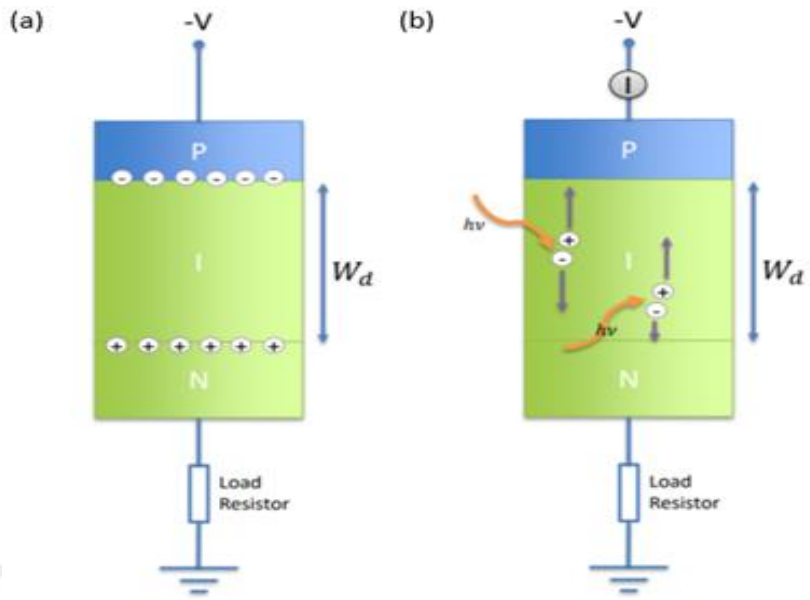

Figure 17: p-i-n junction under reverse bias consisting of three layers: p-doped, intrinsically-doped and n-doped layers. [97] (a) It is reverse biased and loaded with a load resistor. The intrinsic region increases the depletion region width. (b) Most of the incident photons are absorbed within the depletion region. In photodetection, carrier diffusion and drift contribute to photoconductance.

Similar to p-n junction, p-i-n junction is a diode with an undoped intrinsic region that is sandwiched between p-type and n-type regions as shown in Figure 17. Besides photodetectors, they are also used for solar cells, attenuators, RF switches, and many other purposes. It was invented by Jun-ichi Nishizawa in 1950 [98]. Among the three modes of operation of photodiodes, namely photovoltaic (open-circuit), short-circuit and photoconductive (reverse-biased), p-i-n photodetectors are operated in photoconductive mode as shown in Figure 17 [48]. The excess charge carriers in the p and n doped regions can drift through the intrinsic region with the help of reverse bias voltage and create a large depletion region that is very close to the width of intrinsic region [99]. The width of the depletion region in p-i-n photodiodes can be expressed as in equation (1.6) where W_{int} is the width of the intrinsic region [100].

$$W_D = \sqrt{{W_{int}}^2 + \frac{2\varepsilon_r\varepsilon_0(N_A + N_D)}{qN_AN_D}(\psi_{bi} - V)} - W_{int} \qquad (1.6)$$

The built-in voltage originating from the carrier concentration differences and the band gap of the material used in the intrinsic region. The relation can be expressed as in equation (1.7) where N_V and N_C are the effective density of states in valence and conduction band, respectively [94]. Due to the fact that E_g and $k_B T$ parameters in the equation determined by material characteristics and environmental conditions, in order to tune the threshold voltage, the doping concentrations are used as tuning parameters.

$$q\psi_{bi} = E_g - k_B T \ln \frac{N_V N_C}{N_A N_D} \tag{1.7}$$

The excess charge carriers build up on the edge of depletion region and act like a parallel plate capacitor with a near uniform electric field inside it as shown in Figure 17(a) [39, 48]. The absorbed photons in the intrinsic region generate electron hole pairs and these photogenerated carriers are swept out of the depletion region due to electric field and results in generating a photocurrent.

The reason of photodiode operating in the reverse bias can also be understood by looking in the I-V graph of the photodiode. When it is reverse biased, the photodiode operates in the third quadrant and the photocurrent varies almost linearly with the light intensity as shown in Figure 18 [101]. By operating in this quadrant, the signal-to-noise ratio of the photodiode is also maximized.

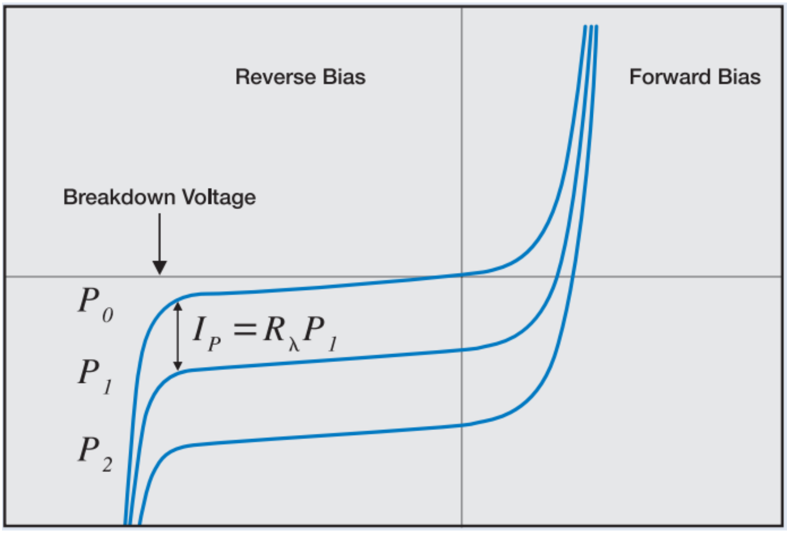

Figure 18: I-V graph of a photodiode under illumination. P_0, P_1 and P_2 represent different light levels [101].

2.1.1 Absorption Characteristics

Semiconductors absorb photons by exciting electrons from valence to conduction bands [102]. A semiconductor crystal has long range order and hence, the energy levels are determined due to the bonding structure within the lattice. The energy levels belong to the system as a whole because of the proximity of the atoms in the crystal lattice [48]. Hence, a group of dense energy levels forms into energy bands. These bands are either entirely filled by electrons or completely unoccupied in the absence of external stimulation at $T = 0\ °K$ [48]. At finite temperatures, the lower energy levels of the conduction band are partially occupied. The conduction band is the lowest-lying vacant energy band, whereas the valence band is the highest-lying completely occupied energy band. A range of energies exist between valence and conduction bands as prohibited band with energy range E_g. This gap separates these two bands. As shown in Figure 19, the valence and conduction bands are separated by the bandgap energy E_g which is 1.12 eV and 0.66eV for silicon and germanium, respectively [103, 104].

A photon with an energy greater than the bandgap energy of a material can be absorbed, thus, it creates an electron-hole pair [105]. The spectral region where the material changes from relatively transparent ($h\nu < E_g$) to strongly absorbing ($h\nu > E_g$) is known as the absorption edge [48]. The minimum frequency ν required for absorption is,

$$\nu_g = \frac{E_g}{h} \tag{2.2}$$

Similarly, corresponding maximum wavelength is,

$$\lambda_g = \frac{c_0}{\nu_g} = \frac{hc_0}{E_g} \tag{2.2}$$

If the bandgap energy is given in eV (rather than J), the bandgap wavelength (cutoff wavelength) turns out to be,

$$\lambda_g \approx \frac{1.24}{E_g} \tag{2.3}$$

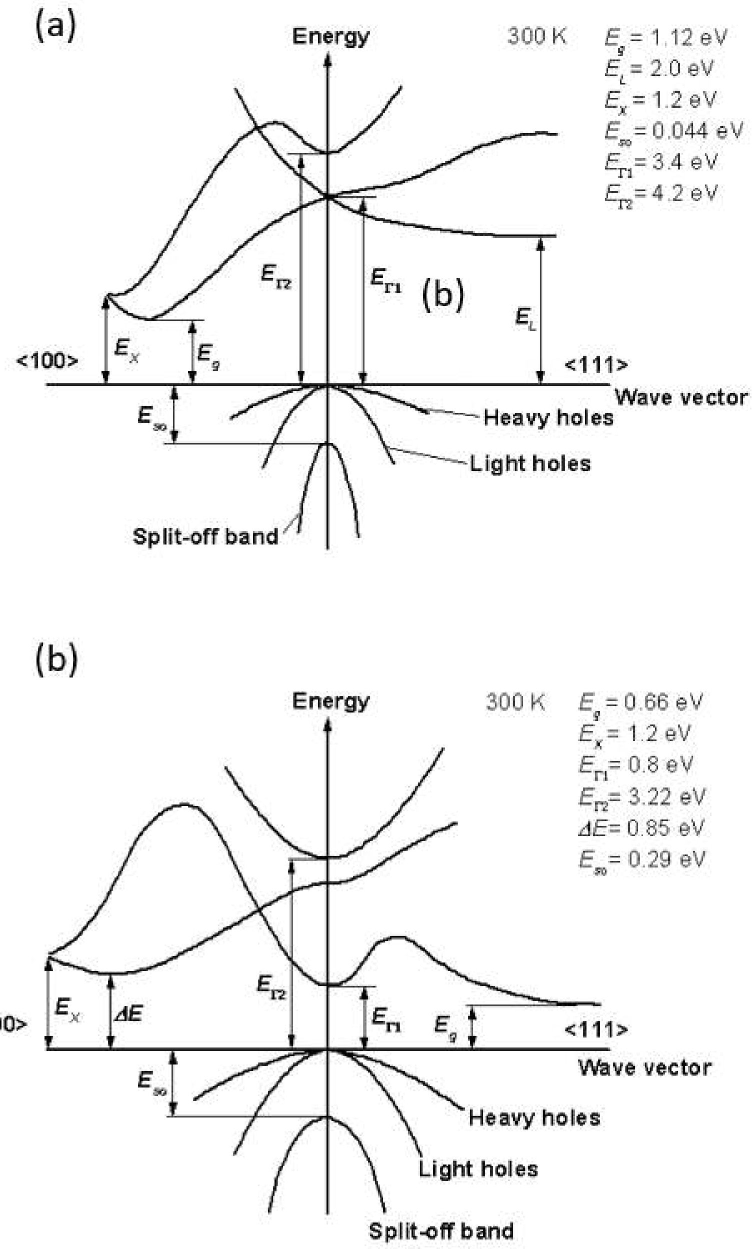

Figure 19: Energy band diagrams (a) silicon, (b) germanium [103, 104].

Figure 20 shows the experimentally measured absorption coefficients for several bulk materials [16]. The area between the green dotted vertical lines is the telecom bands between 1310 nm and 1550 nm. In this region, silicon as in the red curve, is transparent and does not absorb light at these frequencies. Instead, InGaAs based devices are often used for telecommunication applications. However, the most popular strategy for improving the performance of silicon-based detectors is to add germanium (Ge) into the material to reduce the bandgap and match with the telecom bands. Figure 20 also shows the influence on the absorption coefficient and penetration depth, which is defined as the distance traveled by light before its intensity drops to 36.7 percent (e^{-1}) of its starting intensity. The data in Figure 20 are for bulk materials without any voltage applied. It is feasible to stretch the curves to longer wavelengths by applying electrical bias [16].This is critical for detection at 1.55 µm photon wavelength, where even a pure Ge film with the proper bias may get shifted in order to lower penetration depth to acceptable levels.

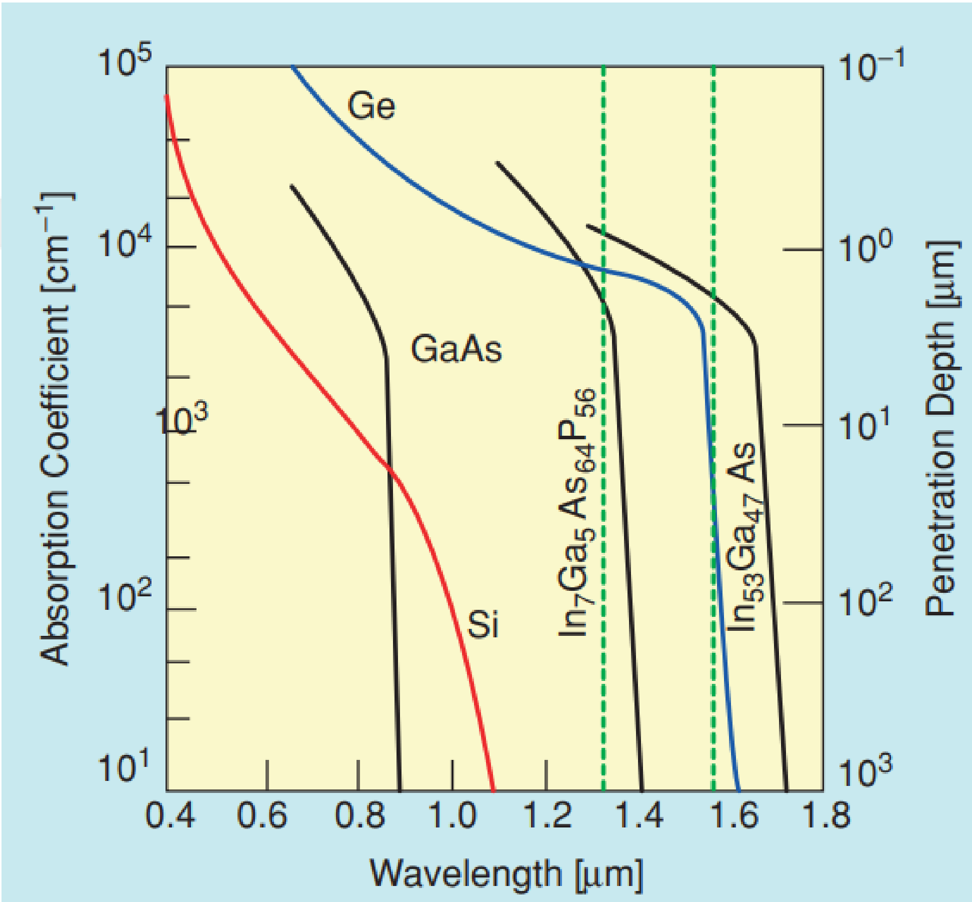

Figure 20: Experimentally measured absorption coefficient values for different materials at different wavelengths. Telecom bands are in between the green dotted vertical lines [16].

As mentioned earlier with the penetration depth, besides the material properties for absorption, the material geometry is also important. According to Lambert's law, the absorbance of a material is directly proportional to its thickness.

$$A = log\left(\frac{P_{transmitted}}{P_{incident}}\right) = log(T) \propto L \quad (2.4)$$

where T is the transmission and L is the penetration depth.

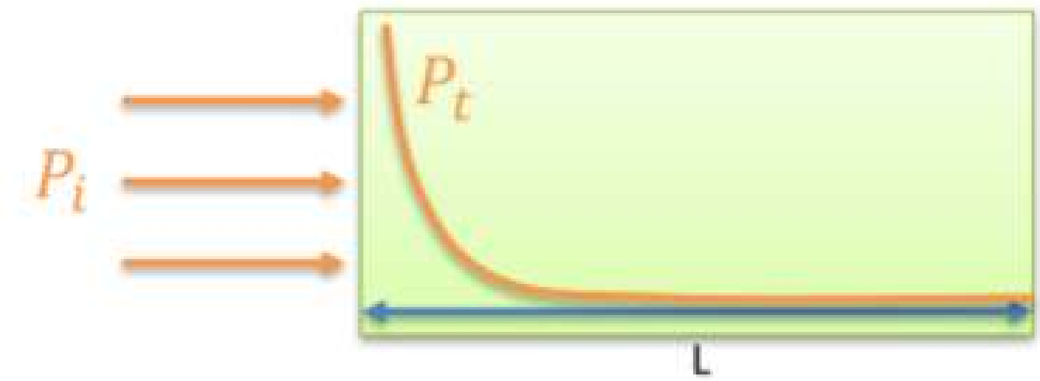

Figure 21: Absorption increases with the thickness of the material [97].

Optical power decreases exponentially as it penetrates a uniform absorbing material as shown in Figure 21. The importance of the absorption and its dependency on the geometry is examined in more detail in the detector geometry part of the study.

2.1.2 Performance Metrics

A photodetector's performance is mainly determined by three important criteria, namely responsivity, bandwidth and dark current [20, 39, 48, 79]. Responsivity is a wavelength-dependent measure of how much electrical current is created per unit optical power received on the detector. The bandwidth is the photodetector's frequency range from DC to cutoff frequency f_{3dB} at which the electrical output power drops by 3dB below power value at very low frequency as depicted in Figure 22. High bandwidth photodetectors are required to detect optical signals modulated at high data rates. The dark current is the current the detector generates even when there is no incident optical power. It occurs due to the random generation of electron and holes within the depletion region of the device. High dark current is not favorable for photodetection with high SNR. In addition to these three-performance metrics, footprint of the photodetector is also important, because it directly affects the production cost and the amount of dark current the photodetector can generate. Therefore, photodetectors with smaller footprints are preferable.

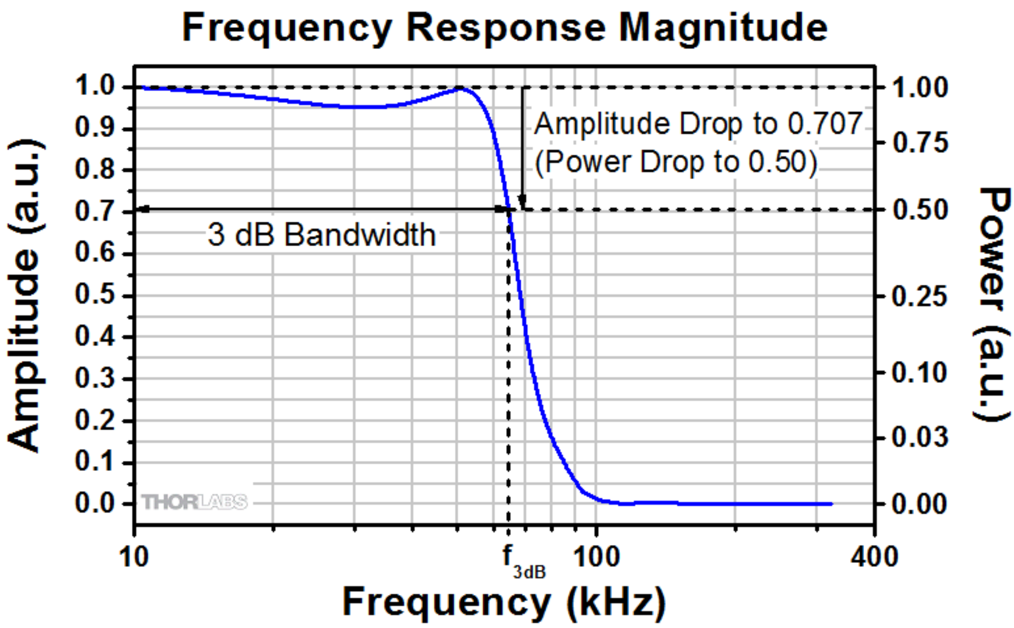

Figure 22: The 3dB bandwidth example for a low-pass filter [106].

Responsivity

Responsivity is the sensitivity of a photodetector in converting optical power to electrical current and is accepted as the most important attribute of a photodetector [79]. The responsivity (R) is simply defined as the ratio of photocurrent (I_{ph}) to incident optical power (P), and is commonly expressed in amperes per watt (A/W) [39].

The quantum efficiency, η, is another term related to responsivity. The likelihood that a single photon incident on the device will form a photocarrier pair that contributes to the detector current is known as quantum efficiency [48]. Since not all incoming photons are absorbed, not all of them form electron-hole pairs. Some photons are reflected at the detector's surface, while others cannot be absorbed due to insufficient absorption length in the material. Furthermore, due to the presence of recombination centers and defects along surfaces, some of electron-hole pairs formed at the detector's surface quickly recombine and are therefore unable to contribute to the detector current. As a result, the external quantum efficiency may be expressed as [48, 107]:

$$\eta = (1 - \mathcal{R})\varsigma(1 - e^{-\alpha d}) \quad (3.1)$$

where $\mathcal{R}$ is the optical power reflectance at the surface, ς is the fraction of electron-hole pairs participating in the detector current (internal quantum efficiency), α is the absorption coefficient and d is the photodetector's absorption length.

The first term, $(1 - \mathcal{R})$ can be increased by using antireflection coatings [48]. The second term, ς, can be increased by lowering the surface recombination rate of electron-hole pairs and eliminating dislocations within the materials. This can be done by an optimized layer growth process and device design. The third term in the multiplication, $(1 - e^{-\alpha d})$, can be maximized with a sufficiently large value of d.

Additionally, the quantum efficiency is a function of wavelength, due to the wavelength dependence of absorption coefficient. The photocurrent spectral range is optimized to match the quantum efficiency spectrum by optimizing the properties of the absorptive semiconductor material. The following relationship is used to convert quantum efficiency to responsivity [39]:

$$R = \eta \frac{q\lambda}{hc} = \eta \frac{\lambda}{1.24} \quad (3.2)$$

where q is the charge of an electron, λ is the wavelength (in μm), h is Planck's constant and c is the speed of light. According to the equation, a detector can have a maximum responsivity of 1.25 A/W at 1550 nm and 1.06 A/W at 1310 nm given a quantum efficiency of 1.

The parabolic shape of the responsivity versus wavelength curves for photodetectors based on different materials in Figure 23 depends on several factors. The geometry of the detector, the absorption coefficient of the semiconductor and quantum efficiency are the most important factors [99]. For very short wavelengths, the penetration depth of photons would be too small as shown in Figure 20. In this case, the photogeneration occurs very close to surface and outside the depletion region. These generated electron hole pairs most probably disappear by recombination without reaching to electrical contacts. Therefore, short wavelength limits occur for the responsivity of the detectors. The long wavelength limit (cutoff wavelength) occurs due to band gap energy of the absorber as discussed in equation (2.3).

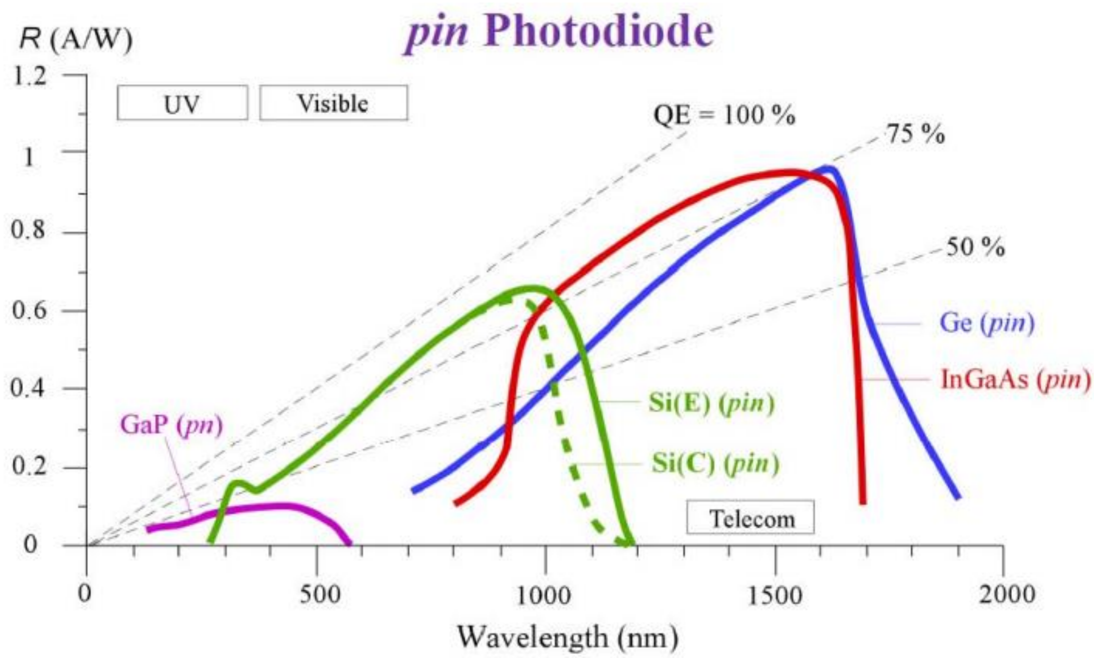

Figure 23: Responsivity vs wavelength of GaP pn type and Si, InGaAs and Ge p-i-n normal-incidence type photodiodes. GaP (Thorlabs FGAP71), Si(E) (Hamamatsu S11499-IR enhanced), Si(C) (Hamamatsu S11499-conventional UV enhanced), InGaAs (Hamamatsu G8376) and Ge (Thorlabs FDG03). Light blue dashed lines represent responsivity at different quantum efficiencies for a wavelength range [99].

Bandwidth

An optical bandwidth is the frequency range that an optical device responds to. It is the spectral width between the points where the signal power is reduced to half of the maximum power point. Therefore, there are two terminal points defining the bandwidth of a signal, namely lower cut-off, and higher cut-off. Optical bandwidth values can be specified in terms of frequency or wavelength, because of the inverse relationship of these terms.

A photodetector's bandwidth is limited due to the maximum detectable modulation frequency of optical power. In general, optoelectronic bandwidth is specified by a 3dB bandwidth which is the frequency point that the signal power is reduced by 3 decibels. The rise time and fall time is directly related to 3dB bandwidth of the photodetector. They are the measure of how fast the detector responds to a modulated optical signal. If they are equal, they may be estimated as $0.35/f_{3dB}$ [106].

Typically for telecommunication applications, the-state-of-the-art photodetectors have 3dB optoelectronic bandwidth on the order of tens of GHz [62, 77, 79, 83, 88]. The carrier transit time and the RC delay are the two key elements that influence a detector's bandwidth [25, 39, 107].

Transit Time

In simplest terms, the transit time is the time it takes for carriers originating from an optical signal to be swept out of the active region of the detector [39]. In doing so, they collide often with lattice ions that are moving about their equilibrium locations due to thermal motion, and phonons, as well as defects in the crystal lattice caused by impurity ions. The carriers experience random decelerations as a result of the collisions, resulting in travel at an average velocity rather than a constant acceleration [48]. The velocity of carriers is determined by:

$$v_i = \mu_i E \tag{3.3}$$

where μ is the carrier mobility, i represents the type of carrier (n or p) and E is the electric field. In the case of a sufficiently high electric field, the velocity of carriers saturates at a point. This phenomenon occurs due to fact that the carrier energy exceeds the optical phonon energy. Thus, the increased probability of emitting an optical phonon causes carrier velocity to saturate with increased electric field. In Table 2, the electron and hole mobilities and saturation velocities for silicon and germanium are given [108]. These values are used in the simulations for the design part of this thesis.

It is also important that the carrier mobilities are also dependent on the doping concentrations and the types of the dopants [109]. The electron and hole mobilities change similarly with respect to doping concentration as shown in Figure 24. For low doping levels, electron and hole mobilities are relatively constant. For high doping levels, carrier mobilities decrease due to ionized impurity scattering with the ionized dopants [109]. Since the photogeneration process predominantly occurs in the intrinsically doped region, mobilities of the electron-hole pairs are relatively low.

Table 2: Silicon and germanium carrier mobility and saturation velocity parameters [108].

	e^- (Si)	h^+ (Si)	e^- (Ge)	h^+ (Ge)
Mobility (cm^2/Vs)	1450	500	3900	1900
Sat. Velocity (m/s)	$1x10^5$	$0.7x10^5$	$0.7x10^5$	$0.63x10^5$

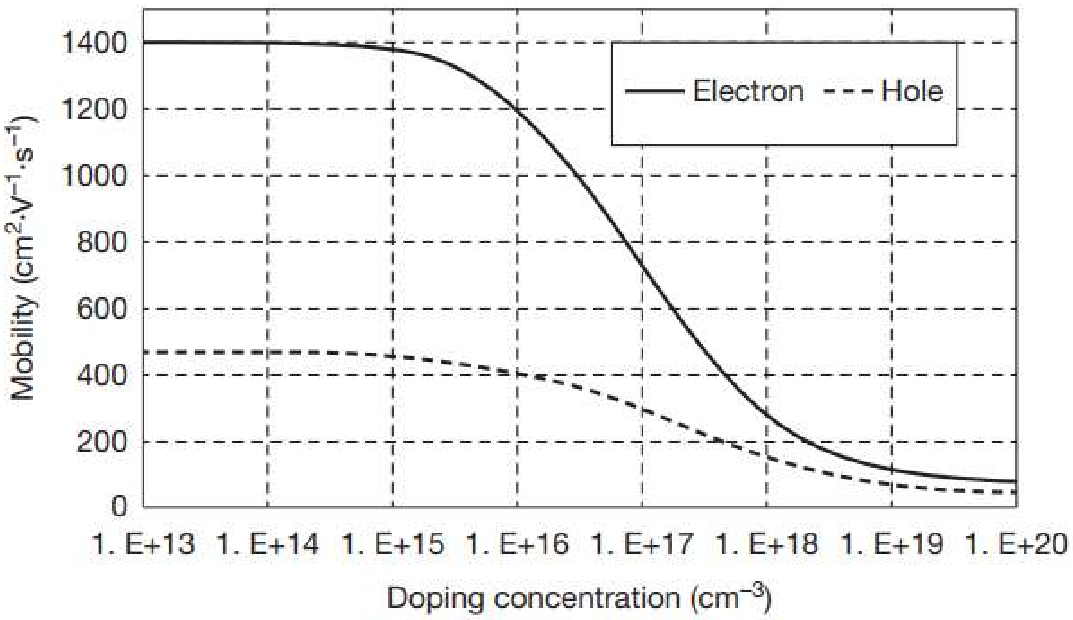

Figure 24: Electron and hole mobility versus doping concentration for silicon at 300°K [110].

The bandwidth originating from carrier transit time can be expressed as [108]:

$$f_{transit} = 0.44\frac{v_{sat}}{W_D} \tag{3.4}$$

RC Response

The electrical impedance characteristics of the photodetector is the second component in defining the bandwidth of a detector [20, 39, 48, 79]. As with any electronic circuit, detectors are also affected by RC charging delay. The effective series resistance between anode and cathode contacts is mainly stem from the resistivity of the doped semiconductor material and contact resistances. The capacitance, on the other hand, is determined by the depletion layer (junction) capacitance. As demonstrated in Figure 25, electrical effects are usually reduced to an RC circuit model for detector. The photodetector is illustrated as a current source, I_{PD}, in the dashed box, with a parallel capacitor C_{PD} and a resistor R_{PD}. A second resistor, R_{load}, represents the load circuit connected to photodetector.

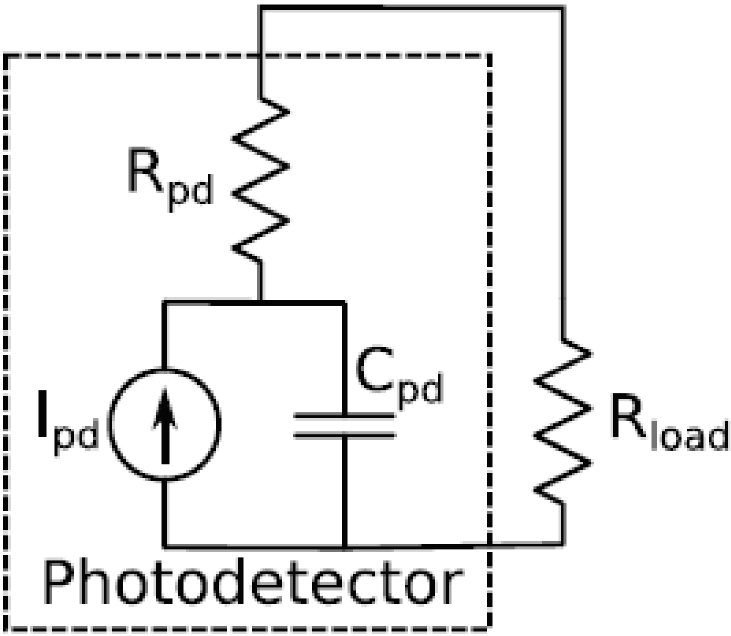

Figure 25: Photodetector RC circuit model [39].

Further considerations on carrier mobility and doping concentrations are required to understand their effects on resistivity of a semiconductor [100]. In doing so, the series resistance of the photodetector, R_{PD}, can be calculated.

The resistivity of a material is defined as the applied electric field divided by the current density [96]. The equation for total current density is already given in equation (1.3), which includes both the electron and hole current densities. Therefore, the resistivity can be expressed as in equation (3.5). Figure 26 shows that the resistivity of the material is inversely proportional to doping concentrations.

$$\rho = \frac{E}{J} = \frac{1}{q(\mu_n n + \mu_p p)} \tag{3.5}$$

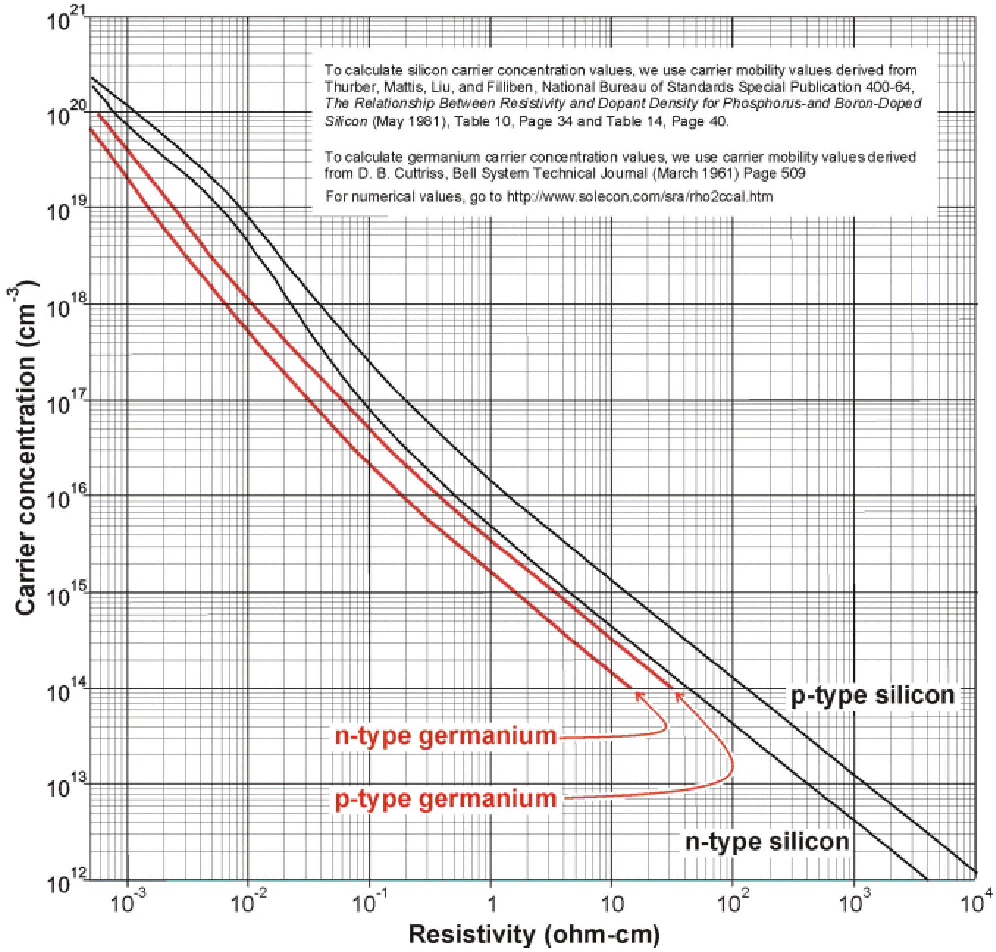

Figure 26: Resistivity versus carrier concentration [111].

The capacitance of the p-i-n detector is mainly determined by the junction capacitance and can be formulated similar to parallel plate capacitor where A is the cross-sectional area and ε_s is the permittivity of semiconductor.

$$C_{PD} = \frac{\varepsilon_s A}{W_D} \tag{3.6}$$

The bandwidth originating from RC response of the detector can be calculated as in equation (3.7) where R_{load} is generally 50Ω for telecommunication applications [39]:

$$f_{RC} = \frac{1}{2\pi(R_{load} + R_{PD})C_{PD}} \tag{3.7}$$

As a result, the total bandwidth can be calculated by including the effects of both transit time and RC response [25, 39, 107].

$$f_{3dB} = \left(\frac{1}{f_{RC}^2} + \frac{1}{f_{transit}^2}\right)^{-\frac{1}{2}} \quad (3.8)$$

Dark Current

Photodetectors produce dark current, which is the current output when there is no light input. It is an unwanted property of vertical p-i-n germanium photodetector that is caused by the material defects in germanium layer as well as finite thermal effects that excite electron from valence band to conduction band [39]. Under a strong electric field, the Shockley-Read-Hall process will cause these defects to become active current leakage channels [20, 39, 48]. The total dark current is influenced by two factors: bulk generation and surface generation [112].

Bulk generation is a volume-dependent mechanism [39]. Threading dislocations are caused by the significant lattice mismatch between silicon and germanium, allowing for the development of mid bandgap states [20]. The bulk current density is essentially stable at low electric fields. Band bending, on the other hand, results in a greater bulk current density that grows exponentially with the applied electric field [39].

Surface generation, which is caused by surface defects such as dangling bonds, is the second component to the dark current [39]. Since germanium is not entirely passivated by silicon dioxide, and it is not an easy process as in silicon passivation, the formation of minority carriers on the Ge layer surface due to the poor passivation quality of silicon dioxide causes surface leakage current [112]. Thus, the total dark current can be expressed as [113]:

$$I_{dark} = I_{bulk} + I_{surface} = J_{bulk} \times A + J_{surface} \times \sqrt{4\pi A} \quad (3.9)$$

where A is the detector area, J_{bulk} and J_{surf} are the current densities for bulk and surface components, respectively.

$$J_{surface} = q \times S \times n_{i,Ge} \times t \quad (3.10)$$

$$J_{bulk} = q \times \frac{n_{i,Ge}}{\tau} \times t \quad (3.11)$$

The minority carrier generation on the germanium sidewalls can be expressed as in equation (3.10) for a reverse biased photodiode where q is charge, S is surface recombination velocity, $n_{i,Ge}$ is intrinsic carrier concentration and t is the thickness of depletion region [114]. Similarly, the minority carrier generation process inside the bulk germanium region can be expressed in equation (3.11) where τ is the minority carrier lifetime [114]. These two equations show that thickness of the germanium region which is equal to depletion region thickness also linearly affects the dark current.

2.1.3 Detector Geometry

To create a germanium-on-silicon photodetector, a number of important design decisions must be made. Depending on the p-i-n junction orientation, two commonly used orientations available for the p-i-n detectors are vertical and lateral. The vertical orientation which we are focusing throughout this study is shown in Figure 27. In this orientation, a silicon waveguide taper couples incident light from a single-mode silicon waveguide to the Ge waveguide. An intrinsic (undoped or slightly doped) region is sandwiched between p-doped and n-doped area. Since germanium has a direct band gap energy of $E_g = 0.8\, eV$ [104] and germanium's refractive index is higher than that for silicon ($n_{Ge} = 4.275$, $n_{Si} = 3.48$) [103, 104], the optical mode leaks into germanium from silicon waveguide and gets absorbed in germanium intrinsic region. When a reverse bias voltage is applied to p-i-n diode, the photo-generated carriers can be efficiently collected by drifting along the constructed electric field, provided that surface and bulk recombination rates are minimized. Thus, external photocurrent is generated.

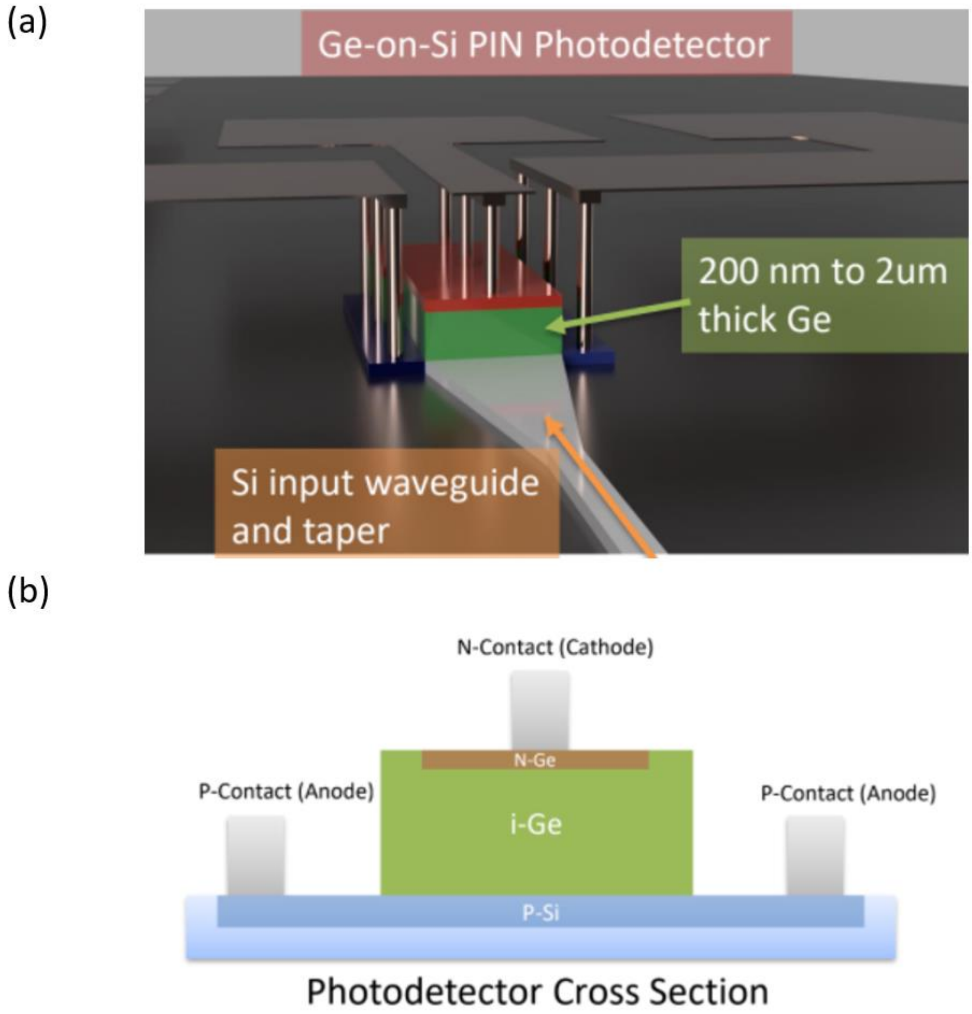

Figure 27: Ge p-i-n photodetector geometry (a) isometric view (b) cross-section view. Reverse-bias is applied by having the electrical potential at anode contacts higher than the cathode contact [97].

The following are some of the benefits of photodiodes with a p-i-n structure [48]:

- Increasing the size of the device's depletion layer improves the area accessible for absorbing light.
- By increasing the thickness of the the depletion layer, the junction capacitance and hence the RC constant are reduced. However, increased depletion region thickness also increases the transit time. Thus, a trade-off may emerge between RC or transit-limited photodetection regimes in designing fast photodetectors.

- By lowering the ratio between the device's diffusion and drift lengths, a higher proportion of the produced current is transported by the faster drift process.

In the following sections, how the different geometries of epitaxially grown germanium on silicon affect the performance metrics of the device is evaluated.

Detector Length

Considering a light incident on an absorptive material with no geometric variation in the incidence direction, the transmitted optical power will be [39],

$$P_{transmitted} = P_{incident}e^{-\alpha(\lambda)L} \quad (4.3)$$

where α is the absorption coefficient which is a function of the wavelength and L is the length of the absorptive material. Therefore, the absorbed light can be calculated with the below equation [39].

$$P_{absorbed} = P_{incident} - P_{transmitted} = P_{incident}(1 - e^{-\alpha(\lambda)L}) \quad (4.2)$$

According to the preceding equation, the absorbed power and hence the detector's responsivity will grow as a function of length. This relation has been validated by several experimental results and by finite-difference time domain waveguide models [20, 25, 39, 79, 92].

On the other hand, if we take a p-i-n photodetector with a fixed width, however, the total capacitance of the detector may be calculated using the following formula where C_l is the capacitance per unit length [39]:

$$C = C_l \, . L \quad (4.3)$$

Therefore, as the length of the detector is increased, the capacitance increases, and bandwidth may decrease due to RC delay. Figure 28 shows the effect of photodetector length on responsivity and bandwidth [39]. The tradeoff between responsivity and bandwidth is an important design consideration. As detector length is increased, more and more light is absorbed and therefore, responsivity increases. On the other hand, the bandwidth decreases due to increased RC delay with length increase.

As given in equation (3.9), dark current increases with the area of the germanium region. The area increases with length, and increases the dark current [114].

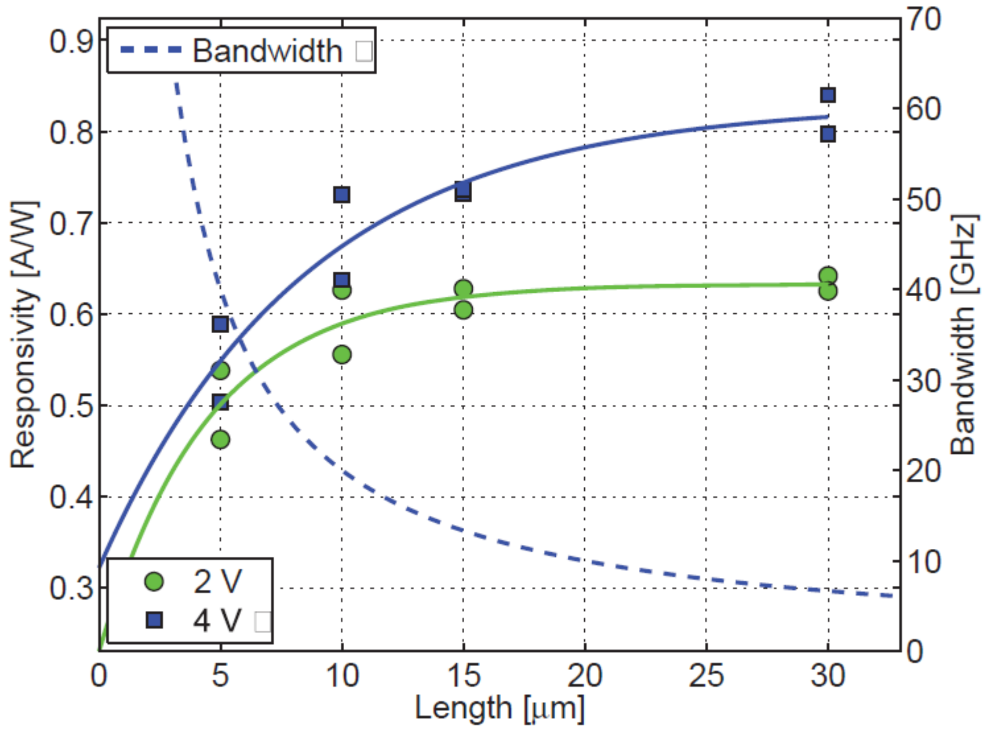

Figure 28: Responsivity and bandwidth versus length of the detector. Two different color responsivity curves are given at 2V and 4V reverse-bias in green and blue, respectively. The blue dotted curve shows the bandwidth. For shorter detectors carrier transit time is the limiting factor, whereas for longer detectors RC response limits the bandwidth [39].

Detector Width

Detector width refers to the width of germanium layer on top of silicon for vertical germanium p-i-n photodiodes [20, 39, 79, 92]. The responsivity of the detector is mainly dependent on the waveguide-to-photodetector coupling efficiency [115]. The optical coupling from waveguide to detector is similar to coupling in between two waveguides as in the case of directional couplers. The phase-matching is important for efficient coupling. When an efficient evanescent coupling occurs into germanium, the optical power oscillates between the waveguide and germanium layer. In this evanescent coupling mechanism, when the phase-matching condition is satisfied, the mode vertically oscillates and varying the width of germanium has no significant effect on coupling behavior [115].

However, a wider germanium area increases the detector capacitance and decreases the bandwidth of the detector due to RC delay. In addition to that, as both bulk and surface rates are increased with the area, dark current will increase correspondingly as in equation (2.8) [92]. Therefore, choosing a sufficiently small device width improves the bandwidth and dark current performance metrics, while it does not affect the responsivity as much. On the other hand, there is a consequence that arises once the detector is sufficiently small [39]. The contact sizes may need to be lowered in order not to overlap as the width of the detector decreases, thereby contact resistance may begin to limit bandwidth.

Detector Height

The height of germanium epitaxially grown on silicon has two limits [39]. Due to the lattice and thermal coefficient of expansion mismatch between silicon and germanium, a buffer region is required to limit the defects in fabrication. The height of this buffer region is in general 20-50 nm. The buffer region should be kept small in proportion to total detector height because of having significant number of defects. Therefore, assuming the buffer region to be kept twenty percent of the total germanium height, a typical lower limit for the detector height can be around 200 nm [39]. The upper limit of the height of the detector is determined by the fact that the evanescent tail of the light exponentially decays and there is no significant advantage of further epitaxial growth of germanium. In practice, 2μm is commonly used as an upper limit [39].

Intuitively, as the thickness of the detector is increased the responsivity should also increase as much the amount of light is absorbed. However, the absorption profile depends on the overlap between higher-order mode and input mode. The optical coupling from waveguide to photodetector can be treated as coupling from waveguide to waveguide. Since the oxide layer surrounding the photodetector provides high index contrast for photodetector, unabsorbed photons can be confined in the photodetector with the help of total internal reflection. In order to achieve efficient coupling, phase-matching between the two waveguides is the key factor [115].

In their study, Ahn et al. presented a methodology to characterize the coupling efficiency depending on the photodetector thickness and wavelength [115]. In their leaky-mode phase-matching model, they are suggesting that the photodetector thickness that minimizes $\left|n_{eff,WG} - n_{eff,PD}\right|^2$ also maximizes absorption rate. The interval between the peaks, Δd, can also be found by the below equation where λ_0 is the wavelength, θ is the reflection angle of the wavefront against the silicon-germanium interface.

$$\Delta d = \frac{\pi}{\left(\frac{2\pi}{\lambda_0} n_{eff,PD}\right)\sqrt{1 - \cos^2\theta}} \tag{4.4}$$

Piels et al. simulated quantum efficiency of a 20μm long photodetector by changing both the germanium thickness and the underlying silicon thickness as shown in Figure 29. There is a peak-valley behavior in efficiency with respect to change in germanium thickness. Moreover, in case of the underlying silicon thickness increased, these valleys deepen [20]. Even though the trendline of responsivity increases with the thickness of germanium, the peak-valley behavior should be examined to optimize the responsivity in detector designs.

Another factor to consider when choosing a detector height is the influence it will have on the bandwidth of the photodetector. As it is already mentioned in equation (3.4) depletion region width directly plays a role in carrier transit time. Since a short detector has a short depletion region, carrier transit time is low and therefore, $f_{transit}$ is high. On the other hand, junction capacitance of the detector is inversely proportional with the depletion region width as it is mentioned in equation (3.6). Thus, a short detector has a greater junction capacitance and therefore a lower RC bandwidth. Similarly, a tall detector has a longer carrier transit time, but a low RC latency [39]. The tradeoff between transit time and RC delay may be evaluated using a basic model of a vertical PIN, as illustrated in Figure 30. For this example, for around 0.8μm germanium height, the optimal bandwidth around 20 GHz can be achieved. However, it is evident that by increasing the thickness of germanium, bandwidth decreases due to longer carrier transit time. Similarly, when the thickness of germanium is sufficiently low, due to capacitance increase, RC delays can play a role on limiting the bandwidth of detector.

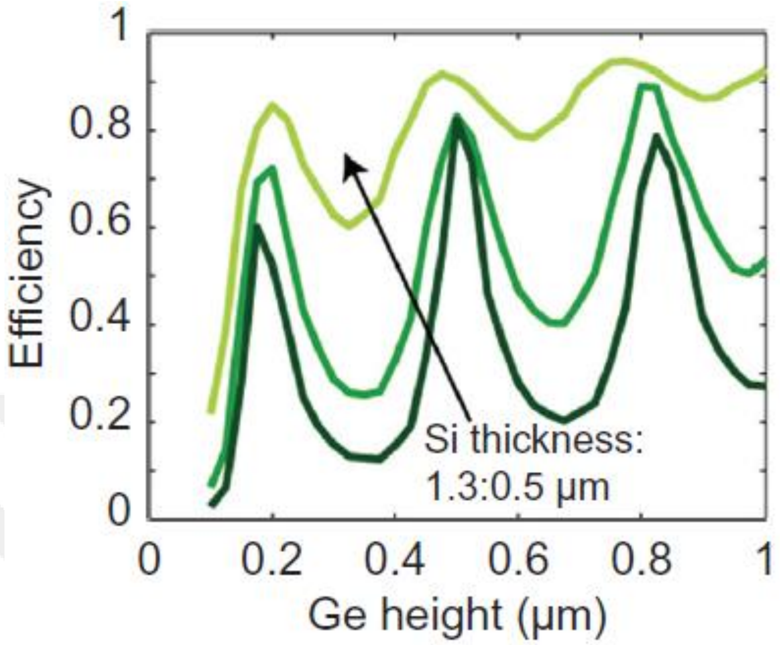

Figure 29: Coupling efficiency vs device thickness. The peak-valley behavior is observed and coupling efficiency is maximized when phase-matching occurs in between photodetector and waveguide [20].

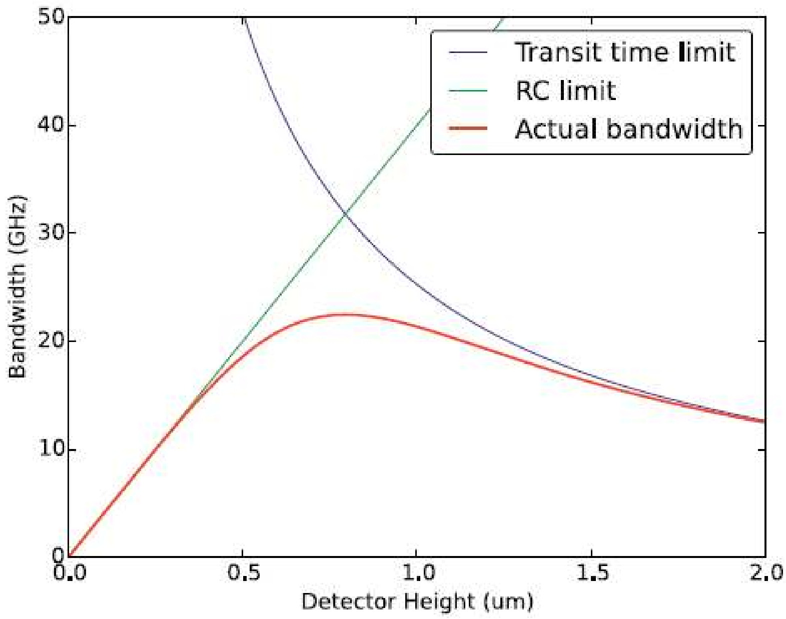

Figure 30: Transit time vs RC delay effects on detector bandwidth [39].

In terms of dark current, as shown in equations (2.9) and (2.10), with the increased germanium thickness, linear increment in the dark current is expected. However, experimental results show that increasing the thickness improves the layer quality and therefore, decreases the dark current as shown in Table 3 [92]. This may be result from the fact that as the layer quality is improved, defect density in Ge layers decreases which also decreases the carrier generation-recombination process.

Table 3: Dark current vs device thickness [92].

Thickness (nm)	**Area (μm^2)**	**Dark Current (µA)**
300	2500	11.1
700	2500	8.44
1000	2500	5.55

2.1.4 Vertical p-i-n Ge Photodetector Equivalent Circuit Model

The equivalent circuit model of vertical p-i-n germanium photodetector is shown in Figure 31. In this model, C_J is the junction capacitance of the reversed biased p-i-n junction. R_{S1} *and* R_{S2} are series resistances to p-i-n junctions due to doped regions and anode contacts. In order to calculate the total series resistance, due to symmetry in the device, R_{S1} *or* R_{S2} could be found and divided by two as they are in parallel. There is also a resistance due to cathode contact and n doped Ge region, but it is negligibly small (on the order of few mΩ) and therefore not shown in the equivalent circuit model.

In addition to junction capacitance, there is also a shunt resistance R_{sh} that is in parallel with the other components in the circuit model. In general, it is measured experimentally by applying $\pm 10\ mV$ to the contacts and can be calculated by dividing the applied voltage to measured current [116]. In photovoltaic mode, shunt resistance is the determining parameter for noise current calculation, so that the highest shunt resistance is desired for a better photodetector performance.

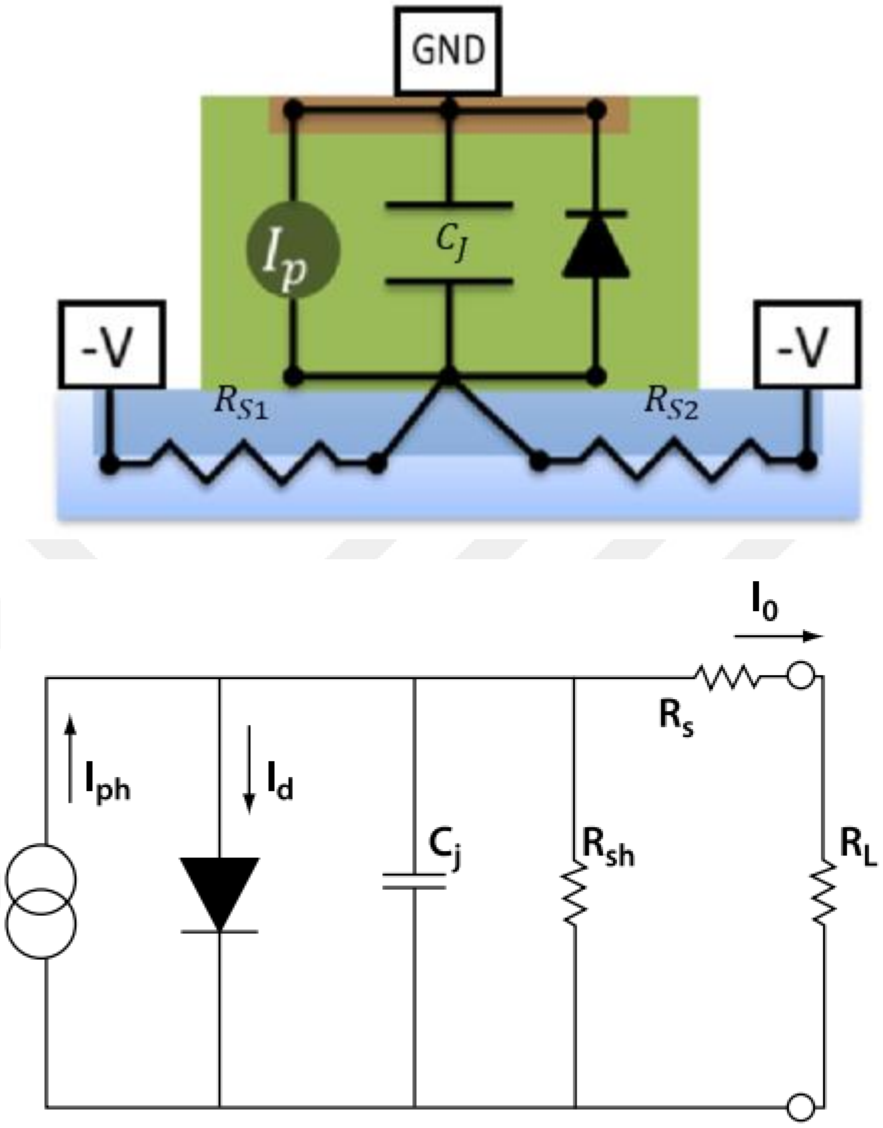

Figure 31: Equivalent circuit model for VPIN Ge Photodetector [116].

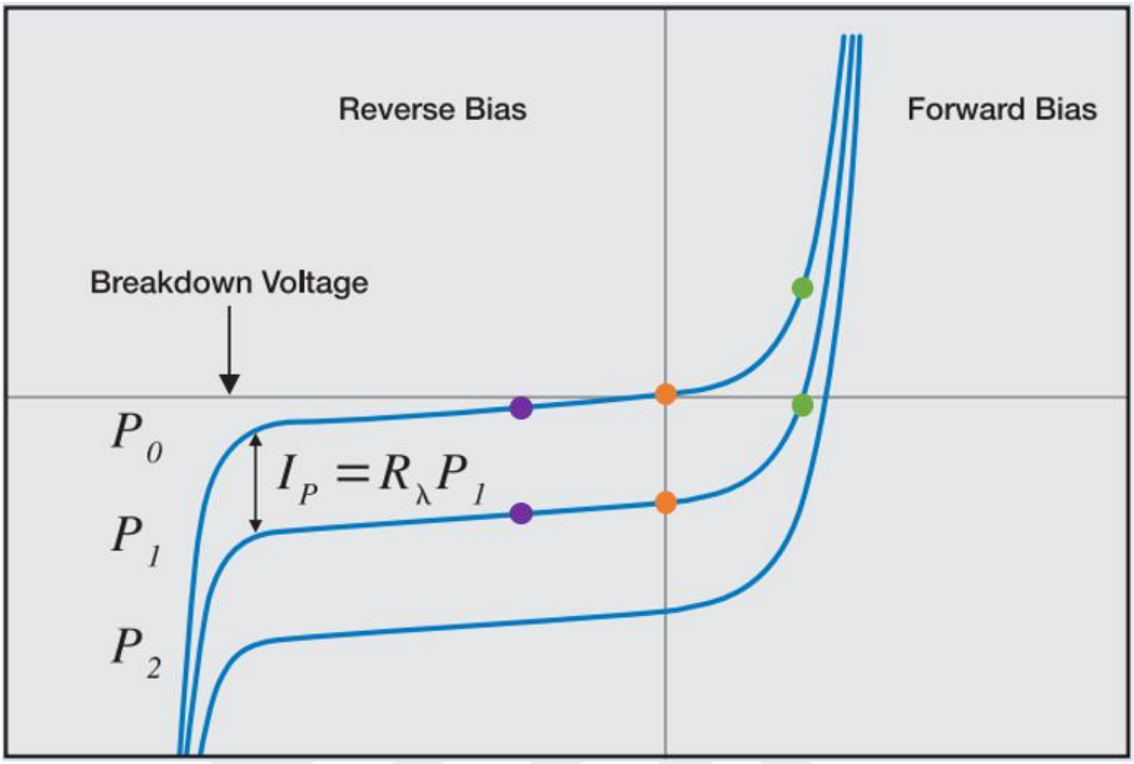

Figure 32: IV Characteristics in dark and under illumination for different operation regimes. Purple, orange, and green dots show the reverse bias, zero bias and forward bias of operations, respectively. P_0, P_1 and P_2 represents different illumination levels.

Using photodetector under reverse bias or zero bias, as shown in Figure 32 (purple and orange dots, respectively), the ratio of photocurrent to dark current is maximized which is directly related to SNR performance of the photodetector. However, at forward bias, even negative SNR values are expected. The current-voltage characteristics of photodetector with no incident light can be represented by Eq. (4.5) where I_D is the dark current and it is related to reverse-bias saturation current. Under illumination, the I-V curve is shifted below as in Figure 32 and the total current can be expressed as in Eq. (4.6) where I_P is the photocurrent.

$$I_D = I_{SAT}\left(e^{\frac{qV_{bias}}{k_B T}} - 1\right) \tag{4.5}$$

$$I_{Total} = I_{SAT}\left(e^{\frac{qV_{bias}}{k_BT}} - 1\right) - I_P \qquad (4.6)$$

2.2 *Noise Analysis in Optical Receiver Design*

Figure 33 schematically depicts an optical receiver that contains a photodetector, a transimpedance amplifier (TIA), a filter, a main amplifier (MA) and the decision circuit [117]. As it is the lowest signal point, the optical receiver dictates the performance of the whole system [116].

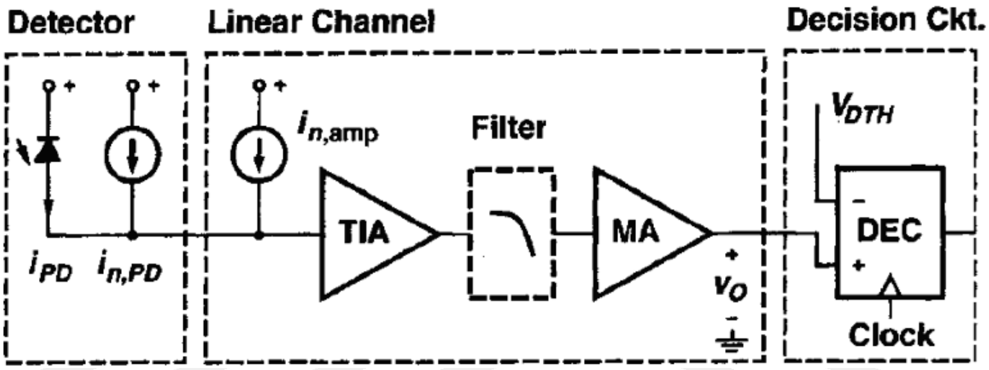

Figure 33: Basic optical receiver model [117].

In an optical receiver used for digital communication, photodetector generates photocurrent in proportion to incident optical power. Then, TIA converts the photocurrent to a voltage signal and finally main amplifier brings this voltage to a standard level to be used by decision circuit. The photodetector and TIA performance are the key determinants of the sensitivity of an optical receiver [25].

In germanium-on-silicon p-i-n photodetectors there are two sources of noise can be identified: shot noise and Johnson (thermal) noise [116]. From the photodetector perspective, shot noise is generally the major noise component which occurs with the random arrival of photons to the device and mainly depends on the dark current and noise bandwidth which can be represented as [39]:

$$I_{sn} = \sqrt{2qI_{dark}BW} \qquad (5.1)$$

where I_{dark} is the dark current, and BW is the bandwidth of the photodetector. Wider bandwidths, as seen in the formula, place higher constraints on the dark current in order to maintain the same signal-to-noise ratio. Therefore, shot noise limits detector bandwidths.

Johnson noise, on the other hand, is due to the thermal generation of carriers and all resistors have a Johnson noise associated with them. This type of noise is dominant current noise in photovoltaic operation mode where the photodetector is unbiased [116]. The Johnson noise of the photodetector can be formulated as:

$$I_{jn} = \sqrt{\frac{4k_B TBW}{R}} \tag{5.2}$$

where k_B is the Boltzmann constant, T is the absolute temperature in degrees Kelvin and R is the load resistance of the photodetector, typically 50 Ω. Typical noise values for Johnson noise and shot noise (assuming $100\ nA$ dark current) are $1.82 \times 10^{-11}/\sqrt{Hz}$ and $1.79 \times 10^{-13}/\sqrt{Hz}$, respectively.

The total noise generated by the photodetector, therefore, can be expressed as:

$$I_{tn} = \sqrt{{I_{sn}}^2 + {I_{jn}}^2} \tag{5.3}$$

Therefore, the minimum detectable power, in other words noise-equivalent power (NEP) can be found by dividing the total noise current to responsivity [116]. Photodetector NEP values can vary from $10^{-11}\ W/\sqrt{Hz}$ to $10^{-15}\ W/\sqrt{Hz}$ for large active area photodetectors and small active area photodetectors, respectively [101].

$$NEP = \frac{I_{tn}}{R}\left(\frac{A/\sqrt{Hz}}{A/W}\right) \tag{5.4}$$

The electrical amplification of a receiver, on the other hand, usually makes up the majority of the noise in a receiver [116]. In a photoconductive mode of operation, dark current-induced noise can thus be insignificant depending on the application.

In a digital optical communication system, the binary data stream is sent by modulating the optical signal. During the bit time period, an optical signal with non-return-to-zero (NRZ) coding can have one of two states of optical power level. Figure 34 shows optical logic levels where logic-level 1 relates to high optical power (P1), whereas logic-level 0 relates to low optical power (P0). It is important to mention that in a real case, when transmitting logic-level 0, optical power is not equal to zero.

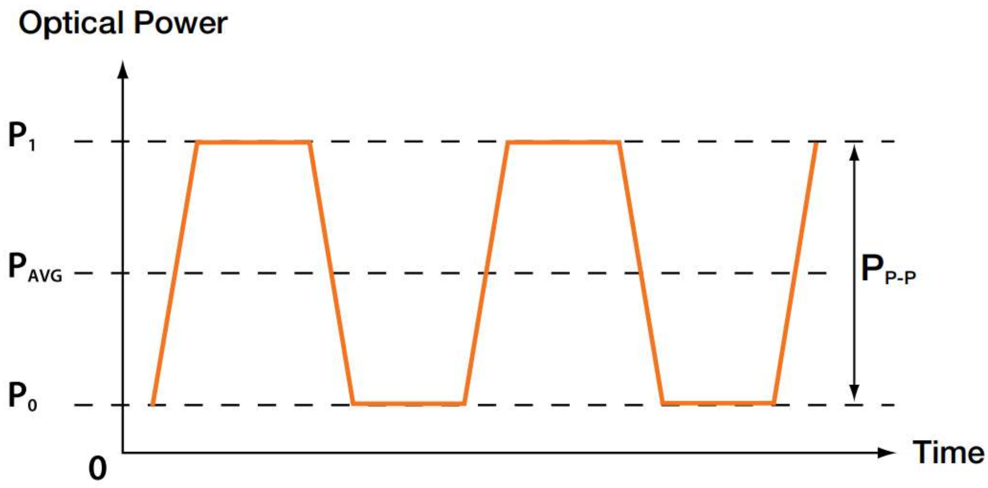

Figure 34: Optical power levels [116].

The number of errors at the decision circuit's output determines the receiver's quality. The bit-error-rate (BER) is the proportion of detective count bit to the total number of bits sent. The sensitivity of the receiver, S, is defined as the minimum optical power of the incident optical signal required to maintain the desired bit-error-rate [116].

In binary optical communications, the optical signal-to-noise ratio (OSNR) is the figure-of-merit for qualitatively measuring the performance at the receiving end. It combines the separate SNRs associated with the high and low levels into overall system SNR [118]. As indicated in below formula, it can theoretically be used to calculate the signal quality of electrical data generated by an optical receiver:

$$OSNR = \frac{I_1 - I_0}{\sigma_1 + \sigma_0} = \frac{I_1 - I_0}{\sqrt{i_{sn,1}^2 + i_{amp}^2} + \sqrt{i_{sn,0}^2 + i_{amp}^2}} \tag{5.5}$$

In this equation, $i_{sn,1/0}^2$ is the shot noise current originated from p-i-n photodetector at bit 1 and bit 0 level, respectively. i_{amp}^2 is the electrical amplification noise current originated from TIA. The form of the OSNR given in equation (5.5) simplifies both the measurement of SNR and the calculation of the theoretical BER due to additive random noise.

$$\log_{10}(BER) = 10.7 - 1.45(OSNR) \tag{5.6}$$

Equation (5.6) shows the relationship between bit error rate (BER) and OSNR [119]. For example, in order to have an error-free reception with a bit error rate of 1×10^{-12}, the OSNR should be $15.65\ dB$. Alternatively, OSNR can be derived in a similar formula including the responsivity in the equation as [25]:

$$OSNR = \frac{\sqrt{R}\ (P_1 - P_0)}{\sqrt{2qP_1BW + \frac{i_{amp}^2}{R}} + \sqrt{2qP_0BW + \frac{i_{amp}^2}{R}}} \tag{5.7}$$

where $P_1\ and\ P_0$ is the optical input power incident on Ge p-i-n photodetector at bit 1 and bit 0 level, respectively, and BW is the noise bandwidth of the optical receiver. It is evident that to obtain higher sensitivity, or higher OSNR, the photodetector responsivity should be as high as possible, whereas the shot noise and the amplification noise should be as low as possible.

2.3 Application Based Receiver Characteristics

In this section of the thesis, photodetector performance requirements are determined for each application. In doing so, commercial examples are analyzed, and optical power link budgets are calculated for estimating the sensitivity requirements of the photodetector designs for desired OSNR levels.

2.3.1 OTDR Application (Sensing)

Optical time domain reflectometry (OTDR) is a measurement technique commonly used for characterization of optical fibers and fiber-optic communication systems and the optoelectronic device using this technique is called optical time domain reflectometer as depicted in Figure 35 [120]. Rayleigh backscattering in the fiber plays a crucial role for the functioning OTDR systems. The operation principle of OTDR is based on sending a series of light pulses and analyzing the returning optical signals resulting from the Rayleigh scattering and reflections from fiber connectors, splices etc. which is similar to a one-dimensional radar system [121].

A basic OTDR circuit is shown in Figure 36. The OTDR device emits short laser pulses. These pulses are injected through the device under test, an optical fiber. Any reflected light due to thermal drift (temperature sensing) [122, 123], strain (pressure, strain, or vibration sensing) [124-126], and acoustic noise (audio sensing) [127, 128] is extracted with a directional coupler and detected by a high-sensitivity photodetector. This allows a time domain measurement of the reflected optical signal power.

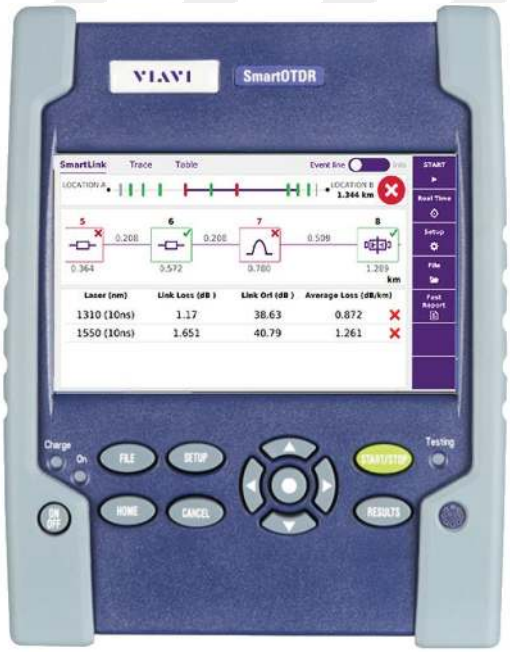

Figure 35: A commercially available example of OTDR signal source and read-out device by Viavi Solutions [43].

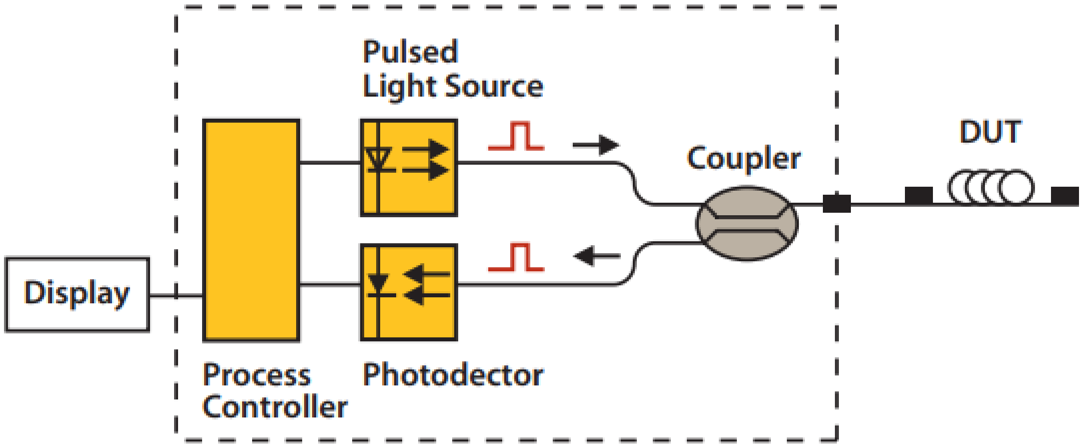

Figure 36: Basic OTDR Setup [129].

In an OTDR system, the location of a reflection point is determined by the time delay between the launched light pulse and the corresponding Rayleigh backscattered signal and can be expressed as [130, 131]:

$$x = \frac{c \times \tau}{2n_g} \tag{6.4}$$

where τ is the time delay, c is the propagation speed of light in the fiber, n_g is the group index of the fiber, and x is the distance of the reflection point from the reference. Since the emitted light travels the distance from where it is backscattered two times, there is a factor of two in the denominator. The spatial resolution, Δx of the measurement can be expressed as:

$$\Delta x = \frac{c \times T_P}{2n_g} \tag{6.2}$$

where T_P is the pulse width. The power of the backscattered signal at a distance l from the reference can be calculated as:

$$P_{scattered} = \frac{1}{2} F \times \alpha_S \times v_g \times \tau \times P_{input} \times e^{-2\alpha l} \tag{6.3}$$

where F is the capture coefficient, α_S is the Rayleigh scattering coefficient, v_g is group velocity in the fiber, P_{input} is the input power and α is the fiber loss coefficient. In order to calculate the optical loss budget in an OTDR circuit, typical attenuation values of different fiber components to consider are [129]:

- 0.2 dB/km for single-mode fiber loss at 1550 nm wavelength
- 0.05 dB for a fusion splice
- 0.3 dB for a mechanical splice
- 0.5 dB for a connector pair
- 3.5 dB for a 1 to 2 splitter (3 dB splitting loss + 0.5 dB excess loss)

The fact that the laser signal travels many kilometers and is reflected back by undergoing various power losses causes the signal reaching the photodetector to be of very low power. Therefore, the most important requirement for the photodetector at the receiver end is that it must be able to detect extremely low power levels of backscattered light [129]. Table 4 shows an example of loss budget calculation for short, medium, and long-haul applications.

Table 4: Example of typical optical loss budget calculation [129].

Network	**Short Haul**	**Medium Haul**	**Long Haul**
Laser (dBm)	16	16	16
Isolator (dB)	-0.7	-0.7	-0.7
Fiber Coupler (dB)	-5.428	-5.428	-5.428
Number of couplers	3	3	3
Total Coupler Loss (dB)	**-16.284**	**-16.284**	**-16.284**
MZ-Modulator (dB)	-10.77	-10.77	-10.77
EDFA (dB)	30	30	30
Circulator (dB)	-1	-1	-1
Optical Power Entering Fiber (dBm)	**17.246**	**17.246**	**17.246**
Distance (km)	30	80	200
Fiber loss (dB/km) at 1550 nm	-0.25	-0.22	-0.19
Total Fiber Loss (dB)	**-7.5**	**-17.6**	**-38**
Number of splices	15	40	50

Average splice loss (dB)	-0.1	-0.1	-0.05
Total Splice Loss (dB)	**-1.5**	**-4**	**-2.5**
Number of connectors	2	2	2
Average connector loss(dB)	-0.5	-0.5	-0.5
Total Connector Loss (dB)	**-1**	**-1**	**-1**
Power at the Detector (dBm)	**7.246**	**-5.354**	**-24.254**

In OTDR systems, dynamic range is the difference between the maximum signal power that can be detected by the receiver and noise power of the receiver in dB terms. As the received input optical power increases, SNR also increases proportionally, and OTDR event detection becomes more sensitive and specific. Figure 37 shows the different representations of dynamic range depending on the different noise levels. OTDR systems generally use RMS dynamic range in their specifications documents.

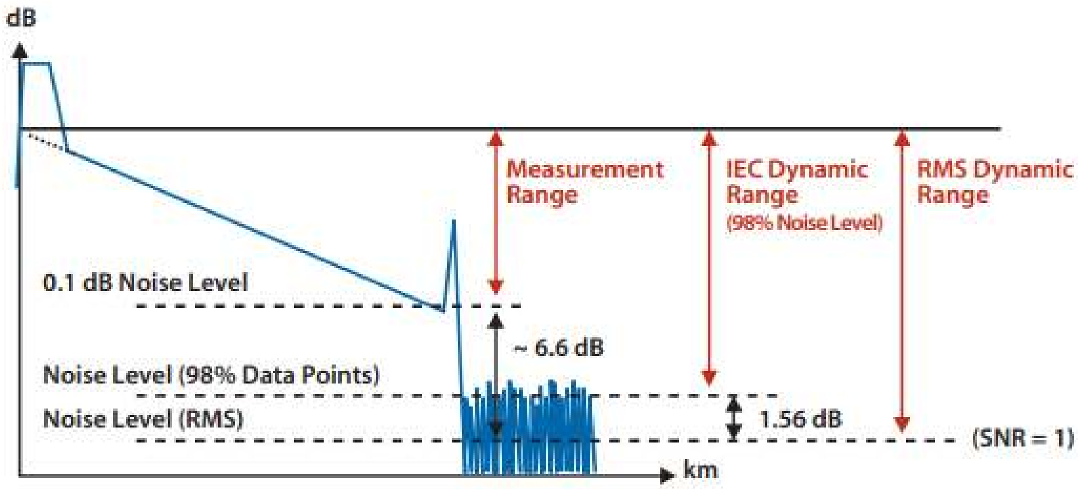

Figure 37: Different definitions of dynamic range [129].

In a typical application, laser diodes send pulses from 10 mW to 1 W into the fiber ($10 - 100\ dBm$). These interrogation pulses have a frequency of several kilohertz and have a pulse width of 2 ns to 2 μs [129]. However, in order to take the requirements to the next level, we will consider portable OTDR instruments, which have lower power consumption and therefore send a lower power laser signal. For example, SmartOTDR 100AS is a commercially available OTDR device manufactured by Viavi Solutions. In this device, output power of the light source is -3.5 dBm which is around 0.45 mW and operates at 1 kHz frequency [43]. In the datasheet of SmartOTDR 100AS, the device has been reported to have 30 dB RMS dynamic range.

Since in an OTDR application optical signal frequencies are on the order of a few kHz, shot noise on the photodetector output signal can be safely ignored. For example, at an operating frequency of 1 kHz with a detector having a dark current of 100 nA, shot noise will be calculated as in the equation (5.1):

$$i_{sn} = \sqrt{2 \times 1.602 \times 10^{-19} \times 100 \times 10^{-9} \times 10^{3}} = 5.66 \times 10^{-12}\ A$$

On the other hand, we can similarly calculate the Johnson noise with assuming load resistance of 50 Ω at 300 degrees of Kelvin as in the equation (5.2):

$$i_{jn} = \sqrt{\frac{4 \times 1.38 \times 10^{-23} \times 300 \times 1000}{50}} = 5.75 \times 10^{-10}\ A$$

Therefore, the total noise can be found by adding the squares of shot noise and Johnson noise and taking the square root of the summation:

$$i_{tn} = 57.5\ nA$$

The resulting total noise current is at a comparable level to the dark current (100 nA). Therefore, the minimum detection limit can be found by adding total noise to the dark current level. Considering a detector with a responsivity of $1\ A/W$, the noise-equivalent-power (NEP) can be calculated as:

$$NEP = \frac{157.5\ nA}{1\ A/W} = 157.5\ nW = -38\ dBm$$

Similar to SmartOTDR example, if we have 30dB dynamic range, then the power corresponding to photocurrent will be:

$$P_1 = P_0 + 30dB = -38\ dBm + 30\ dB = -8\ dBm$$

which is equivalent to $0.16\,mW$ of power. Therefore, a photodetector with a responsivity $1\,A/W$ at $-1V$ bias, photocurrent must be $0.16\,mA$ which is an achievable value with waveguide integrated germanium detectors. Actually, several demonstrations have been made of p-i-n photodiodes with saturation currents in the order of a few mAs [83, 132].

To sum up, in order to use in an OTDR application, the most important parameter for a detector is its dynamic range. Therefore, a detector with a high responsivity and sufficiently low dark current is preferred. The bandwidth of the detector is not a difficult to achieve constraint as kHz levels are quite low for p-i-n photodiodes. For the design portion of the study, the target performance metrics for a detector in OTDR application is shown as in Table 5.

Table 5: Design targets for an OTDR detector.

Responsivity	**Bandwidth**	**Dark Current**	**Bias Voltage**
$> 1\,A/W$	$> 10\,KHz$	$< 10\,nA$	$\leq 0V$
@$1550\,nm$ max. responsivity is $1.25\,A/W$	More than Nyquist rate is required and typical OTDR devices operates at $1-5\,KHz$. Bandwidth is not the limiting design criterion even when the detector is operated at 100 MHz sampling rate.	In order to have more than $50\,dB$ dynamic range, less than $10\,nA$ dark current level should be achieved.	In order to minimize the dark current photovoltaic operation mode can be reasonable.

2.3.2 *Telecom Application*

We live in a data-centric society, with technologies like artificial intelligence and 5G causing the amount of data to rise tremendously from 33 Zettabytes (ZB) in 2018 to 175 ZB by 2025 [133]. This significant growth of data is driving need for high-bandwidth and low-latency interconnects [134]. More than 100 Gbps high data rate and kilometers long optical links will be required in order to meet the demands. According to IEEE P802.3bs Ethernet Task Force reports, there are several ways to reach 200-Gbps and 400-Gbps depending on the communication reach as shown in Table 6 [135-137].

Table 6: Ethernet PHY variants for 400G and 200G [137].

Name	Medium	Tx Fibers	Lanes	Reach	Encoding
400GBASE-SR16	MMF	16	16 x 25 Gbps	70-100 m	NRZ
400GBASE-DR4	SMF	4	4 x 100 Gbps	500 m	PAM4
400GBASE-FR8	SMF	1	8 x 50 Gbps (WDM)	2 km	PAM4
400GBASE-LR8	SMF	1	8 x 50 Gbps (WDM)	10 km	PAM4
200GBASE-DR4	SMF	4	4 x 50 Gbps	500 m	PAM4
200GBASE-FR4	SMF	1	4 x 50 Gbps (WDM)	2 km	PAM4
200GBASE-LR4	SMF	1	4 x 50 Gbps (WDM)	10 km	PAM4

In old Ethernet standards, 2-level Non-Return-to-Zero (NRZ) method for encoding binary data stream is used. However, to obtain higher data rate per lane, the encoding method is changed to PAM4, which effectively doubles the data rate. PAM4-modulated signal has 4-levels as shown in Figure 38, therefore, instead of sending 1-bit of data with NRZ, 2-bits of data can be sent using PAM4 signaling.

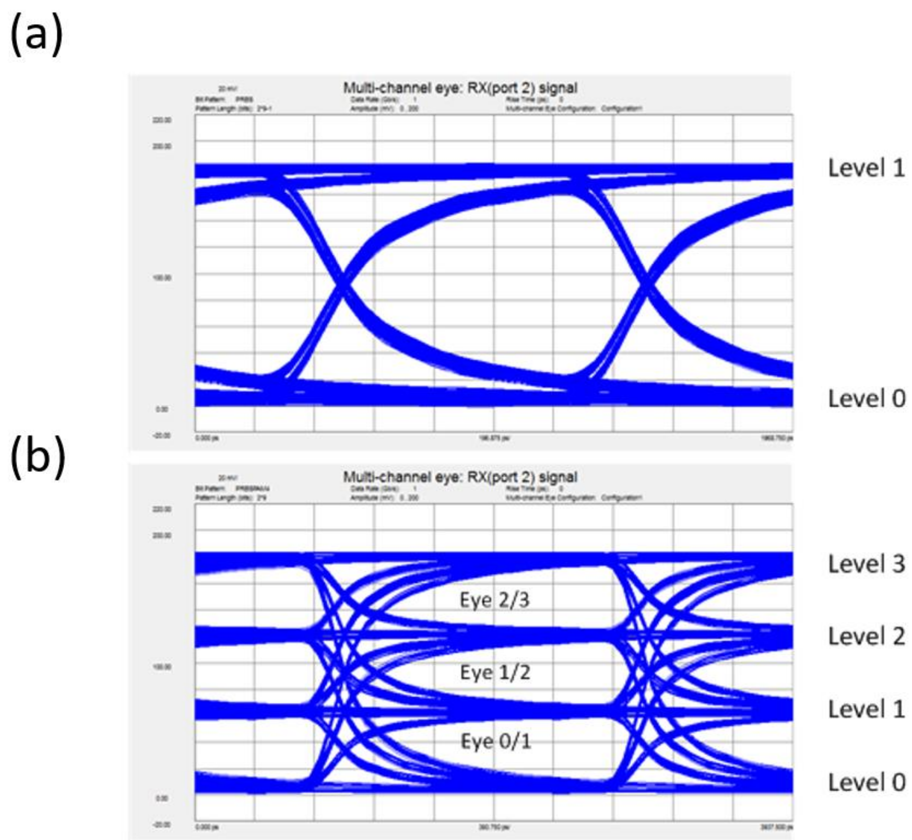

Figure 38: (a) NRZ vs (b) PAM4 encoding [138].

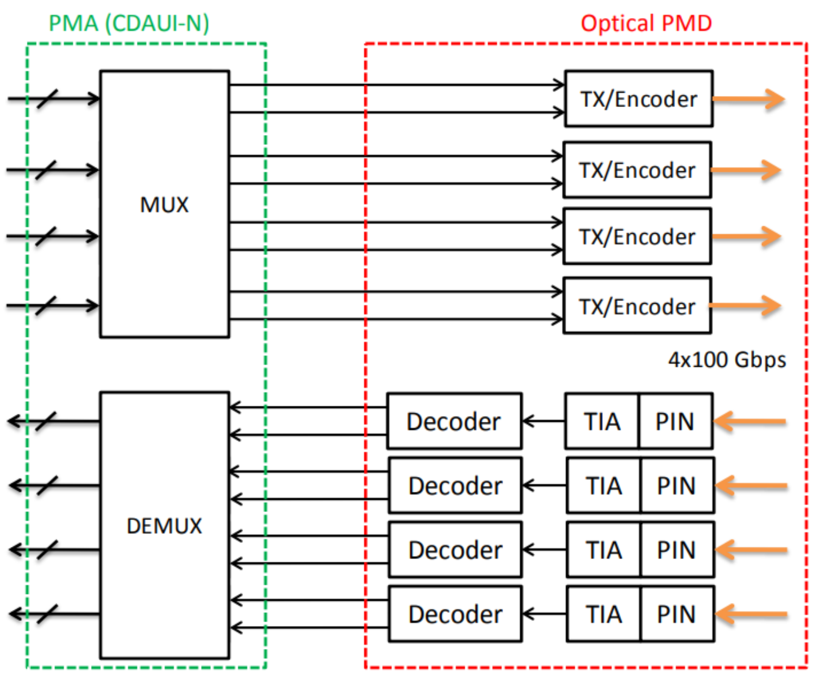

Figure 39: Block diagram of 400GBASE-DR4 [139].

Considering the future communication needs, we can examine the photodetector requirements for the 400GBASE-DR4 system as it has the highest data rate per lane. Figure 39 shows the block diagram of 400GBASE-DR4 system [139]. The receiver characteristics given in Table 7 is obtained from a commercial example, which is 400G-QSFP-DD-500 module from Edge Optical Solutions [140].

Table 7: 400GBASE-DR4 Receiver Characteristics [140].

Specification	**Value**
Rx Wavelength Bandwidth	1304.5-1317.5 nm
Avg. Receiver Sensitivity (Min)	-5.9 dBm
Avg. Receiver Sensitivity (Max)	4 dBm
Min Receiver Sensitivity [139]	-9.25 dBm
Data Rate Per Lane	53.125 GBd
Operating BER	2×10^{-4}
Modulation	PAM4

In contrast to photodetector requirements for OTDR application, 400GBASE-DR4 specifications require minimum responsivity of 0.6 A/W at 1310 nm and 35 GHz bandwidth at 2V reverse bias for the photodetector [134]. Moreover, the shot noise due to dark current should be comparably low to the input referred noise of the TIA which is $15\ pA/\sqrt{Hz}$ [141]. For 40 GHz of operating bandwidth, input referred TIA noise will be around 3µA. Therefore, choosing the upper bound of photodetector's dark current to be 100 nA does not harm the noise profile of the receiver circuit.

Table 8: Design targets for telecom photodetector.

Responsivity	**Bandwidth**	**Dark Current**	**Bias Voltage**
$> 0.6\ A/W$	$> 35\ GHz$	$< 100\ nA$	$\geq -2V$

Chapter 3:
VERTICAL PIN PHOTODETECTOR DESIGN

In this chapter, our waveguide integrated Ge-on-Si vertical p-i-n photodetector design procedures using Lumerical tools will be presented. A photodetector with 10μm long, 4μm wide and 1μm thick active area will be designed as a base device. First, we will examine the performance metrics of the detector in this geometry in terms of dark current, responsivity and bandwidth. Second, geometrical manipulations on the device length, width and thickness will be made and the effects on the performance metrics will be discussed.

For the first part of the chapter, the photodetector design procedure will be as follows:

1. Setting up the simulation geometry in Lumerical DEVICE
2. Simulating dark current in Lumerical DEVICE
3. Simulating 3D optical absorption and finding the optical generation rate in Lumerical FDTD
4. Simulating responsivity in Lumerical DEVICE after importing the optical generation rate obtained in FDTD simulation
5. Doing a transient simulation in Lumerical DEVICE and estimating the bandwidth of the detector

3.1 Device Setup

In this section of the design, we will create the photodetector geometry in a 3D model with specific electrical and optical material characteristics. In the simulations, we will be using material database of Lumerical. For a germanium vertical p-i-n detector simulation, it is required to add silicon (Si), silicon-dioxide (SiO_2), germanium (Ge) and aluminum (Al) materials. Silicon and silicon-dioxide are used for creating waveguide and cladding whereas germanium is used for the active region of the photodetector. Aluminum is chosen for metal contacts as it is widely used as a metallization material in the IC industry due to its advantages like ease of deposition, low resistivity and ohmic contact to silicon [142]. After adding the materials, using script files for the device setup is useful for parametrizing the device geometry, for parameter sweeps and for analyzing the device behavior change with respect to different geometries.

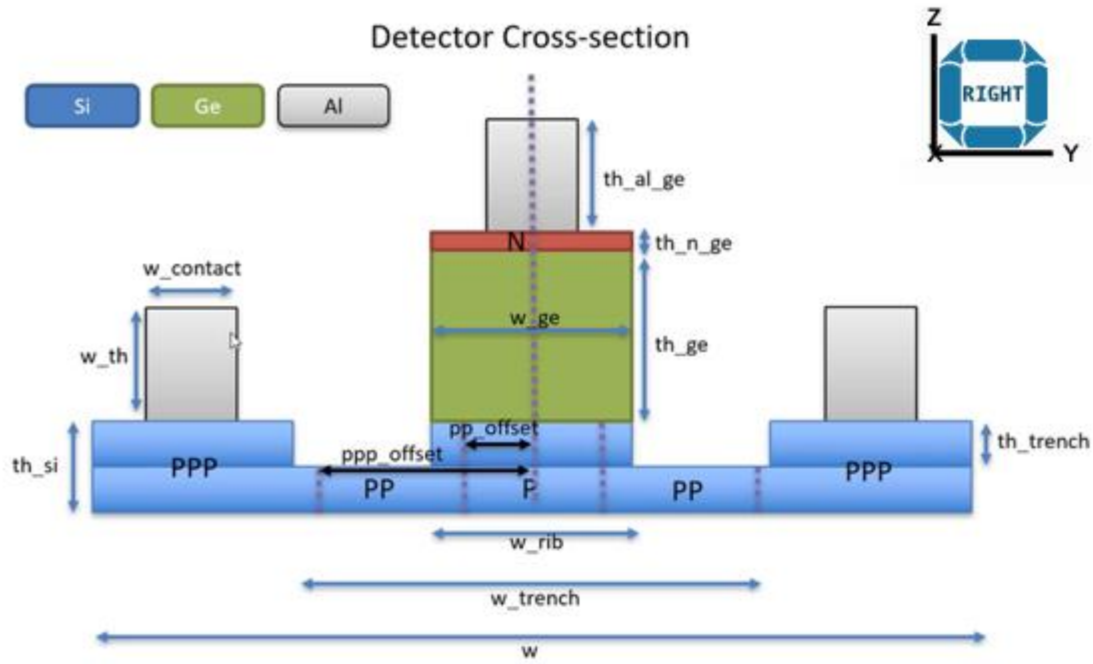

Figure 40: Geometric detector parameters used in device setup scripts.

Figure 40 shows some of the different parameters in describing our photodetector device setup. Among these parameters, especially Ge thickness, Ge width and Ge length are important as they constitute the active region of the detector. Table 9 shows the detailed description and value of each dimension shown in Figure 40.

In addition to detector parameters, we have also included the 2D simulation region in the script. The simulation is in 2D (yz cross-section) because the detector does not vary along the x-axis, which is the direction of the light. This makes the simulation run much faster. Some of the important things about the simulation region is that the simulation region should cover the entire detector area and the CHARGE solver norm length should be equal to detector length in order to have accurate results. The norm length is actually the missing third dimension as we do the simulation in 2D.

Inside the CHARGE solver, we are adding the electrical boundary conditions for our contacts. In order to have a reverse-bias on the photodetector, the anode voltage is set to -1V, whereas the cathode voltage is held at ground or 0V. We also have surface recombination boundary conditions for the interfaces between the material used.

Finally, we add the doping regions and the charge monitor. We have n-type doping region for the top of the germanium and p-type doping regions in the silicon. All the doping concentrations and doping regions are parametrized in the scripts and can be changed to see the doping effects on the device behavior. The important device setup parameters are shown in Table 9.

Table 9: Device parameters used in the models and parametric studies.

Parameter	Definition	Value
l	Photodetector length (along x axis)	10μm
w	Total width of the device	7.6μm
w_rib	Width of Si rib waveguide	4μm
w_trench	Width of trench	5.5μm
pp_offset	pp doping starting point from center	0
ppp_offset	ppp doping starting point from center	500nm
w_ge	Germanium width	4μm
w_n	N doped Ge region width	4μm
l_in	Input waveguide length [Figure 27(a)]	1μm
th_si	Thickness of the silicon	220nm
th_trench	Trench thickness	110nm
th_ge	Germanium thickness	1μm
th_al_ge	Germanium contact thickness	500nm
th_n_ge	Germanium doping depth	50nm
w_contact	Width of contact	500nm
th_contact	Thickness of contact	500nm
contact_offset	Contact offset from detector edge	100nm
n	n doping concentration	$10^{18} cm^{-3}$
nn	nn doping concentration	$10^{19} cm^{-3}$
nnn	nnn doping concentration	$10^{20} cm^{-3}$
p	p doping concentration	$10^{18} cm^{-3}$
pp	pp doping concentration	$10^{19} cm^{-3}$
ppp	ppp doping concentration	$10^{20} cm^{-3}$

After setting up the parameters and creating the device model, the resulting photodetector would be similar to the geometry shown in Figure 41. The light blue box covering the detector is silica (SiO_2) which surrounds the device in every direction to eliminate electrical discontinuities in the simulation.

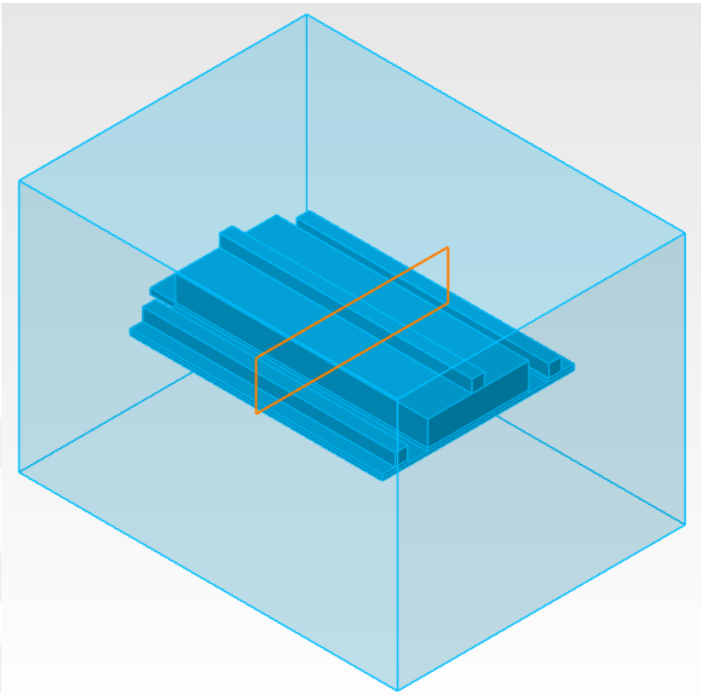

Figure 41: Example device model.

3.2 Dark Current

In this section, we use our photodetector device model in DEVICE simulation and analyze its I-V relation without illumination.

In order to better visualize the I-V relation of the photodiode, changing the boundary condition of the anodes from single voltage value to sweep of voltage ranges is required.

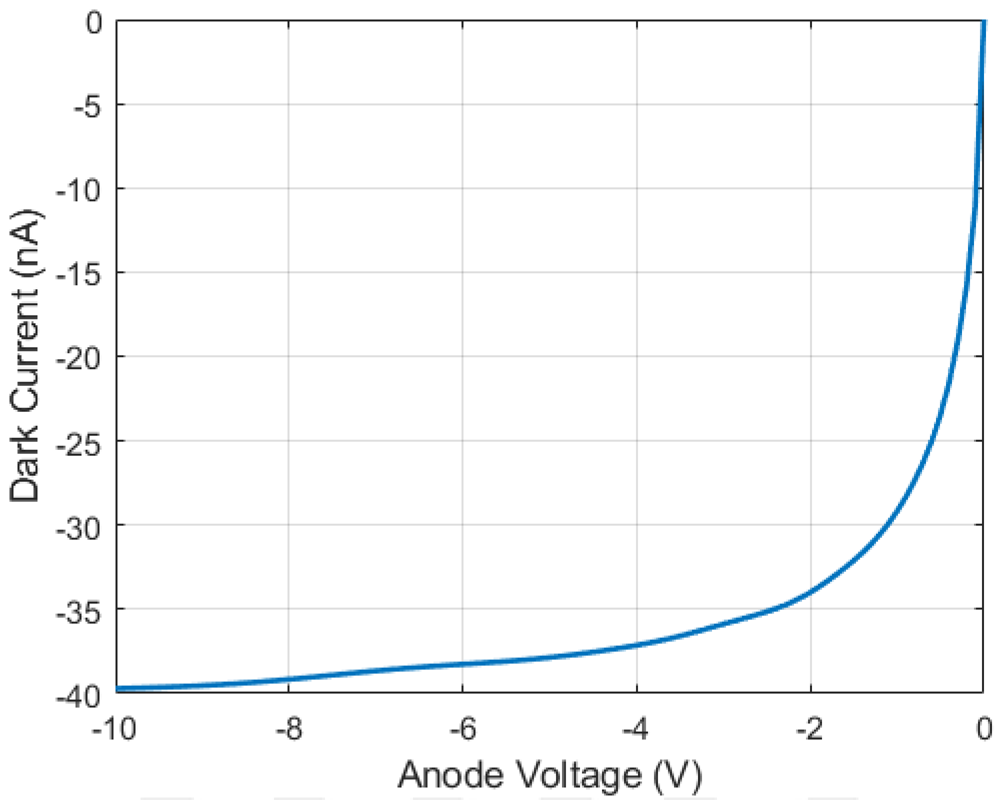

Figure 42: Dark current at different anode voltage levels.

It can be seen in Figure 42 that at 1V reverse bias, the photodetector dark current is around 29 nA. Moreover, as the reverse bias voltage increases, the dark current also increases. At -2V bias, the dark current is increased to 34 nA. If the voltage level is further increased to -10V, the dark current saturates around 40 nA. Also, it is important to mention that at 0V when there is no bias voltage, there is no dark current as the material is in equilibrium.

3.3 Optical Generation Rate

In this section, we do an optical absorption simulation in FDTD and see how the photodetector absorbs light and generates photocarriers. In contrast to DEVICE simulations, we will make a 3D simulation to understand the behavior of incident light rather than 2D. Since 3D simulation takes much longer time, one of the things can be done to mitigate this is disabling metal regions of the detector. Even though the light absorbing effect of the metal regions are excluded in this case, this change significantly shortens the simulation time from 55 hours to less than 2 hours. Finally, since we have used the scripts to define the device geometry in DEVICE simulation, we can immediately define the same device in FDTD again by using the scripts.

Unlike in DEVICE simulation, in FDTD simulations we need to shine light into our photodetector. Thus, we are adding an optical mode source as shown in Figure 43 as a purple arrow.

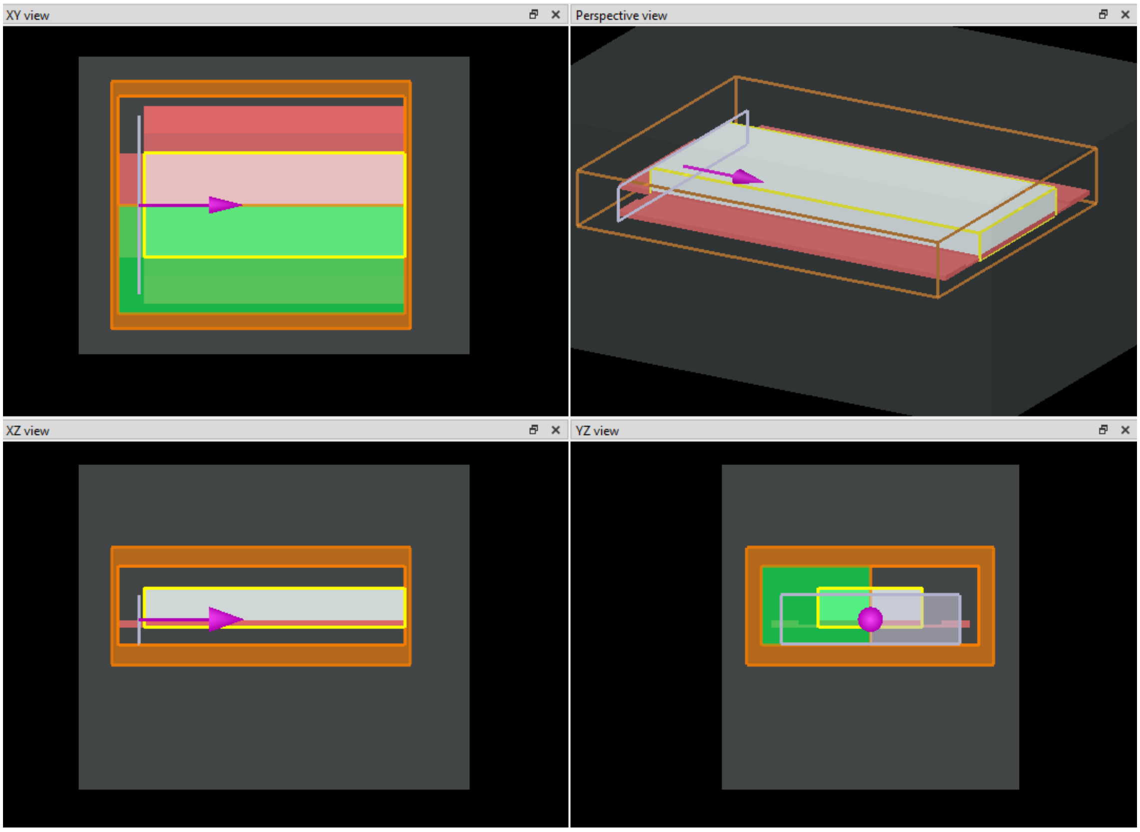

Figure 43: FDTD Device Setup.

The injection axis of the light is in the x-axis, and we input the fundamental mode of the input silicon waveguide. Mesh accuracy parameter is set to 3, which was 2 by default, to get a more accurate result from the simulation. The optical input mode is visualized as in Figure 44Figure 44.

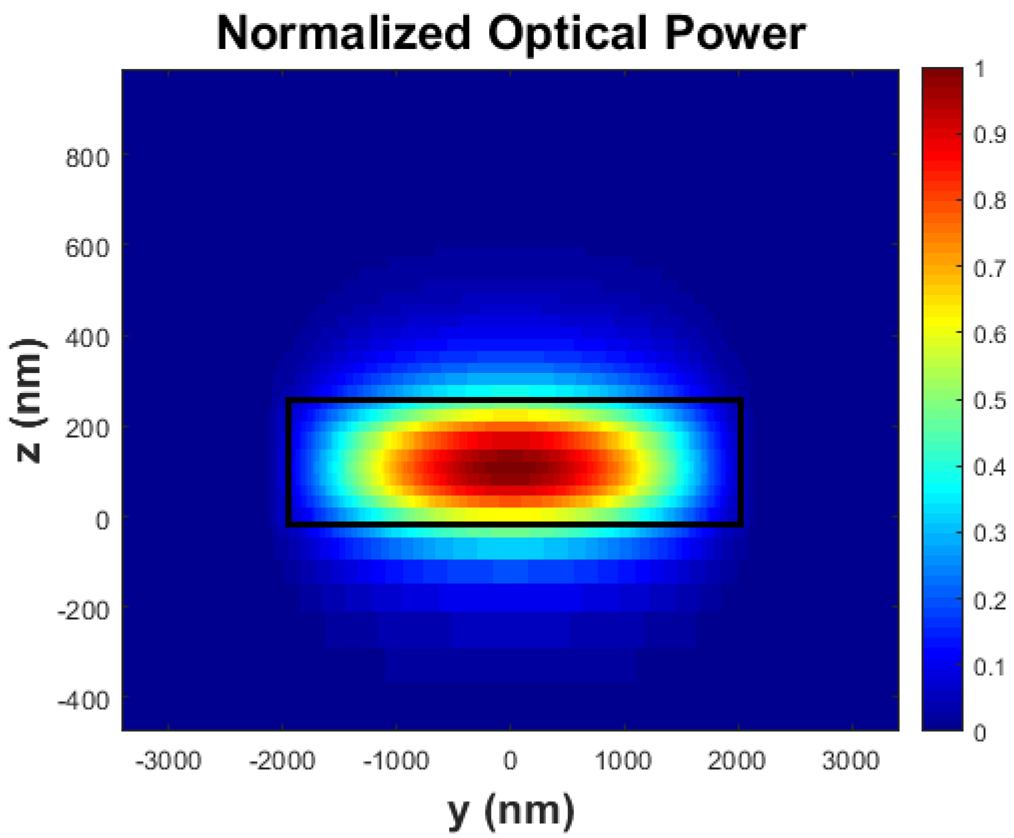

Figure 44: Optical input mode in silicon waveguide. Solid rectangle shows the edges of the input waveguide.

The actual data we need to get out of this simulation is the photocarrier generation rate. The power absorbed by the photodetector can be expressed as in equation (9.1) where ε is the permittivity.

$$P_{absorbed} = -0.5\nu|E|^2 imag(\varepsilon) \tag{7.1}$$

The refractive index of a medium is given as:

$$n = \left(\frac{\varepsilon}{\varepsilon_0}\right)^{\frac{1}{2}} \tag{7.2}$$

If we consider unity internal quantum efficiency (for each absorbed photon, one photocarrier pair is generated), then we can simply write the generation rate as the ratio of absorbed photons per unit volume per second.

$$G = \frac{P_{absorbed}}{h\nu} \tag{7.3}$$

Hence, if we calculate $E\ and\ n$ using FDTD simulations, we can also find the generation rate. In order to do that, we use CW generation analysis group in FDTD, which is comprised of a field monitor and an index monitor.

Besides the optical generation rate, FDTD simulation visualizes a lot of electro-optical characteristic about the photodetector. For example, in Figure 45 it can be seen how light is coupled from silicon waveguide to germanium region. Light enters from the left in our silicon region, which is at the bottom, and it leaks into higher index germanium. As it continues to bounce around and propagate in a multi-mode nature, it is getting weaker and weaker as light gets absorbed.

Figure 46 depicts the average of generation rates along the x-axis. As our device is symmetric around the x-axis, for the electrical simulations in DEVICE, it is better to average the generation rates along the x-axis. Figure 46 also shows that in our silicon region at the bottom, no light is being absorbed, but in our germanium layer in the upper side of the graph, we see strong electric field due to carrier generation.

Finally, we can look at the total absorbed power as a result of the FDTD simulation and it is 36.7 percent of the input power which is fairly low. We will show several approaches to increase the total absorbed power by refining the detector geometry.

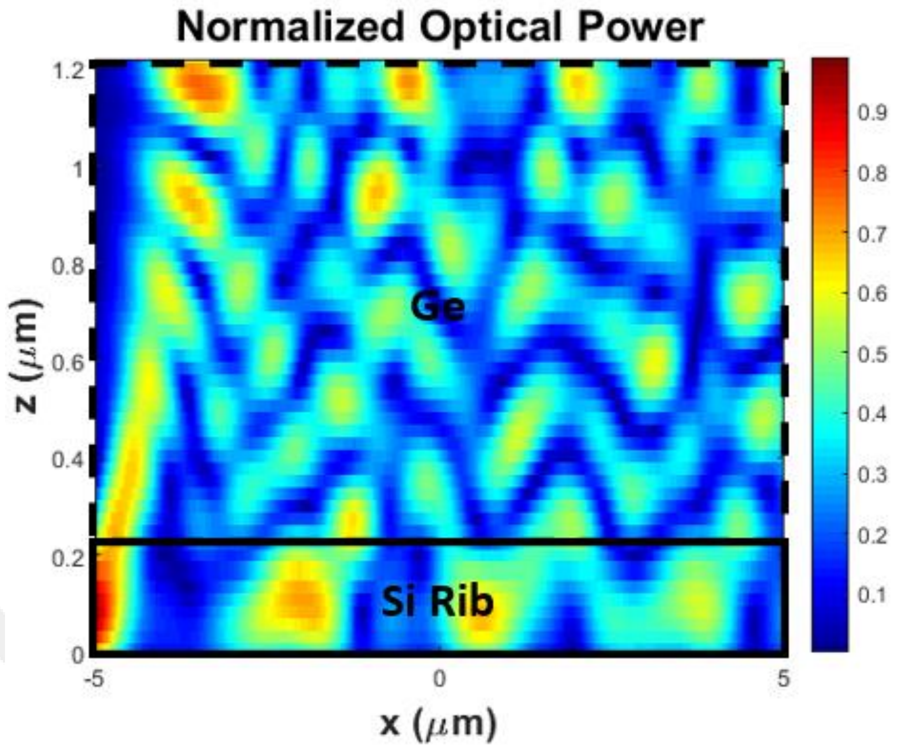

Figure 45: Light intensity change along the detector length. Dashed rectangle shows the Ge region whereas solid rectangle shows the Si rib waveguide.

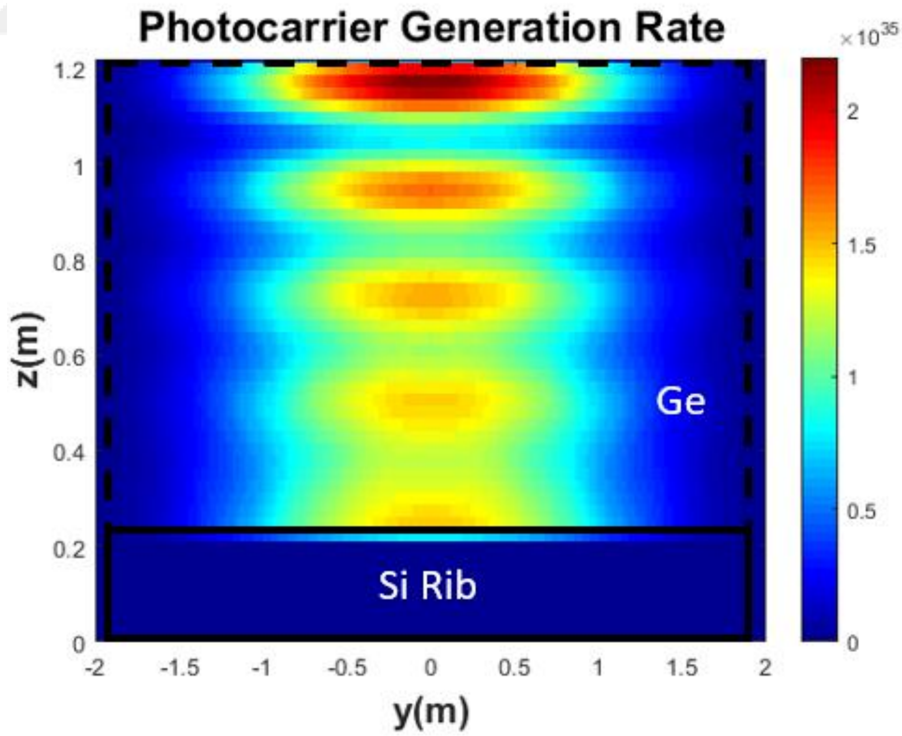

Figure 46: Generation rates averaged along the x-axis. Figure shows the y-z cross-section of the detector. Dashed rectangle shows the Ge region whereas solid rectangle shows the Si rib waveguide.

3.4 Responsivity

In this section, we are going to import the generation rate that we have found in FDTD optical simulation into DEVICE simulation to simulate the responsivity of the photodetector.

Responsivity, or photocurrent output per incident optical power, is determined by the internal quantum efficiency as well as extrinsic properties such as geometry. Thus, responsivity includes information about both electrical and optical characteristics of our photodetector. Photons must be absorbed to produce photocarriers and every photocarrier might not make it to the electrical contacts.

After importing the average optical generation rate along the x-axis, we are ready to model the responsivity of the detector. Similar to dark current model, we will look for the I-V characteristic of the detector by varying the bias voltage, but this time we are going to measure the photocurrent under illumination.

From the simulation results, as shown in Figure 47, the responsivity of the Photodetector at 1V reverse-bias is approximately 0.444 A/W. It is expected to be low as the absorption feature was also low as we have measured in FDTD simulation.

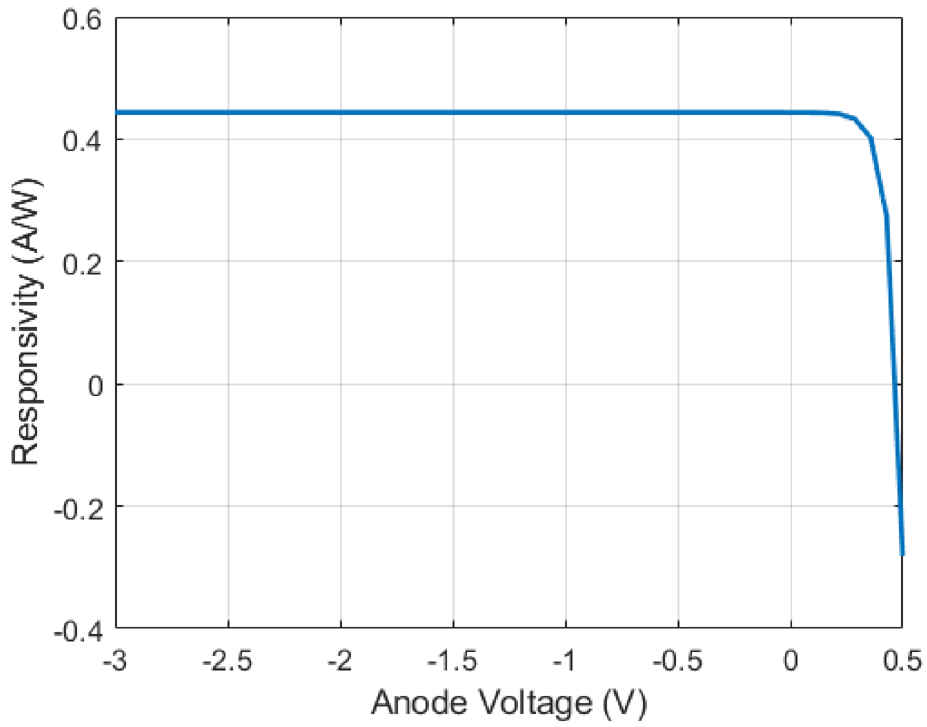

Figure 47: Responsivity of the photodetector.

Figure 47, when we reverse bias the photodetector ($V < 0$), the responsivity does not change significantly and saturates around 0.45 A/W. However, if we zoom in the graph as in Figure 48, as the reverse bias voltage increases, the photocurrent and the responsivity also increase. Since, this base detector design has low responsivity due to its geometry, the effect of reverse bias voltage on responsivity is also quite low.

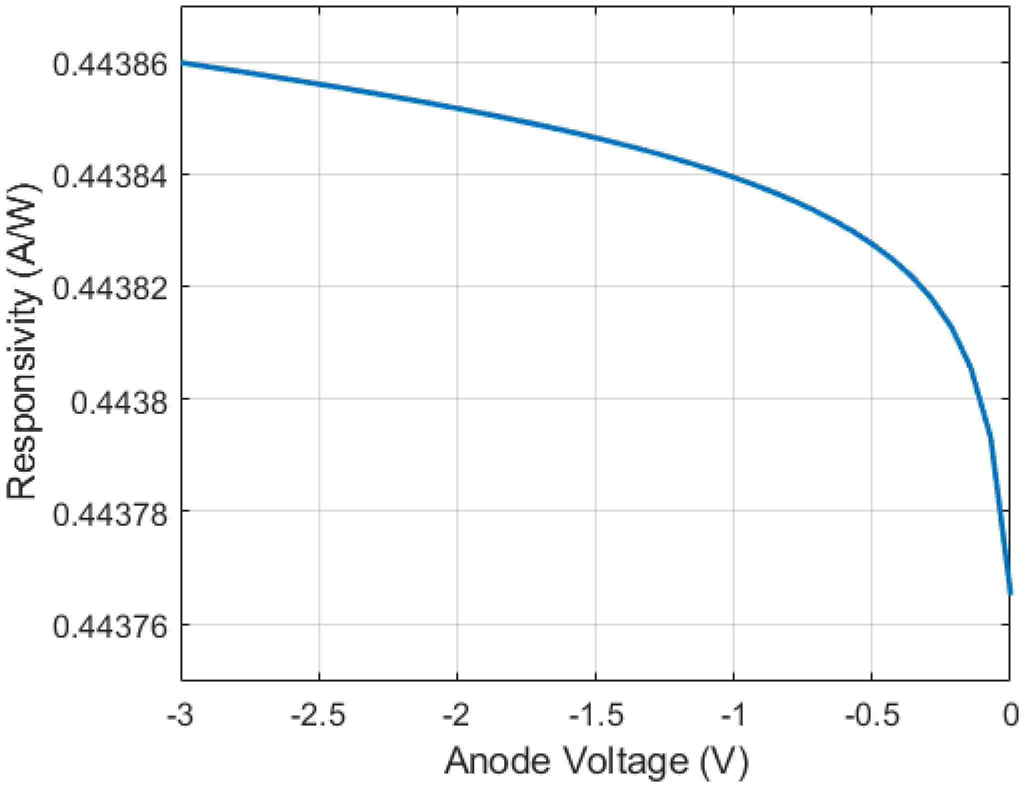

Figure 48: Responsivity graph for the detector between 0-3V reverse bias.

3.5 *Bandwidth*

In this section, we estimate the transit time dependent bandwidth of the photodetector by using two different methods: transient analysis and small-signal AC analysis. Then, we calculate the DC capacitance and resistance from the model and estimate the RC-limited bandwidth of the detector. Finally, by using the equation (3.7), we estimate the total bandwidth of the photodetector.

First, we do a transient simulation. This means, we analyze the detector response when a very short pulse of light is injected. If we Fourier transform this impulse response, we will get the frequency response of the photodetector and be able to estimate quantities such as 3dB bandwidth.

The approach to do this simulation in DEVICE is by using an optical shutter. The optical shutter is going to quickly turn on the optical generation rate instead of putting a pulse of light incident on the detector. This is going to produce a step function input where the light is going to be off, then in a very short amount of time it will be on and keep staying on. The time derivative of the step response will give us the impulse response.

The cartoon in Figure 49 shows the steps in transient simulation. The red curve represents the step input or the optical shutter. It is only a scaling value that will be multiplied by the optical generation rate. For the first picoseconds of the simulation, the optical shutter will be off, and no light will enter the system. Between one picosecond and two picoseconds, the shutter will open up. The period of time for opening up is called the slew.

A small-signal AC analysis (ssac) can also be used as an alternative to transient analysis when measuring the transit time dependent bandwidth of the photodetector. In this method, a small-signal perturbation is introduced to the DC optical generation rate, and the detector's small-signal response (photocurrent) is measured as a function of the small-signal frequency.

In contrast to transient simulation, ssac simulation usually takes shorter amount of time, because while in transient simulations one non-linear equation needs to be solved for each time step, ssac simulation only needs a steady state solution for each bias. Moreover, since the transient simulations are more complex in numerical terms, they usually suffer from convergence issues.

As shown in Figure 50, both simulations yield similar results for the transit bandwidth of the detector which is around 25.12 GHz 3dB bandwidth. Therefore, for the rest of the bandwidth simulations, we will prefer doing ssac simulations to calculate the transit bandwidth.

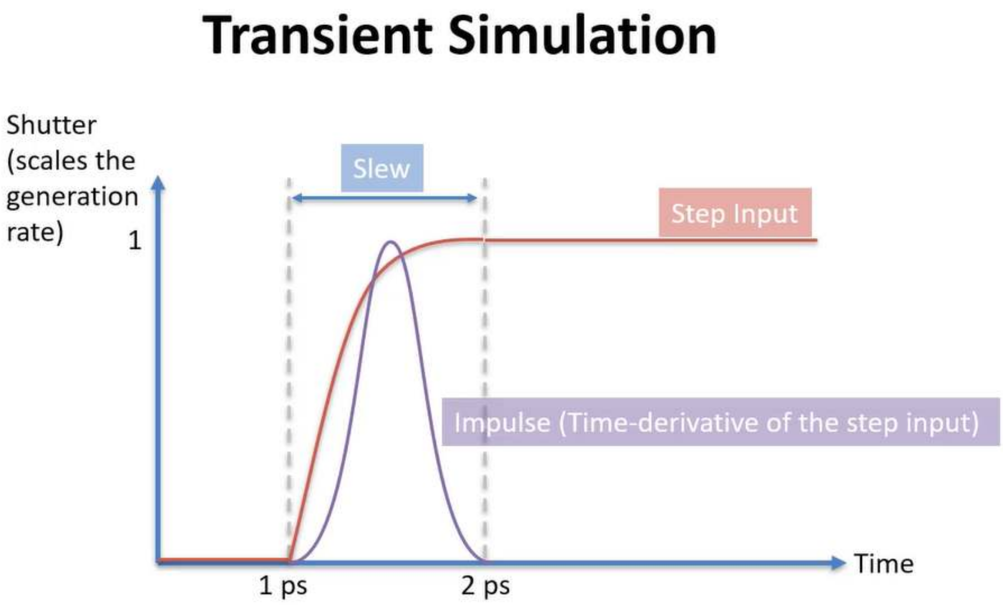

Figure 49: Transient simulation steps [97].

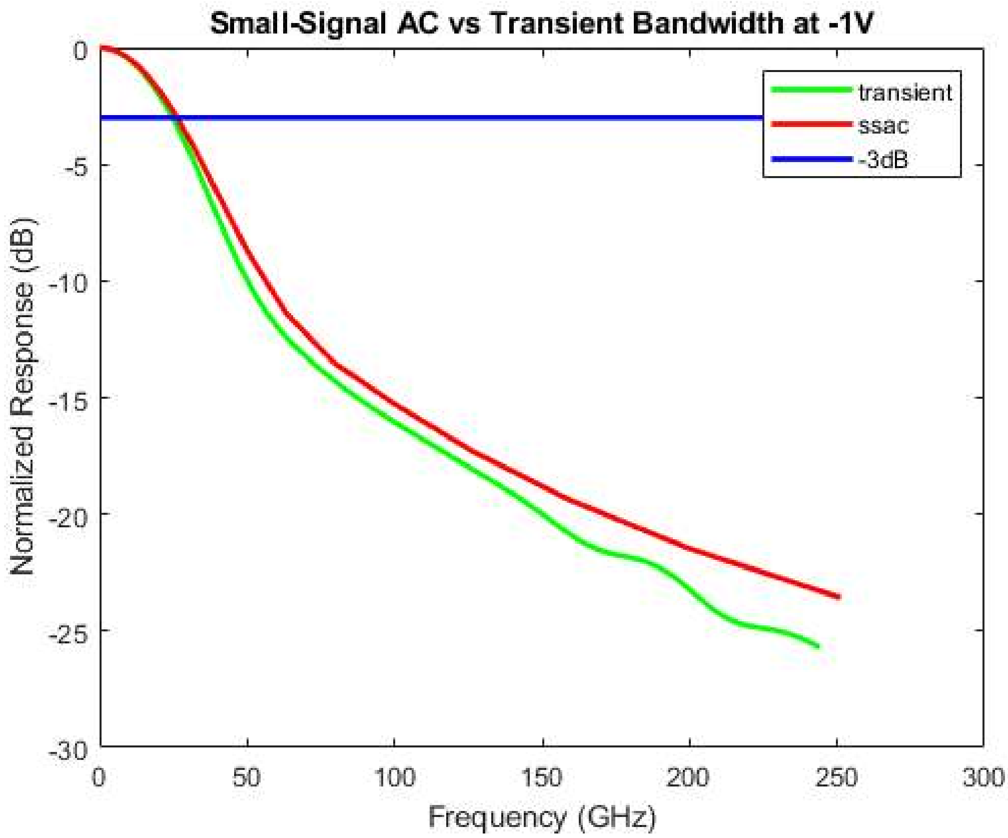

Figure 50: Small-signal AC vs Transient analysis.

These simulation results are also consistent with the estimation of transit bandwidth given by the equation (3.5), which estimates the transit bandwidth as 26.4 GHz.

To calculate the DC capacitance of photodetector, we use a script. This script simply utilizes the definition of capacitance, which is the change in charge with a small change in voltage. We put a monitor that integrates the amount of charge in the junction and then we change the voltage slightly, so that we can calculate the actual capacitance. We repeat the same procedure for a range of voltage biases, because as we deplete the junction, the capacitance should be changing significantly.

Figure 51 depicts the DC capacitance of the detector per unit length. In the simulation, two charge monitors used to compare the overall device capacitance with the junction capacitance. In the equivalent circuit model, the junction capacitance is the dominant term. For -1V bias, the capacitance of the detector is 6.8fF.

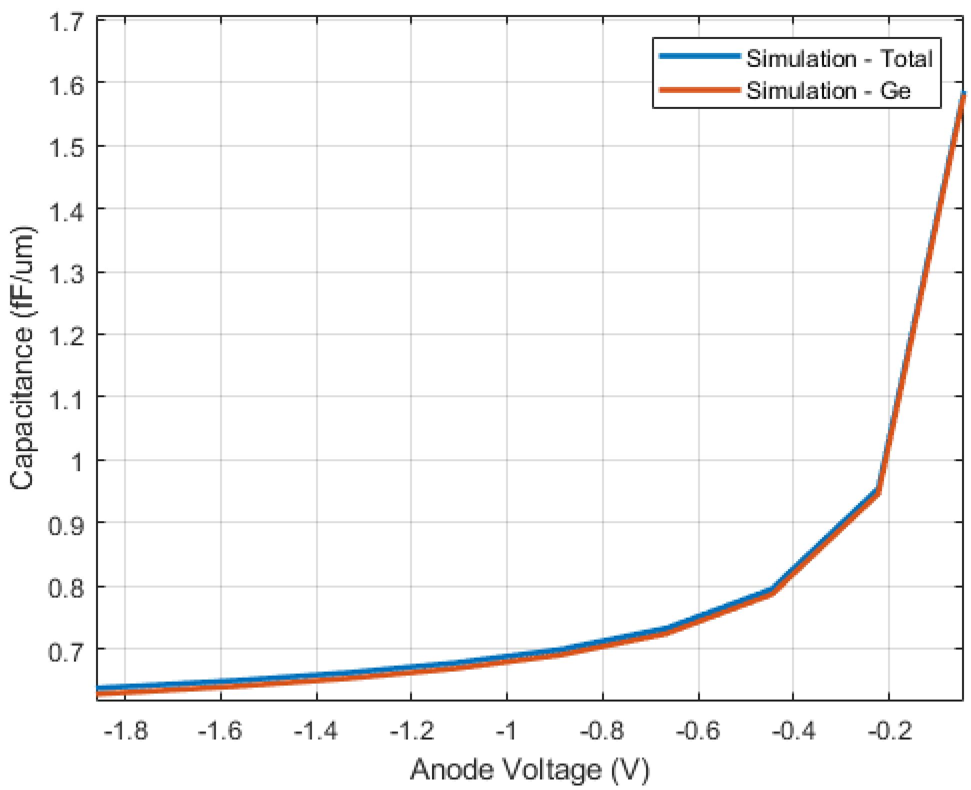

Figure 51: DC Capacitance of the photodetector per unit length.

There are two resistance values to be calculated as shown in the equivalent circuit model in Figure 31. For the resistance measurements on the model, we use virtual ground points and the closest contact metal as the voltage probing points as shown in Figure 52. Then, we will apply a small voltage, i.e., 0.1V, and then by measuring the amount of current flowing between the probes, we simply measure the resistance by R = 0.1/I. The two resistances have the same value as they are equal due to same doping concentrations. Therefore, by measuring one of them is sufficient and it results 35.92Ω. Thus, the overall equivalent resistance is $(R_{S1} \,||\, R_{S2}) = 35.92\Omega\ /\ 2 = 17.96\Omega$. The RC bandwidth, after including a 50Ω R_{Load} resistor, is 344 GHz. However, since the device bandwidth is transit time limited, the overall 3dB bandwidth is 25.1 GHz.

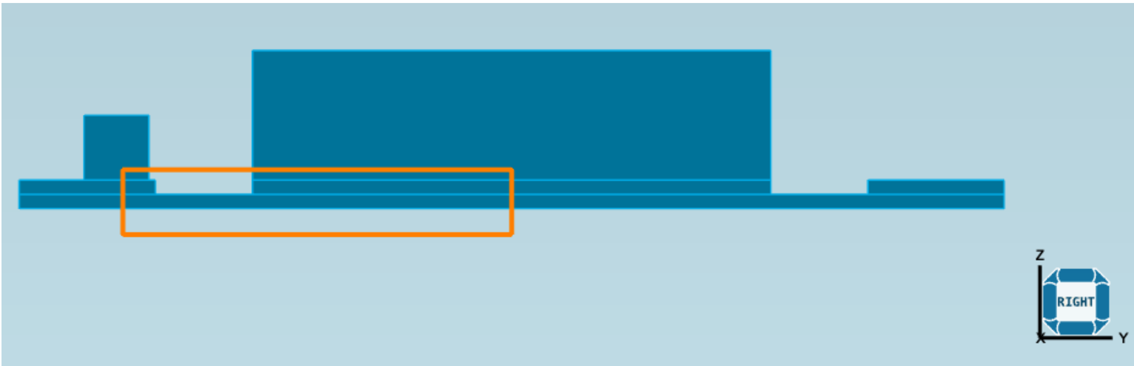

Figure 52: Measuring the resistance of photodetector. The orange rectangle shows the simulation region where the virtual ground is located at the right-most edge of the rectangle.

3.6 Compact Model

In this section, we take the results from photodetector performance simulations in FDTD and DEVICE and import them to INTERCONNECT to realize a compact model for the photodetector. The performance metrics that we have found during the simulations for our base photodetector design is shown as a summary in Table 10.

Table 10: Summary of performance metrics of the base photodetector design.

Responsivity	**Bandwidth**	**Dark Current**	**Bias Voltage**
0.444 A/W	25.1 GHz	29 nA	-1 V

The two blocks inside the dashed red square in Figure 53 represent our photodetector. Photodetector performance metrics are imported in these blocks. For the bandwidth characteristics of photodetector, a low-pass filter is used, and the cut-off frequency of the filter is set as 25.1 GHz 3dB bandwidth of the photodetector. The thermal noise and shot noise properties of the photodetector are also enabled. The other blocks used in the model are required to show photodetector performance by an eye diagram. There are 1mW power continuous-wave laser operating at 1550 nm, an amplitude modulator, pseudo random bit sequence generator and non-return to zero pulse generator that used for random signal generation at 10 Gb/s rate. The electrical output of the detector is connected to eye diagram to show its performance in a standard metric.

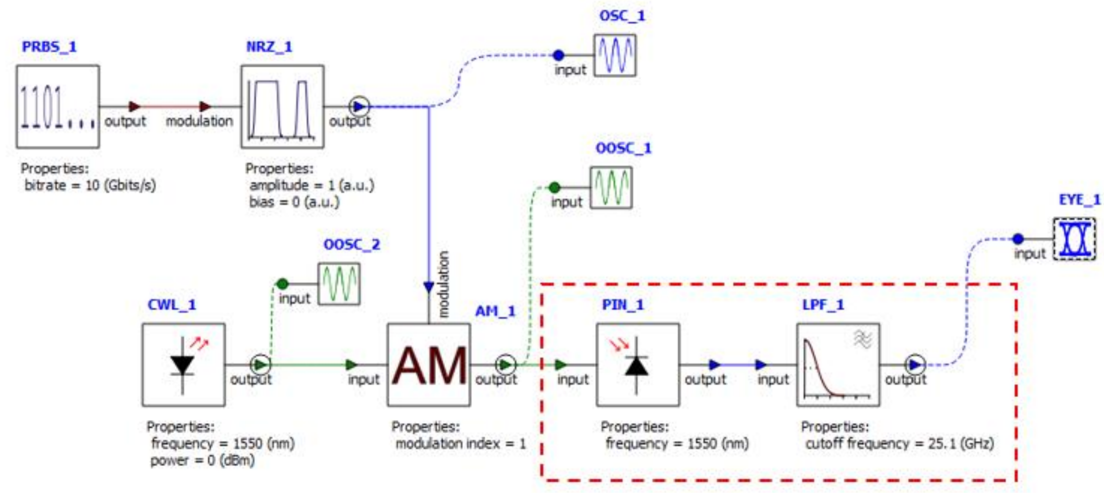

Figure 53: Photodetector compact model in INTERCONNECT software. CWL_1 shows the CW laser, PRBS_1 shows the random bit sequence at 10 Gbps, NRZ_1 shows the digital pulse profile used for driving the ideal modulator (AM_1). Green and blue lines indicate electrical and optical connections, respectively. PIN_1 is our photodetector device under test. LPF_1 is a low pass filter that is required to simulate the bandwidth of our photodetector.

Eye diagrams shown in Figure 54-56 are the time-dependent photocurrent outputs from our photodetector which is subject to a random digital bit stream generated by on/off keying. These plots quantify the rise and fall times of the photodetector. The opening between high and low signals indicates the signal-to-noise ratio for the given bit rate. Eye diagrams are commonly used for quantifying the bandwidth of photodiodes.

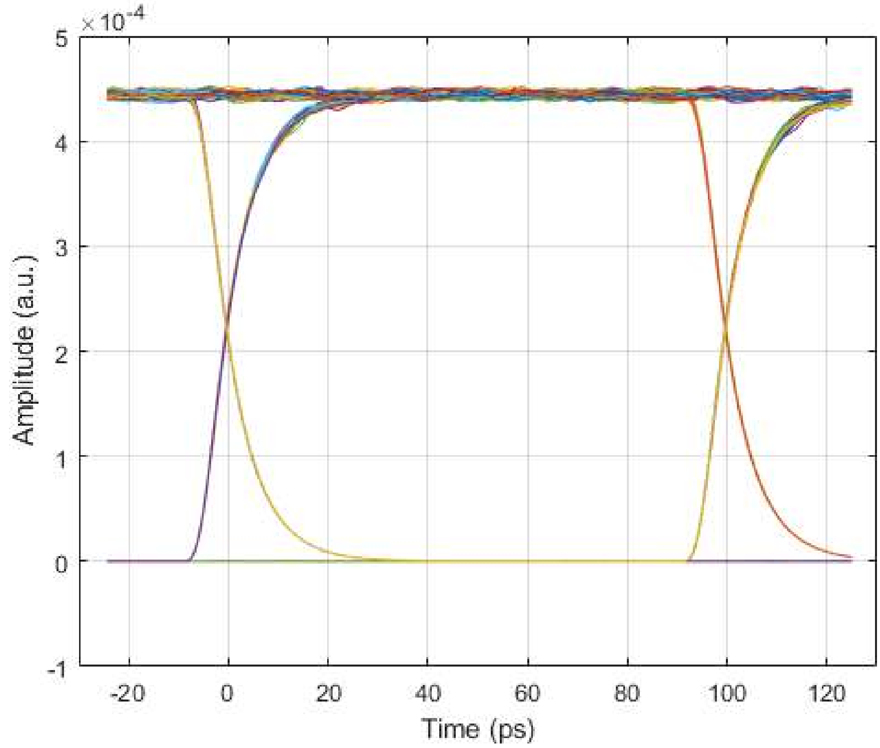

Figure 54: The eye diagram of the base photodetector design at 10 Gbps.

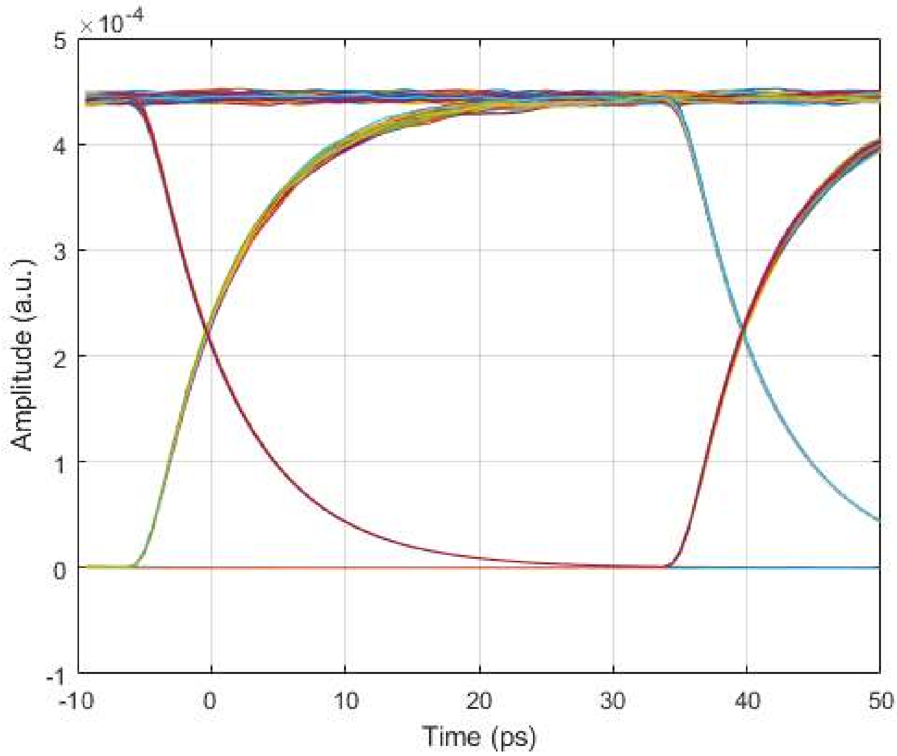

Figure 55: The eye diagram of the base photodetector design at 25 Gbps.

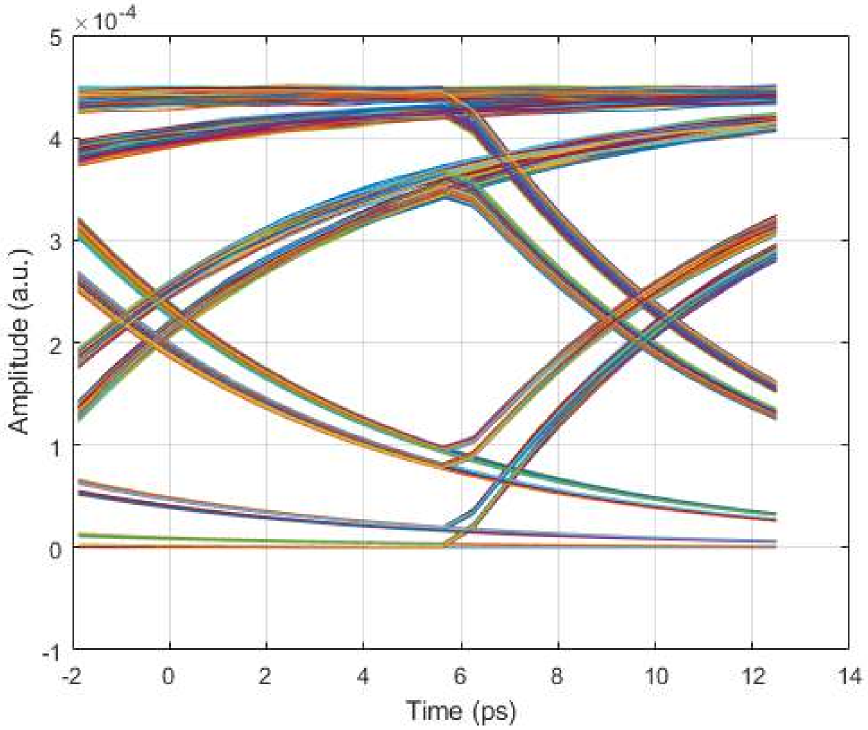

Figure 56:The eye diagram of the base photodetector design at 100 Gbps.

As the bit rate increases, the “eyes” in the diagrams get closed. This metric shows the performance of the detector in different applications with different bit rate requirements.

3.7 *Effect of Different Geometries on Photodetector Characteristics*

3.7.1 *Photodetector Length Sweep*

The base design for the photodetector can be enhanced by changing the length, width, and thickness of the active region of the device. For the design optimization, we start by increasing the total absorbed power, as the fundamental functionality of a photodetector is how efficiently it converts light into current. In the detector geometry section 2.1.3, increasing the length of the active region of the detector has been shown to increase the total absorbed power and therefore the responsivity.

In this section, we sweep the length of our base photodetector design having 1µm Ge thickness and 4µm width. Figure 57 shows the simulation results for responsivity values of photodetectors ranging from 10µm to 100µm long. It is already shown that at 1550 nm wavelength, given an internal quantum efficiency of 1, the maximum responsivity value can be 1.25 A/W at most. Figure 57 shows that designing photodetectors longer than 40μm absorbs most of the light and has responsivity values higher than 1 A/W.

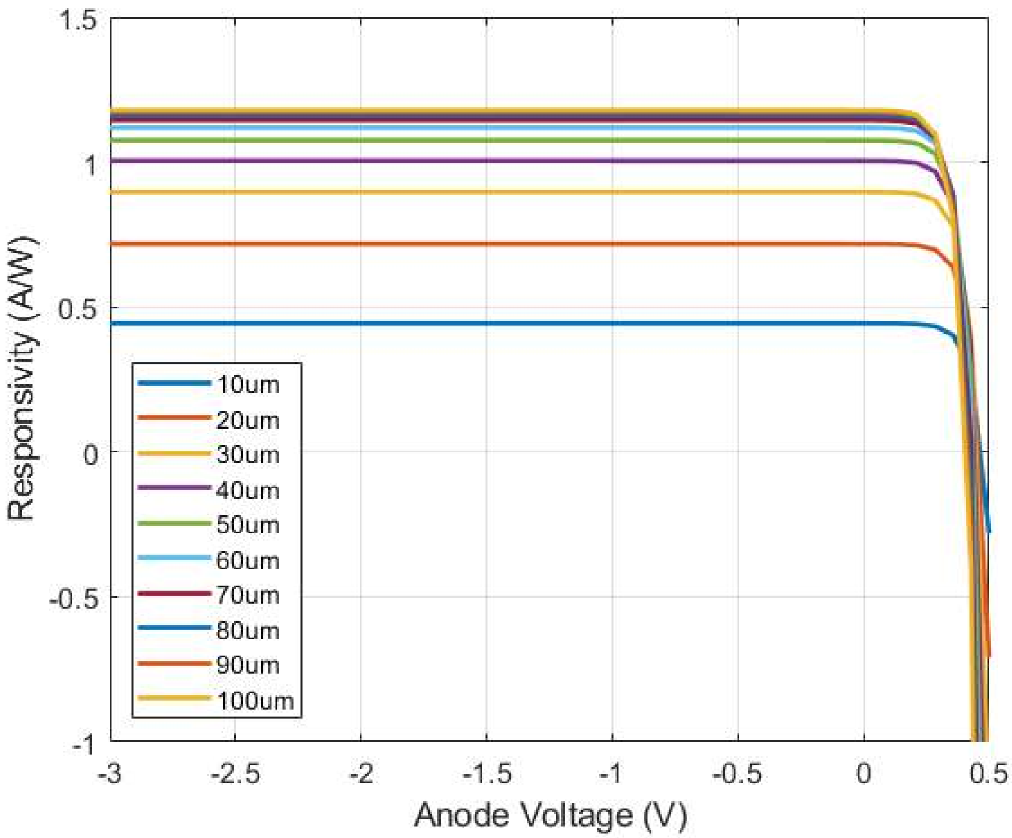

Figure 57: Responsivity for different lengths ($10 - 100\ \mu m$ with $10\ \mu m$ increments).

However, increasing the length of the detector has some drawbacks. The first disadvantage is that the dark current increases proportionally with the length as shown in Figure 58. It rises from 29nA to 290nA as the length is increased from 10μm to 100μm at 1V reverse bias. The second disadvantage of increasing the length is that the RC-limited bandwidth decreases due to increased capacitance with length.

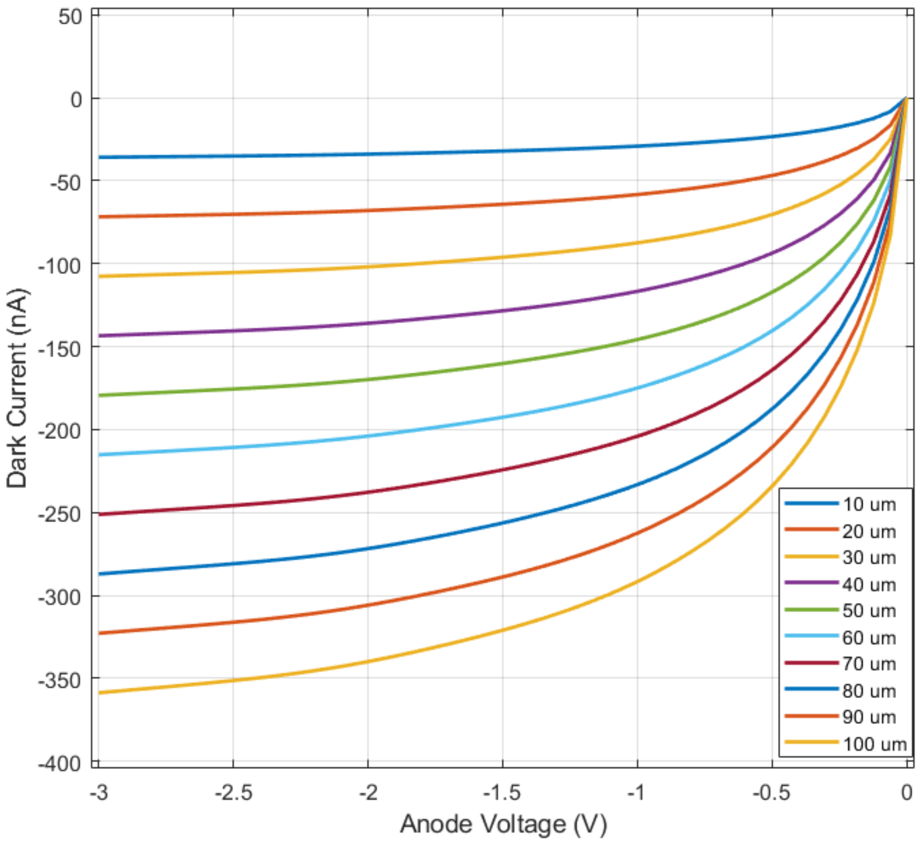

Figure 58: Dark Current values for different lengths ($10 - 100$ μm with 10 μm increments).

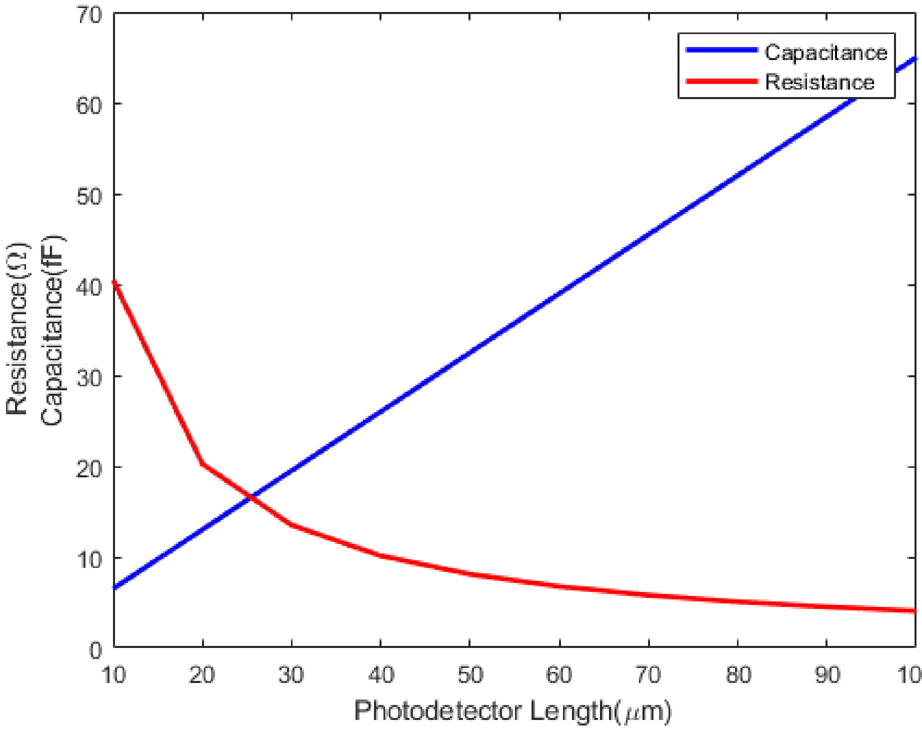

Figure 59: Detector RC characteristics with respect to the length.

Figure 59 shows that as length increases, while capacitance increases proportionally, the total series resistance decreases. The overall RC delay may not be affected significantly as one term increases and the other decreases. However, if we add the load resistance, R_{Load}, which is usually 50Ω for impedance matching, the RC-limited bandwidth decreases with photodetector length as in Figure 60. Since, the detector is transit time limited the overall effect on bandwidth is small as 3dB bandwidth decreased to 22 GHz for 100µm long detector. However, for designs with ultra-short transit delays, the RC delay effect would be more significant and could dominate the overall detector bandwidth.

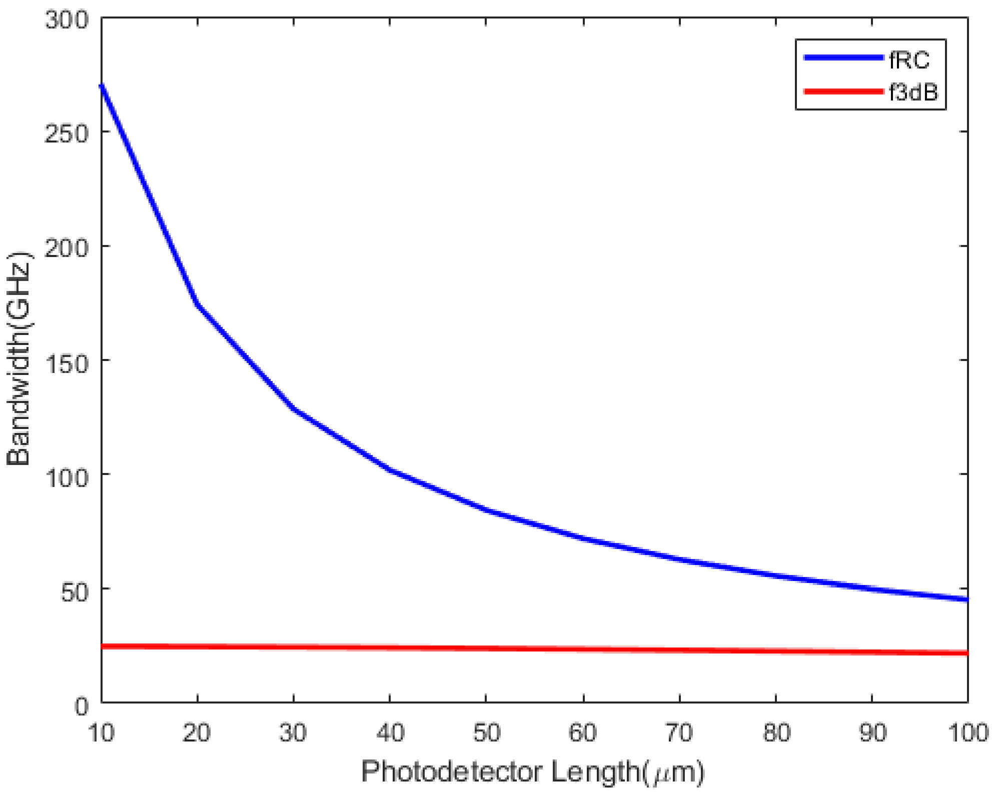

Figure 60: RC-limited bandwidth with respect to detector length.

3.7.2 *Photodetector Thickness Sweep*

Since the photodetector thickness has been the limiting factor for the bandwidth in the previous section, we now optimize the bandwidth by doing a thickness sweep for the photodetector design ranging from 100 nm to 500 nm. In order to systematically analyze the effect of thickness, we fix the length of the photodetector as 50µm long and the width of the Ge region as 2.5µm wide.

The first figure of merit to examine is dark current. Due to the volume-dependent bulk generation component of the dark current, as the thickness of germanium region is increased, the dark current also increases proportionally as shown in Figure 61Figure 61. The dark current ranges from 6.6 nA to 66 nA at 1V reverse bias for 100 nm and 500 nm Ge thicknesses, respectively.

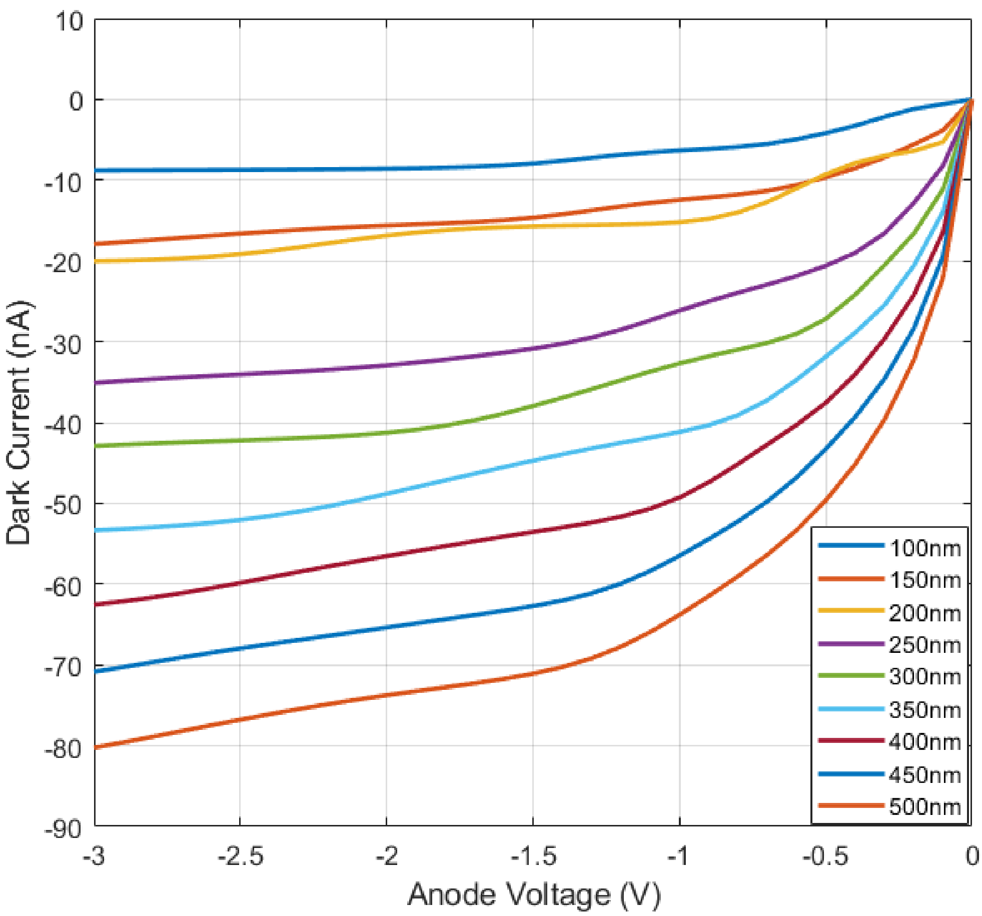

Figure 61: Dark Current for different Ge thicknesses ($100 - 500\ nm$ with $50\ nm$ increments).

Second, we examine the change of responsivity of the detector with respect to Ge thickness. Figure 62Figure 62 shows the simulation results at 1V reverse bias. The important thing to notice is the responsivity shows peak-valley behavior similar to the work of Piels et al. [20]. At 200 nm and 400 nm germanium thickness, the responsivity values are low. This stems from the fact that the absorption profile is determined by the confinement factor of the higher-order mode in the absorbing region as well as the overlap between it and the input mode, both of which are functions of the thickness of the absorbing region [20].

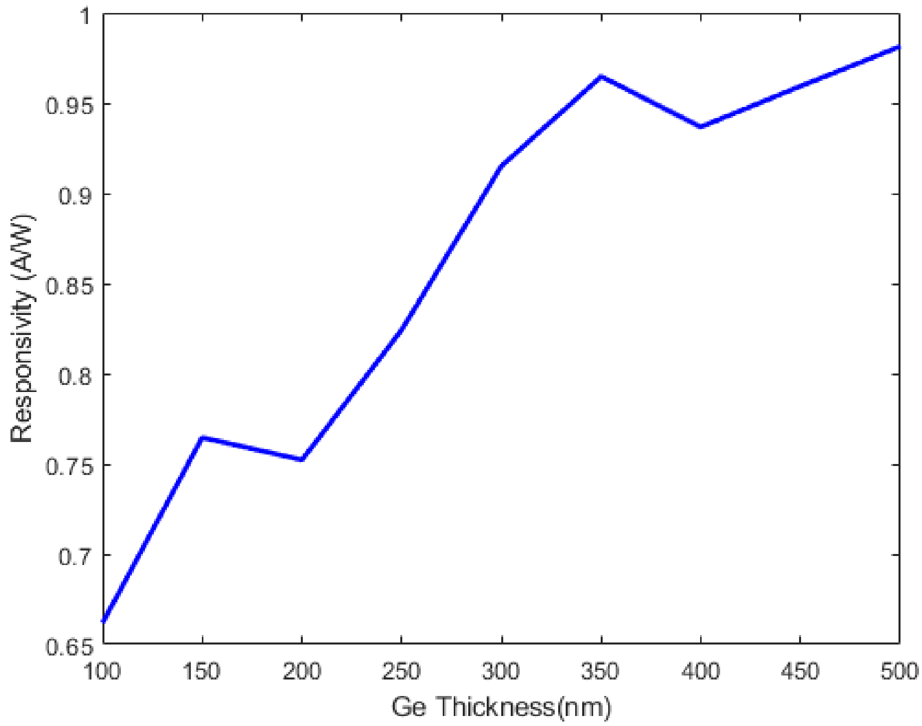

Figure 62: Responsivity for different Ge thickness values.

The next figure of merit is bandwidth. The thickness affects both the depletion region width, which is directly related to transit time, and the junction capacitance. As the thickness of germanium region increases, the depletion region also increases, therefore the transit time for carriers to reach the contacts also increases. This phenomenon can also be seen in Figure 63, where transit time dependent bandwidth ($f_{Transit}$) value decays with red curve as thickness of Ge region increases. On the other hand, from the fundamental definition of the capacitance, as the distance between the parallel plates gets bigger, the capacitance gets smaller. Therefore, RC delay decreases, and RC delay dependent bandwidth (f_{RC}) increases as represented in the blue curve in Figure 63. The point, where the two curves are intersecting each other, is the optimal Ge thickness for the maximum achievable bandwidth given the length and width of the detector. The Ge thickness for the maximum bandwidth point is 418 nm. On the other hand, there is an absorption reduction close to 400 nm, resulting in a lower responsivity value compared to neighboring points. Therefore, for an application where both the responsivity and bandwidth are important, a photodetector design with 450 nm Ge thickness can be a better option as shown in Table 11.

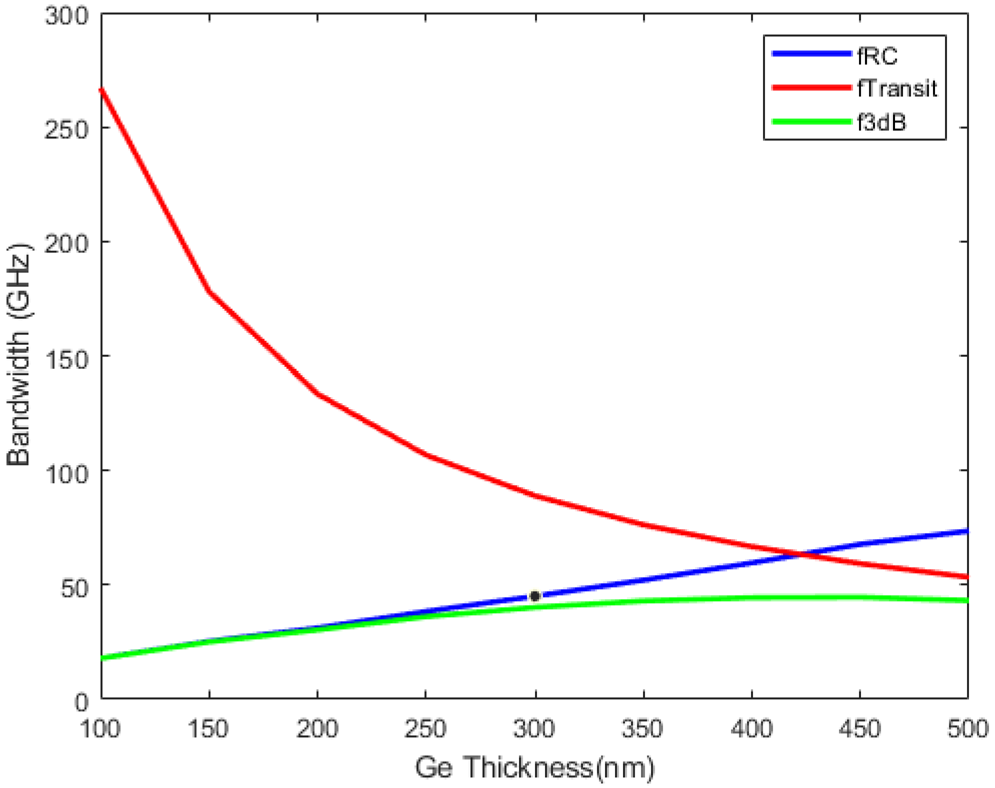

Figure 63: Bandwidth for different Ge thickness values.

Table 11: Responsivity-Bandwidth Product for 400 nm, 450 nm, and 500 nm designs.

Ge Thickness	*Responsivity (A/W)*	*Bandwidth (GHz)*	$R \times B \left(\frac{A}{W} GHz\right)$
400 nm	0.937	44.49	41.69
450 nm	0.959	44.66	42.83
500 nm	0.981	43.2	42.38

3.7.3 Photodetector Width Sweep

In this section of the study, we examine the performance metrics of the photodetector with respect to change in the width of germanium region. In doing so, we keep the length and the thickness of the detector fixed at 50μm and 400 nm, respectively. Then, we sweep the width of the germanium from 2μm to 6.5μm with 0.5μm steps to investigate the effect on responsivity, dark current and bandwidth of the detector.

The optical responsivity of the photodetector is relatively insensitive to germanium width as shown in Table 12. However, the dark current increases with the germanium width. Since, the transit bandwidth is related to thickness of the germanium, rather than the width, the RC delay, which increases with the germanium width, will be the limiting factor in device bandwidth.

Table 12: Responsivity and dark current vs germanium width. (Germanium length and thickness are fixed 50μm and 400 nm, respectively.)

Ge Width (μm)	**Responsivity (A/W)**	**Dark Current (nA)**
2	0.9221	46.2
2.5	0.9368	49.46
3	0.9322	52.07
3.5	0.9352	53.69
4	0.9351	57.15
4.5	0.9458	59.28
5	0.9361	61.38
5.5	0.9404	64.41
6	0.9388	67.2
6.5	0.9369	69.28

The simulation results for capacitance and resistance values are given in Table 13 with respect to change in the germanium region width. Similar to length sweep, capacitance linearly increases with the germanium region width as the junction area increases. In contrast to length sweep, resistance also increases as the germanium width is increased. However, considering a 50Ω load resistor, R_{Load}, in a real scenario, its effect becomes negligible.

Table 13: RC-limited Bandwidth vs germanium width (50Ω load resistance is included in bandwidth calculation).

Ge Width (μm)	Capacitance (fF)	Resistance (Ω)	RC-limited Bandwidth (GHz)	3dB Bandwidth (GHz)
2	41	3.10	73.11	50.18
2.5	50.5	3.13	59.32	44.98
3	61	4.05	48.27	39.55
3.5	71	4.27	41.30	35.44
4	81	4.39	36.13	32.01
4.5	90.5	4.67	32.17	29.15
5	100	5.06	28.90	26.66
5.5	111.25	5.12	25.95	24.29
6	121.3	5.65	23.58	22.31
6.5	130.5	5.78	21.86	20.84

When we further decrease the germanium width, two effects occur. First, the fundamental mode will not be confined within the germanium and the responsivity will decrease as the modes overlap. Second, since the metal contacts should also shrink with the size of the detector, contact resistances begin to increase RC delays and counteract the increases in bandwidth [39].

3.8 Design Guidelines for Waveguide-Integrated Ge Photodetectors

There are three figures of merit for photodetectors consisting of responsivity, dark current and bandwidth. These metrics are optimized according to the geometry of active region of the photodetector. Since there is not a single guideline for optimizing all these metrics at once, optimizing each performance metric is summarized as a design guideline in this chapter. Table 14 summarizes the design considerations for each performance metric.

Table 14: Design considerations for each performance metric.

	Length	**Thickness**	**Width**	**Bias Voltage**
High-Responsivity PD	Increased PD length increases the photodetector responsivity.	Peak-valley behavior occurs.	Does not affect at all.	Applying higher reverse bias increases the photodetector responsivity.
High-Bandwidth PD	Increased PD length increases RC delay which decreases RC-limited bandwidth.	Increased Ge thickness decreases transit time-limited bandwidth whereas higher thickness increases RC-limited bandwidth. Thus, there is an optimal point for 3dB bandwidth.	Increased Ge width decreases RC-limited bandwidth.	Applying higher reverse bias increases the photodetector 3dB bandwidth.
Low-Dark Current PD	Increased PD length increases the dark current.	Increased Ge thickness increases the dark current.	Increased Ge width increases the dark current.	Applying higher reverse bias increases the dark current.

According to the results in Table 14, for applications where high SNR (high responsivity and low dark current) is required and bandwidth is not a priority such as sensing applications, designing longer photodetectors with an optimal Ge thickness and narrow Ge width is reasonable. In order to suppress the effect of dark current, photovoltaic operation (unbiased) of photodetector is crucial.

On the other hand, for applications where the bandwidth is a priority and sufficient SNR is required such as telecom applications, designing shorter and narrower detectors is required in terms of length and width, respectively. For the optimal 3dB bandwidth Ge thickness should be carefully designed. In order to increase SNR, designing narrower Ge width is also crucial. Applying higher reverse bias may increase the overall performance of the photodetector, however increasing the bias further may result in high dark current levels which may limit the SNR. Also, higher voltage levels in any device decreases the reliable performance lifetime of the device and for CMOS compatibility and low power consumption, reverse bias voltage level should not exceed 3V. Finally, as a geometrical result, the footprint of the designed devices is also important. Smaller footprint devices are preferable due to low production cost per device and high yield.

Chapter 4:
APPLICATION SPECIFIC PHOTODETECTOR DESIGNS

In this chapter, two photodetector designs are developed specifically to meet the requirements of OTDR and telecom applications. The requirements of the photodetectors are analyzed from a systems engineer perspective and are given in chapter 2.3. As a result, the required performance metrics are also summarized in Table 15 for each application. Based on the change in performance metrics with varying the geometry of the detector as discussed in chapter 3.7, two optimized device models will be presented throughout this chapter.

Table 15: Summary of performance requirements of photodetectors for each application.

Application	Responsivity	Bandwidth	Dark Current	Bias Voltage
OTDR	$> 1\ A/W$	$> 10\ KHz$	$< 10\ nA$	$\leq 0V$
Telecom	$> 0.6\ A/W$	$> 35\ GHz$	$< 100\ nA$	$\geq -2V$

4.1 OTDR Application

Designing a photodetector for OTDR application requires the device to have high responsivity ($> 1\ A/W$) and low dark current ($< 10\ nA$). Since the bandwidth of the device is not a strict limiting factor, in order to increase the responsivity, increasing the germanium length and thickness would be effective. However, increasing these terms, also linearly increases the dark current. Due to the fact that in our photodetector geometry, which is bottom waveguide coupled, the light is evanescently coupled from silicon waveguide to germanium absorbing region. As the direction of incident light is parallel to length of the device, light absorption is dominantly dependent on the length of the device as demonstrated in the simulations in chapter 3. Therefore, increasing mainly the length of the device is more effective in terms of responsivity per dark current, rather than the thickness.

On the other hand, as we show the results of responsivity simulations in chapter 3 that germanium p-i-n photodetectors have high responsivities at 0V bias. This is important that at 0 V bias technically there is zero dark current and photodetector noise will be dominated mainly by the Johnson noise. Therefore, we prefer a photodetector design having a length longer than our baseline design. The length of the detector both increases the responsivity and decreases the series resistance of the detector. From the results presented in chapter 3.7.1, we choose the longest length for the highest responsivity purpose. Moreover, as the responsivity is the main factor to optimize, we choose the 500 nm thickness as this point is not close to valley as illustrated peak-valley behavior in Figure 62Figure 62. The width of the detector is chosen according to responsivity per series resistance ratio, where 2.5 µm germanium width has the highest score. As a result, the photodetector geometry is determined as having a 100 µm long, 500 nm thick and 2.5 µm wide germanium active region.

The simulation results for given geometry is shown in Table 16.

Table 16: OTDR photodetector performance metrics.

Performance Metric	**Value**
Responsivity	$1.17\ A/W\ @\ 0V$
Resistance	$1.613\ \Omega$
Capacitance	$105\ fF$
Johnson Noise	$56.6\ nA$
NEP	$48.38\ nW(-43.15\ dBm)$
3dB Bandwidth	25.73 GHz
Dynamic Range	$57.66\ dB$
Footprint	$100\mu m \times 2.5\mu m \times 500nm$

As it is mentioned in chapter 2.3.1 that the most important metric for an OTDR photodetector is its dynamic range. In order to calculate the dynamic range, we will first calculate the noise floor for our OTDR photodetector in photovoltaic mode. In photovoltaic mode, at 0 V bias, only the Johnson noise term is dominant as discussed in chapter 2.2. If we calculate the Johnson noise results from $51.613\ \Omega$ series resistance with load operating at $300°K\ at\ 1kHz$:

$$I_{jn} = \sqrt{\frac{4 \times 1.38 \times 10^{-23} \times 300 \times\ 1000}{51.613\ \Omega}} = 56.6\ nA$$

Therefore, NEP for our OTDR detector will be:

$$P_0 = \frac{56.6\, nA}{1.17 A/W} = 48.38\, nW = -43.15\, dBm$$

The upper limit of the dynamic range is determined by the saturation photocurrent which is an experimental value to find. However, the maximum optical input power capacity of an input waveguide is $20\ mW$. Thus, multiplying the maximum optical input power by responsivity ($1.17 A/W$) yields $I_{P-Sat} = 1.17(A/W) \times 20mW = 23.4mA$. Hence, the upper limit can be found as:

$$P_1 = (23.4 \times 10^{-3})^2 \times 51.613 = 28.26\, mW = 14.51\, dBm$$

Therefore, the overall dynamic range is:

$$P_1 - P_0 = 14.51\, dBm - (-43.15\, dBm) = 57.66\, dB$$

which is sufficient for long-haul operation requirements of OTDR systems.

Table 17: Comparison of imec photodetector with our OTDR photodetector [143].

Performance Metric	**This Study**	**imec (TE_SVPINDFCWT_2K_13700_900)**
Responsivity	$1.17\ A/W$ @ $0V$	$1\ A/W$ @ $-1V$
Dark Current	$0\ A$	14 nA
Bandwidth	$25.73\ GHz$	20 GHz
Footprint	$100\mu m \times 2.5\mu m$*	$75\mu m \times 12\mu m$**

*Area of the active region of the photodetector. (Does not include contact pad area.)

**Actual dimensions of active region of the detector are not available in the datasheet. These numbers are approximated according to PDKs given for layout files (.gds).

Table 17 compares imec photodetector (TE_SVPINDFCWT_2K_13700_900) with our photodetector in terms of responsivity, dark current, bandwidth, and footprint. According to available data in the library handbook, among three different designs, this photodetector is chosen for comparison, because it has the highest responsivity to dark current ratio (highest SNR). It is important to notice that the figures of merits of imec photodetector are given under -1V reverse bias. In case of usage at 0V bias, these values may be lower than the presented ones. From these results, it is evident that our photodetector design has superior performance for these figures of merit and its usage for sensing applications (OTDR) would give better results.

The traditional optical time-domain reflectometers are expensive and large in size. The advancement of silicon photonics allows for the creation of small, low-cost optical devices that are compatible with the CMOS fabrication processes. In highly populated fiber interconnects such as backplane distribution harnesses and rack-to-rack links, commercially available OTDR test equipment requires a connector opening, which may not be feasible. Transceiver-integrated monitoring would improve overall network reliability while lowering fiber optic network installation and maintenance expenses.

Typical power levels to be measured by an OTDR varies for different networks. For telecom transmitters, the optical power levels are in between 1 to 10 milliwatts (0 to 10 dBm) and for receivers, typical optical power level is 1 microwatt (-30 dBm). For DWDM systems with fiber amplifiers, transmitter side has optical power levels at 10 to 100 milliwatts (10 to 20 dBm), whereas the optical power levels at receiver side are ranging from 1 to 10 microwatts (-20 to -30 dBm). For data links and LANs, transmitter side has optical power levels at 1 to 10 milliwatts (0 to 10 dBm) for VCSEL and 25 to 100 microwatts (-10 to -16 dBm) for LED. For the receiver side, optical power levels vary from 1 to 25 microwatts (-16 to 30 dBm) [144].

4.2 Telecom Application

Designing a photodetector for telecom application requires ultra-high bandwidths with sufficient sensitivity levels. In chapter 2.3, when we analyze the requirements of 400G-BASE-DR4 ethernet standard, we defined the performance metrics of photodetector to have a bandwidth higher than 35 GHz, responsivity higher than 0.6 A/W and dark current to be lower than 100 nA. Moreover, all these metrics should be satisfied under less than or equal to 2V reverse bias.

Since the bandwidth of the device is the main performance metric, for the geometric optimization of the device we first consider the bandwidth related parameters such as germanium thickness, total resistance, and total capacitance of the device. As it is discussed in chapter 3.7, in order to increase the bandwidth of the detector, germanium thickness should be small enough, so as not to limit the bandwidth due to carrier transitions. Also, as the device capacitance is mainly related with the depletion region, decreasing the germanium thickness may result in increasing the capacitance, thus, the bandwidth may be limited by the RC delay of the device. Moreover, the length and width of the germanium region should be sufficiently small to keep the capacitance at low levels. The series resistance of the device decreases with the device length, whereas this resistance increases with the device width. As a result, in contrast to OTDR detector, telecom detector will have a smaller footprint.

Moreover, in terms of responsivity, it is important to mention that the absorption spectrum of 10 μm long germanium p-i-n photodiode is shown in Figure 64Figure 64. For the telecom application, according to 400G-BASE-DR4 standard, 1310 nm center wavelength is used. As seen in Figure 64, for 1310 nm spectrum absorption of the photodetector is much better than that of at 1550 nm. Therefore, designing a shorter photodetector is feasible.

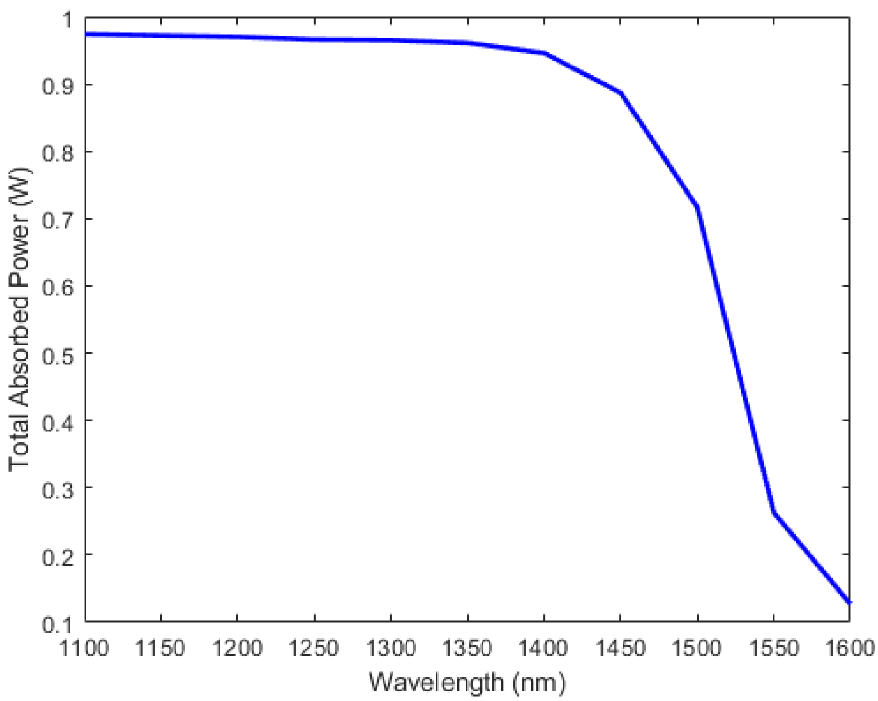

Figure 64: Absorption profile vs wavelength.

For low BER communications, the dark current level of the detector is as important as responsivity. Therefore, a photodetector design with 2 μm wide germanium region is chosen which also further enhances the bandwidth of the device due to small capacitance level. Since the bandwidth is the main motive, detector with 300 nm germanium thickness is chosen. The theoretical transit time limited bandwidth at this thickness is 89 GHz. Therefore, the RC bandwidth higher than this value is preferred in order not to limit the bandwidth with RC delay.

Three different designs with 10 μm, 20 μm, and 30 μm length germanium region is created. The performance metrics of these designs at 2V reverse bias are given in Table 18.

Table 18: Comparison of candidate designs.

Length	Dark Current (nA)	Responsivity (A/W)	Bandwidth (GHz)
$\mathbf{10\mu m}$	8.67	0.972	84.26
$\mathbf{20\mu m}$	17.3	0.979	76.02
$\mathbf{30\mu m}$	26.02	0.981	66.94

As a result, for the telecom application the best suited design is the shortest design with 10 μm long germanium region, because it has the lowest dark current and the highest bandwidth. The noise analysis of the device can be done as follows. The Johnson noise at 300°K and at 84.26 GHz is equal to:

$$I_{jn} = \sqrt{\frac{4 \times 1.38 \times 10^{-23} \times 300 \times 84.26 \times 10^{9}}{77}} = 4.25\ \mu A$$

The shot noise is calculated as,

$$I_{sn} = \sqrt{2 \times 1.602 \times 10^{-19} \times 8.67 \times 10^{-9} \times 84.26 \times 10^{9}} = 15.3\ nA$$

Therefore, the total noise is dominated by Johnson (thermal) noise:

$$I_{tn} = \sqrt{{I_{sn}}^2 + {I_{jn}}^2} = 4.25\ \mu A$$

However, there is also TIA noise besides the noise originating from the photodetector. The TIA driven noise can be approximated as 15 $pA/\sqrt{Hz}$ [141] which is equal to 4.35 µA at 84.26 GHz operation. Then, the resulting NEP can be calculated as,

$$NEP = \frac{I_{tn}}{R} = \frac{(4.35\ + 4.25)\mu A}{0.972\ A/W} = 8.85\ \mu W = -20.53\ dBm$$

which is far below the minimum required receiver sensitivity (-9.25 dBm).

Adapting the photodetectors into optical PAM4 transceiver circuit in Lumerical Interconnect, the overall circuitry becomes as in Figure 65Figure 65. This circuit is composed of two pseudo-random bit stream (PRBS) block, 2 non-return-to-zero (NRZ) pulse generator, 1 continuous-wave laser, 3 fork, 2 electrical NOT gate, 1 optical phase shifter, 2 waveguide coupler, 4 optical modulator, eye diagram analyzer, vector signal analyzer (VSA), low pass filter, transimpedance amplifier (TIA) and 2 PIN photodetectors.

In the signal generation phase, NRZ pulse generators creates the electrical signal, and the fork splitter duplicates these signals to drive the modulators. There are two cascaded phase modulators in each branch results in 4-level modulated optical signal. The modulated optical output signal is detected by two PIN photodetectors. The upper branch is used as a reference for the eye diagram whereas the lower branch is degraded by a low pass filter to simulate the bandwidth of the photodetector. There are four different levels of modulated signal around 0.001a.u., 0.000824a.u., 0.00065a.u. and 0.00049a.u. Using $1k\Omega$ TIA modulated signals are amplified by 1000.

The eye diagram for 100 Gbps (50 GBaud/s) and 150 Gbps (75 GBaud/s) bitrates are shown as in Figure 66-67. It can be seen that at 100 Gbps the eyes are wide open, and the Q-factor value given by VNA is 6.68 ($SER\ = 11.64 \times 10^{-11}$) and 7.75 ($SER\ = 4.73 \times 10^{-15}$) for 50 GBaud/s and 75 GBaud/s, respectively.

Table 19: Comparison of imec photodetector with our telecom photodetector [143].

Performance Metric	**This Study**	**imec (TE_SVPINCFCWT_1K_15400_600)**
Responsivity	$0.972\ A/W\ @\ -2V$	$0.6\ A/W\ @\ -2V$
Dark Current	$8.67\ nA$	140 nA
Bandwidth	$84.26\ GHz$	50 GHz
Footprint	$10\mu m \times 2\mu m$*	$76\mu m \times 12\mu m$**

* Area of the active region of the photodetector. (Does not include contact pad area.)

** Actual dimensions of active region of the detector are not available in the datasheet. These numbers are approximated according to PDKs given for layout files (.gds).

Table 19 compares imec photodetector (TE_SVPINCFCWT_1K_15400_600) with our photodetector in terms of responsivity, dark current, bandwidth, and footprint. According to available data in the library handbook, among three different designs, this photodetector is chosen for comparison, because it has the highest bandwidth (50 GHz). From these results, it is evident that our photodetector design has superior performance for these figures of merits and its usage for telecom applications would yield better results.

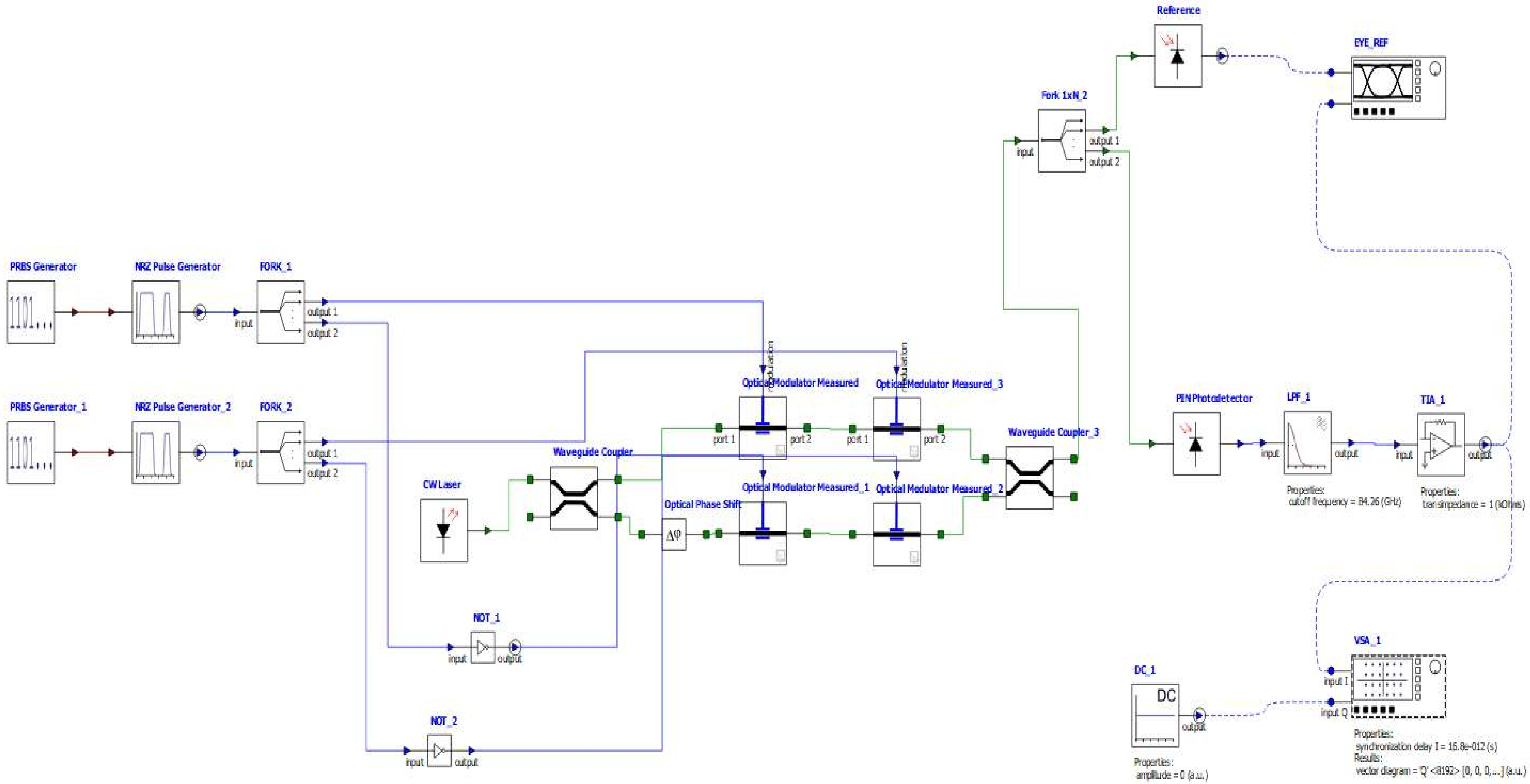

Figure 65: Optical PAM4 transceiver.

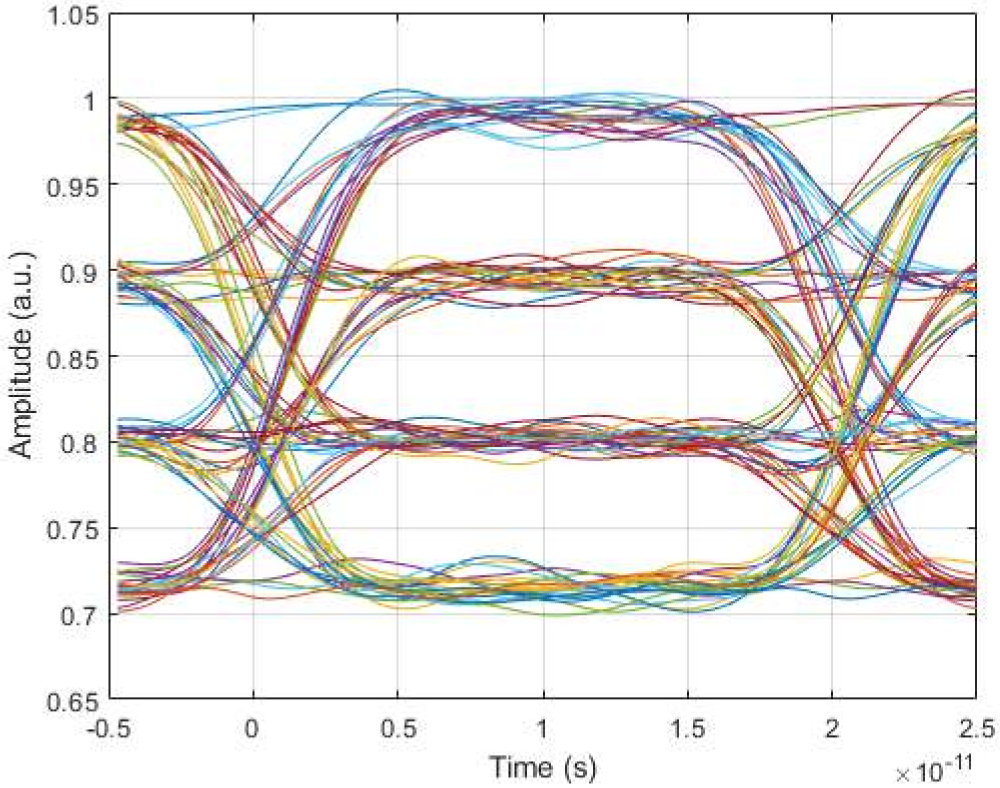

Figure 66: Eye diagram of telecom photodetector at 50 GBaud/s PAM4 signal.

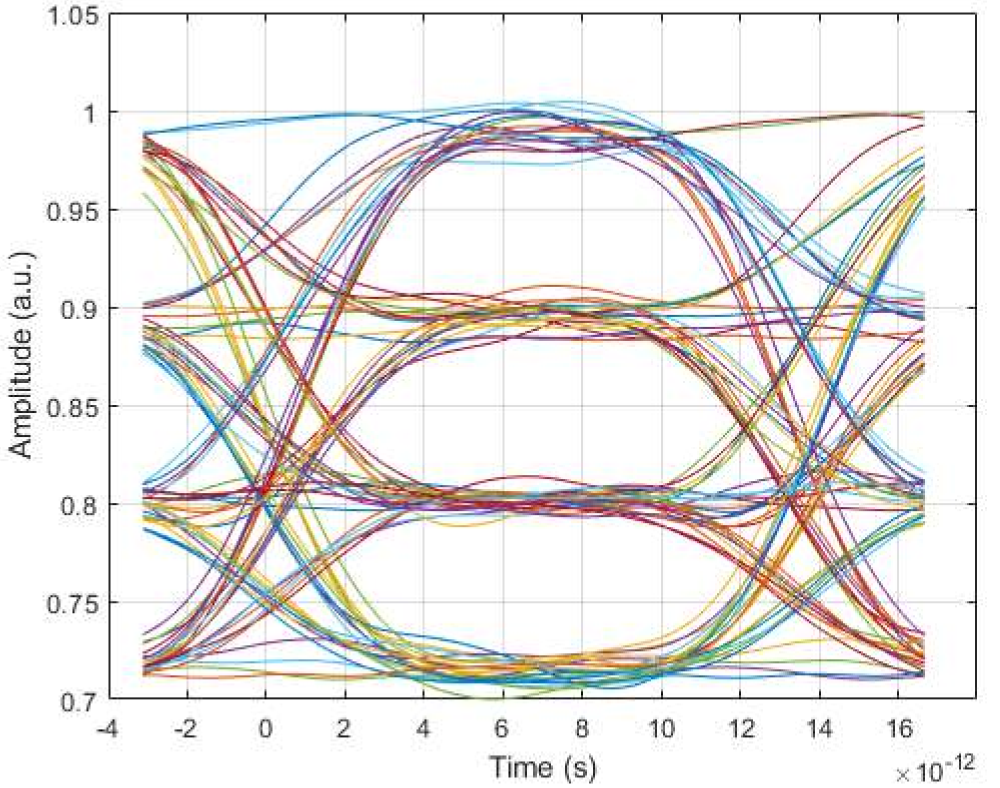

Figure 67: Eye diagram of telecom photodetector at 75 GBaud/s PAM4 signal.

4.3 *Other Design Considerations in Waveguide-Integrated Photodetectors*

Apart from this study, there are several other design considerations in waveguide-integrated photodetectors to further optimize the performance metrics such as bandwidth, responsivity and dark current. There is no all-in-one photodetector in terms of figures of merit such as higher than $100\ GHz$ bandwidth, higher than $5\ AW^{-1}$ responsivity and lower than $1\ nA$ dark current with a sub-micron footprint. However, in order to maximize some of these metrics, there are different methodologies in the literature that are studied by researchers.

Using different materials for photodetection such as GaInAs, InP, graphene, or multi-layer combinations of these materials can increase the bandwidth beyond 100 GHz [145-147]. Designing lateral geometry or more compact photodetectors can decrease the carrier transit time and transit-time limited bandwidth can be enhanced [88, 148] or carrier velocity can be increased by using a uni-traveling carrier structure [146]. Another method to increase transit-time limited bandwidth is to utilize resonant-cavity-enhanced photodetectors where a thin photo-absorption layer is sandwiched between two reflectors [147]. Moreover, exploiting the plasmonic effects [9, 149, 150] or inductive gain peaking [62, 79, 151] can also increase the bandwidth.

To obtain responsivity values higher than $5\ AW^{-1}$, the fundamental solution proposed by the researchers is utilizing avalanche photodetectors due to their internal carrier multiplication mechanism [25, 152, 153]. Besides this, changing the position of metallic contacts on top of photo-absorbing layer (i.e., utilizing two off-centered contacts) [79], or exploiting distributed Bragg reflectors (DBR) [78], or adding photonic bandgaps and photonic crystals on Si substrate [90] are several solutions to improve responsivity performance of waveguide-integrated photodetectors.

Achieving sub-micron footprint and less than $1\ nA$ dark current levels are related metrics due to volume-dependent bulk generation characteristics of dark current. Therefore, any methodology enabling more compact design is useful in this sense. Optimized DBR location on waveguides [78], butt-coupling [154], and dual injection photodetectors [155] are several techniques to obtain smaller devices. Furthermore, advanced metallization techniques [156] and material and fabrication qualities [157, 158] can also decrease dark current levels.

Chapter 5:
CONCLUSIONS AND FUTURE WORK

5.1 Summary and Conclusions

Technological developments and increasing data traffic compelled the development of silicon photonics technology. Photodetectors have been one of the most important components of silicon photonics that played a significant role achieving increased data rates in communications. Photodetectors can achieve high responsivity [72, 75, 79, 83], ultra-wide bandwidth [62, 76, 77, 83, 88], small footprint and CMOS integration [84, 87, 89], ultra-low dark current [74, 77, 78, 81]. Photodetectors with different performance metrics need to be developed for different applications such as sensing, imaging, holographic data storage, free-space optics [159-161].

Waveguide-integrated germanium photodetectors suitable for CMOS fabrication technology are the most widely studied group in the literature [72, 74, 85]. State-of-the-art photodetectors with different geometries with different coupling techniques have been investigated [31, 73, 83, 115, 162]. Photodetectors with vertical p-i-n junction, bottom-coupled design have been the focus of this research due to their successful reproducibility and scalability in production [93]. Changes in geometric measurements of photodetectors of this type directly affect performance metrics such as responsivity, bandwidth and dark current. In this study, photodetectors with different geometries have been designed for different applications.

In this study, the semiconductor physics of photodetectors in vertical p-i-n orientation was investigated in detail. The effects of length, width, and height changes in photodetector geometry on photodetector performance metrics such as bandwidth, responsivity and dark current have been investigated with simulations. With the experience gained from the simulations, this thesis aims to realize different photodetector designs suitable for different application requirements.

Due to their differences in application requirements, two different types of photodetector designs have been developed. The photodetector developed for sensing (OTDR) application has been developed to have a wide dynamic range with high responsivity and low dark current so that it can be used at long-haul operations. For this reason, it has ultra-high responsivity $(1.17\,A/W)$ and relatively low bandwidth

(25.73 GHz). In order to eliminate shot noise, OTDR photodetector is unbiased so that it has minimal dark current. In these circumstances, it has only 48.38 nW noise equivalent power (NEP) due to Johnson noise. It has ultra-wide dynamic range (57.66 dB) which is more than the long-haul operation optical loss budget limit. The physical dimensions of the OTDR photodetector that is determined by the germanium region are $100\ \mu m \times 500\ nm \times 2.5\ \mu m$ ($L \times T \times W$).

The second photodetector developed in this study is based on the requirements of the 400G-BASE-DR4 ethernet standard. As it is developed for telecom application, this photodetector is designed to have ultra-high bandwidth (84.26 GHz), sufficiently high responsivity ($0.972\ A/W$) and low noise so that the minimum receiver sensitivity ($-20.53\ dBm$) is maintained lower than the 400G-BASE-DR4 requirements ($-9.25\ dBm$). The physical dimensions of the telecom photodetector that is determined by the germanium region are $10\ \mu m \times 300\ nm \times 2\ \mu m$ ($L \times T \times W$).

5.2 *Future Work and Outlook*

While waveguide-integrated photodetectors on silicon photonic platform have been developed towards commercial applications, there are many different potentially disruptive directions for extreme figures of merit, new applications or new photodetection physics.

(1) Hybrid integration of 2D materials with Si, Ge:

Graphene, 2D transition metal dichalcogenides, and 2D layers could allow for non-volatile, ultra-wide band detection in mid, far IR or extreme UV [163, 164]. They can also allow for active tuning of bandgap, hence the wavelength of interest can be actively tuned.

(2) Packaging solutions for high-density integration of photodetectors:

One of the major bottlenecks in photonic integrated circuits and detectors is the expensive, partly manual, and large footprint packaging solutions [165, 166]. Since thermal management as well as electronic wire bonding, fiber optical epoxy binding, and mechanical and EMC/EMI shielding must be achieved, some of the most complex packaging methods must be combined. Otherwise, the advantages of silicon integrated photonics might not be fully utilized.

(3) Advanced geometries, doping profiles, and detector bias conditions for inter-sub band photodetection, quantum-confined or plasmonic focusing for spectral selectivity could extend the applications beyond near infrared [167-169].

(4) Advanced read-out electronics for single or arrays of integrated photodetector could help reduce the total NEP and improve sensitivity.

(5) Advanced fabrication and patterning techniques for CMOS compatible nanostructured detectors could enable applications in LIDAR, camera, and other optoelectronic hyperspectral imaging systems [170-172].

BIBLIOGRAPHY

[1] J. D. Cressler, *Silicon Earth: Introduction to Microelectronics and Nanotechnology*. CRC Press, 2017.

[2] S. Gaudin, "The transistor: The most important invention of the 20th century?," *Computerworld,* 2007. [Online]. Available: https://www.computerworld.com/article/2538123/the-transistor--the-most-important-invention-of-the-20th-century-.html.

[3] J. S. Kilby, "Miniaturized electronic circuits," Patent Application 1959.

[4] N. Margalit, C. Xiang, S. M. Bowers, A. Bjorlin, R. Blum, and J. E. Bowers, "Perspective on the future of silicon photonics and electronics," *Applied Physics Letters,* vol. 118, no. 22, p. 220501, 2021.

[5] C. Mack, "The Multiple Lives of Moore's Law," *IEEE Spectrum,* 2015.

[6] A. Danowitz, K. Kelley, J. Mao, J. P. Stevenson, and M. Horowitz, "CPU DB: Recording Microprocessor History: With this open database, you can mine microprocessor trends over the past 40 years," *Queue,* vol. 10, no. 4, pp. 10-27, 2012.

[7] A. Hartstein and T. R. Puzak, "Optimum power/performance pipeline depth," in *Proceedings. 36th Annual IEEE/ACM International Symposium on Microarchitecture, 2003. MICRO-36.*, 5-5 Dec. 2003 2003, pp. 117-125, doi: 10.1109/MICRO.2003.1253188.

[8] E. S. Magden, "Optical signal generation, stabilization, and manipulation in broadband silicon photonics," Massachusetts Institute of Technology, 2018.

[9] E. Panchenko, "Plasmonics-enabled semiconductor photodetectors," 2017.

[10] A. K. Sinha, J. A. Cooper, and H. J. Levinstein, "Speed limitations due to interconnect time constants in VLSI integrated circuits," *IEEE Electron Device Letters,* vol. 3, no. 4, pp. 90-92, 1982, doi: 10.1109/EDL.1982.25491.

[11] D. Korn, *Silicon-Organic Hybrid Platform for Photonic Integrated Circuits*. KIT Scientific Publishing, 2015.

[12] M. T. Bohr, "Interconnect scaling-the real limiter to high performance ULSI," in *Proceedings of International Electron Devices Meeting*, 1995: IEEE, pp. 241-244.

[13] C. Diaz *et al.*, "A 0.18/spl mu/m cmos logic technology with dual gate oxide and low-k interconnect for high-performance and low-power applications," in *1999 Symposium on VLSI Technology. Digest of Technical Papers (IEEE Cat. No. 99CH36325)*, 1999: IEEE, pp. 11-12.

[14] R. Liu, C.-S. Pai, and E. Martinez, "Interconnect technology trend for microelectronics," *Solid-State Electronics,* vol. 43, no. 6, pp. 1003-1009, 1999.

[15] W. Bogaerts *et al.*, "Nanophotonic waveguides in silicon-on-insulator fabricated with CMOS technology," *Journal of Lightwave Technology,* vol. 23, no. 1, pp. 401-412, 2005.

[16] B. Jalali, M. Paniccia, and G. Reed, "Silicon photonics," *IEEE Microwave Magazine,* vol. 7, no. 3, pp. 58-68, 2006, doi: 10.1109/MMW.2006.1638290.

[17] A. Rahim, T. Spuesens, R. Baets, and W. Bogaerts, "Open-access silicon photonics: Current status and emerging initiatives," *Proceedings of the IEEE,* vol. 106, no. 12, pp. 2313-2330, 2018.

[18] M. Salib *et al.*, "Silicon Photonics," *Intel Technology Journal,* vol. 8, no. 2, 2004.

[19] J. Wang and Y. Long, "On-chip silicon photonic signaling and processing: a review," *Science Bulletin,* vol. 63, no. 19, pp. 1267-1310, 2018.

[20] M. Piels and J. E. Bowers, "Photodetectors for silicon photonic integrated circuits," *Photodetectors,* pp. 3-20, 2016.
[21] P. Cheben *et al.*, "A high-resolution silicon-on-insulator arrayed waveguide grating microspectrometer with sub-micrometer aperture waveguides," *Optics express,* vol. 15, no. 5, pp. 2299-2306, 2007.
[22] P. Dumon *et al.*, "Low-loss SOI photonic wires and ring resonators fabricated with deep UV lithography," *IEEE Photonics Technology Letters,* vol. 16, no. 5, pp. 1328-1330, 2004.
[23] Q. Xu, B. Schmidt, S. Pradhan, and M. Lipson, "Micrometre-scale silicon electro-optic modulator," *nature,* vol. 435, no. 7040, pp. 325-327, 2005.
[24] W. Zhang, M. Chan, R. Huang, and P. K. Ko, "High gain gate/body tied NMOSFET photo-detector on SOI substrate for low power applications," *Solid-State Electronics,* vol. 44, no. 3, pp. 535-540, 2000.
[25] H. Chen, "Advanced germanium pin and avalanche photodetectors for low-power optical interconnects," Ghent University, 2016.
[26] Y. T. L. Johnny, "Challenges of Silicon Photonics Testing from A Foundry's Perspective," Presentation 2019. [Online]. Available: https://www.slideshare.net/TiongLehYap/challenges-of-silicon-photonics-testing-from-a-foundrys-perspectivesemicon2016.
[27] S. Lin, E. Schonbrun, and K. Crozier, "Optical manipulation with planar silicon microring resonators," *Nano letters,* vol. 10, no. 7, pp. 2408-2411, 2010.
[28] X. Mu, S. Wu, L. Cheng, and H. Y. Fu, "Edge Couplers in Silicon Photonic Integrated Circuits: A Review," *Applied Sciences,* vol. 10, no. 4, p. 1538, 2020. [Online]. Available: https://www.mdpi.com/2076-3417/10/4/1538.
[29] S. Nambiar, P. Sethi, and S. K. Selvaraja, "Grating-assisted fiber to chip coupling for SOI photonic circuits," *Applied Sciences,* vol. 8, no. 7, p. 1142, 2018.
[30] G. T. Reed, G. Mashanovich, F. Y. Gardes, and D. Thomson, "Silicon optical modulators," *Nature photonics,* vol. 4, no. 8, pp. 518-526, 2010.
[31] H. Yang, *Effcient Coupling Interfaces for Silicon Photonics Applications*. McGill University (Canada), 2019.
[32] M. Dasan, F. Francis, K. T. Sarath, E. Dipin, and T. Srinivas, "Optically Multiplexed Systems: Wavelength Division Multiplexing," in *Multiplexing*: IntechOpen, 2019.
[33] W. Bogaerts *et al.*, "Silicon microring resonators," *Laser & Photonics Reviews,* vol. 6, no. 1, pp. 47-73, 2012.
[34] R. Soref and B. Bennett, "Electrooptical effects in silicon," *IEEE journal of quantum electronics,* vol. 23, no. 1, pp. 123-129, 1987.
[35] C. Sun *et al.*, "Single-chip microprocessor that communicates directly using light," *Nature,* vol. 528, no. 7583, pp. 534-538, 2015.
[36] M. Hochberg *et al.*, "Silicon Photonics: The Next Fabless Semiconductor Industry," *IEEE Solid-State Circuits Magazine,* vol. 5, no. 1, pp. 48-58, 2013, doi: 10.1109/MSSC.2012.2232791.
[37] R. Soref, "The past, present, and future of silicon photonics," *IEEE Journal of selected topics in quantum electronics,* vol. 12, no. 6, pp. 1678-1687, 2006.
[38] I. P. S. R.-. International, "Silicon Photonics," 2020.
[39] L. Chrostowski and M. Hochberg, *Silicon photonics design: from devices to systems*. Cambridge University Press, 2015.

[40] C. A. Brackett, "Dense wavelength division multiplexing networks: Principles and applications," *IEEE Journal on Selected areas in Communications,* vol. 8, no. 6, pp. 948-964, 1990.

[41] G. Li, "Recent advances in coherent optical communication," *Advances in optics and photonics,* vol. 1, no. 2, pp. 279-307, 2009.

[42] L. Brian Welch, "400G Optics - Technologies, Timing, and Transceivers," Presentation 2014.

[43] V. Solutions, "SmartOTDR Handheld Fiber Tester," Datasheet 2021.

[44] V. Solutions, "Working Principle & Characteristics of OTDRs," 2021. [Online]. Available: https://www.viavisolutions.com/en-uk/working-principle-characteristics-otdrs.

[45] M. Morse, "SEMICONDUCTOR DETECTORS: Germanium on silicon approaches III-V semiconductors in performance," 2007. [Online]. Available: https://www.laserfocusworld.com/detectors-imaging/article/16552968/semiconductor-detectors-germanium-on-silicon-approaches-iiiv-semiconductors-in-performance.

[46] R. Hui, *Introduction to fiber-optic communications*. Academic Press, 2019.

[47] B. Nabet, *Photodetectors: materials, devices and applications in communications and imaging technologies*. Elsevier Science & Technology, 2015.

[48] B. E. Saleh and M. C. Teich, *Fundamentals of photonics*. john Wiley & sons, 2019.

[49] J. J. Ackert, A. S. Karar, J. C. Cartledge, P. E. Jessop, and A. P. Knights, "Monolithic silicon waveguide photodiode utilizing surface-state absorption and operating at 10 Gb/s," *Optics express,* vol. 22, no. 9, pp. 10710-10715, 2014.

[50] J. J. Ackert, A. S. Karar, D. J. Paez, P. E. Jessop, J. C. Cartledge, and A. P. Knights, "10 Gbps silicon waveguide-integrated infrared avalanche photodiode," *Optics express,* vol. 21, no. 17, pp. 19530-19537, 2013.

[51] J. Bradley, P. Jessop, and A. Knights, "Silicon waveguide-integrated optical power monitor with enhanced sensitivity at 1550 nm," *Applied Physics Letters,* vol. 86, no. 24, p. 241103, 2005.

[52] H.-H. Chang, Y.-h. Kuo, R. Jones, A. Barkai, and J. E. Bowers, "Integrated hybrid silicon triplexer," *Optics express,* vol. 18, no. 23, pp. 23891-23899, 2010.

[53] L. Colace *et al.*, "Metal–semiconductor–metal near-infrared light detector based on epitaxial Ge/Si," *Applied Physics Letters,* vol. 72, no. 24, pp. 3175-3177, 1998.

[54] J. Doylend, P. Jessop, and A. Knights, "Silicon photonic resonator-enhanced defect-mediated photodiode for sub-bandgap detection," *Optics express,* vol. 18, no. 14, pp. 14671-14678, 2010.

[55] M. Geis, S. Spector, M. Grein, J. Yoon, D. Lennon, and T. Lyszczarz, "Silicon waveguide infrared photodiodes with> 35 GHz bandwidth and phototransistors with 50 AW-1 response," *Optics Express,* vol. 17, no. 7, pp. 5193-5204, 2009.

[56] I. Goykhman, B. Desiatov, J. Khurgin, J. Shappir, and U. Levy, "Locally-oxidized silicon surface-plasmon Schottky detector for telecom wavelengths," in *8th IEEE International Conference on Group IV Photonics*.

[57] I. Goykhman, B. Desiatov, J. Khurgin, J. Shappir, and U. Levy, "Waveguide based compact silicon Schottky photodetector with enhanced responsivity in the telecom spectral band," *Optics express,* vol. 20, no. 27, pp. 28594-28602, 2012.

[58] R. R. Grote, K. Padmaraju, B. Souhan, J. B. Driscoll, K. Bergman, and R. M. Osgood, "10 Gb/s Error-Free Operation of All-Silicon Ion-Implanted-Waveguide

Photodiodes at 1.55$\mu {\rm m} $," *IEEE Photonics Technology Letters,* vol. 25, no. 1, pp. 67-70, 2012.
[59] A. Knights, J. Bradley, S. Gou, and P. Jessop, "Silicon-on-insulator waveguide photodetector with self-ion-implantation-engineered-enhanced infrared response," *Journal of Vacuum Science & Technology A: Vacuum, Surfaces, and Films,* vol. 24, no. 3, pp. 783-786, 2006.
[60] R. Ichikawa, S. Takita, Y. Ishikawa, and K. Wada, "Germanium as a material to enable silicon photonics," *Silicon Photonics II,* pp. 131-141, 2011.
[61] T.-Y. Liow *et al.*, "Silicon modulators and germanium photodetectors on SOI: monolithic integration, compatibility, and performance optimization," *IEEE Journal of Selected Topics in Quantum Electronics,* vol. 16, no. 1, pp. 307-315, 2009.
[62] A. Novack *et al.*, "Germanium photodetector with 60 GHz bandwidth using inductive gain peaking," *Optics express,* vol. 21, no. 23, pp. 28387-28393, 2013.
[63] J. Michel, J. Liu, and L. C. Kimerling, "High-performance Ge-on-Si photodetectors," *Nature photonics,* vol. 4, no. 8, pp. 527-534, 2010.
[64] S. Fama, L. Colace, G. Masini, G. Assanto, and H.-C. Luan, "High performance germanium-on-silicon detectors for optical communications," *Applied Physics Letters,* vol. 81, no. 4, pp. 586-588, 2002.
[65] Z. Huang *et al.*, "21-GHz-bandwidth germanium-on-silicon photodiode using thin SiGe buffer layers," *IEEE Journal of selected topics in quantum electronics,* vol. 12, no. 6, pp. 1450-1454, 2006.
[66] M. Jutzi, M. Berroth, G. Wohl, M. Oehme, and E. Kasper, "Ge-on-Si vertical incidence photodiodes with 39-GHz bandwidth," *IEEE Photonics Technology Letters,* vol. 17, no. 7, pp. 1510-1512, 2005.
[67] J. Liu *et al.*, "High-performance, tensile-strained Ge p-i-n photodetectors on a Si platform," *Applied Physics Letters,* vol. 87, no. 10, p. 103501, 2005.
[68] T. Loh *et al.*, "Selective epitaxial germanium on silicon-on-insulator high speed photodetectors using low-temperature ultrathin Si 0.8 Ge 0.2 buffer," *Applied Physics Letters,* vol. 91, no. 7, p. 073503, 2007.
[69] M. Oehme, J. Werner, E. Kasper, M. Jutzi, and M. Berroth, "High bandwidth Ge p-i-n photodetector integrated on Si," *Applied physics letters,* vol. 89, no. 7, p. 071117, 2006.
[70] M. Rouvière *et al.*, "Ultrahigh speed germanium-on-silicon-on-insulator photodetectors for 1.31 and 1.55 μ m operation," *Applied Physics Letters,* vol. 87, no. 23, p. 231109, 2005.
[71] S. Samavedam, M. Currie, T. Langdo, and E. Fitzgerald, "High-quality germanium photodiodes integrated on silicon substrates using optimized relaxed graded buffers," *Applied Physics Letters,* vol. 73, no. 15, pp. 2125-2127, 1998.
[72] D. Ahn *et al.*, "High performance, waveguide integrated Ge photodetectors," *Optics express,* vol. 15, no. 7, pp. 3916-3921, 2007.
[73] D. Ahn, L. C. Kimerling, and J. Michel, "Evanescent coupling device design for waveguide-integrated group IV photodetectors," *Journal of lightwave technology,* vol. 28, no. 23, pp. 3387-3394, 2010.
[74] M. Beals *et al.*, "Process flow innovations for photonic device integration in CMOS," in *Silicon Photonics III*, 2008, vol. 6898: International Society for Optics and Photonics, p. 689804.

[75] D. Benedikovic *et al.*, "25 Gbps low-voltage hetero-structured silicon-germanium waveguide pin photodetectors for monolithic on-chip nanophotonic architectures," *Photonics Research,* vol. 7, no. 4, pp. 437-444, 2019.
[76] G. Chen, Y. Yu, S. Deng, L. Liu, and X. Zhang, "Bandwidth improvement for germanium photodetector using wire bonding technology," *Optics express,* vol. 23, no. 20, pp. 25700-25706, 2015.
[77] H. Chen *et al.*, "− 1 V bias 67 GHz bandwidth Si-contacted germanium waveguide pin photodetector for optical links at 56 Gbps and beyond," *Optics Express,* vol. 24, no. 5, pp. 4622-4631, 2016.
[78] J. Cui and Z. Zhou, "High-performance Ge-on-Si photodetector with optimized DBR location," *Optics letters,* vol. 42, no. 24, pp. 5141-5144, 2017.
[79] M. M. P. Fard, G. Cowan, and O. Liboiron-Ladouceur, "Responsivity optimization of a high-speed germanium-on-silicon photodetector," *Optics express,* vol. 24, no. 24, pp. 27738-27752, 2016.
[80] D. Feng *et al.*, "High-speed Ge photodetector monolithically integrated with large cross-section silicon-on-insulator waveguide," *Applied Physics Letters,* vol. 95, no. 26, p. 261105, 2009.
[81] X.-L. Li *et al.*, "High-Performance Germanium Waveguide Photodetectors on Silicon," *Chinese Physics Letters,* vol. 37, no. 3, p. 038503, 2020/03 2020, doi: 10.1088/0256-307x/37/3/038503.
[82] S. Liao *et al.*, "36 GHz submicron silicon waveguide germanium photodetector," *Optics express,* vol. 19, no. 11, pp. 10967-10972, 2011.
[83] S. Lischke *et al.*, "High bandwidth, high responsivity waveguide-coupled germanium pin photodiode," *Optics express,* vol. 23, no. 21, pp. 27213-27220, 2015.
[84] J. Liu *et al.*, "Waveguide integrated Ge pin photodetectors on a silicon-on-insulator platform," in *2006 Optics Valley of China International Symposium on Optoelectronics*, 2006: IEEE, pp. 1-4.
[85] G. Masini, S. Sahni, G. Capellini, J. Witzens, and C. Gunn, "High-speed near infrared optical receivers based on Ge waveguide photodetectors integrated in a CMOS process," *Advances in Optical Technologies,* vol. 2008, pp. 1-5, 2008.
[86] L. Vivien *et al.*, "40 Gb/s lateral vs vertical Ge-on-Si photodetectors integrated in silicon waveguides."
[87] L. Vivien *et al.*, "42 GHz pin Germanium photodetector integrated in a silicon-on-insulator waveguide," *Optics express,* vol. 17, no. 8, pp. 6252-6257, 2009.
[88] L. Vivien *et al.*, "Zero-bias 40Gbit/s germanium waveguide photodetector on silicon," *Optics express,* vol. 20, no. 2, pp. 1096-1101, 2012.
[89] T. Yin *et al.*, "31GHz Ge nip waveguide photodetectors on Silicon-on-Insulator substrate," *Optics express,* vol. 15, no. 21, pp. 13965-13971, 2007.
[90] H. Zhou and Y. Sun, "Size reduction of Ge-on-Si photodetectors via a photonic bandgap," *Applied optics,* vol. 57, no. 12, pp. 2962-2966, 2018.
[91] D. Benedikovic *et al.*, "Silicon–germanium receivers for short-wave-infrared optoelectronics and communications," *Nanophotonics,* vol. 10, no. 3, pp. 1059-1079, 2021, doi: doi:10.1515/nanoph-2020-0547.
[92] X. Zhao *et al.*, "Design impact on the performance of Ge PIN photodetectors," *Journal of Materials Science: Materials in Electronics,* vol. 31, no. 1, pp. 18-25, 2020.
[93] V. A. Vu, D. E. Ioannou, R. Kamocsai, S. L. Hyland, A. Pomerene, and D. Carothers, "PIN Germanium Photodetector Fabrication Issues and

Manufacturability," *IEEE Transactions on Semiconductor Manufacturing,* vol. 23, no. 3, pp. 411-418, 2010, doi: 10.1109/TSM.2010.2050080.
[94] S. M. Sze, *Semiconductor devices: physics and technology*. John wiley & sons, 2008.
[95] A. Microsemiconductor, "Germanium Diodes," 2017. [Online]. Available: https://www.americanmicrosemi.com/tutorial/germanium-diodes/.
[96] L. A. M. Sulmoni, "Static and dynamic characteristics of InGaN-based laser diodes," EPFL, 2014.
[97] G. Howland, "Photodetectors - Photonic Integrated Circuits 1," Presentation 2020. [Online]. Available: https://drive.google.com/file/d/1VQ_3bUkSwCiF0AKkrtkAKwA5DXETq3GG/view.
[98] I. Explore, "Junichi Nishizawa," 2021. [Online]. Available: https://ieeexplore.ieee.org/author/37285121500.
[99] S. O. Kasap, "Optoelectronics and Photonics: Principles and Practices, Second Edition," 2013.
[100] B. Van Zeghbroeck, "Principles of semiconductor devices," *Colarado University,* vol. 34, 2004.
[101] O. Optoelectronics, "Photodiode Characteristics and Applications," Application Note 2006. [Online]. Available: http://www.osioptoelectronics.com/application-notes/an-photodiode-parameters-characteristics.pdf.
[102] E. M. Hussein, *Radiation mechanics: Principles and practice*. Elsevier, 2010.
[103] I. Institute. "Si Band Structure and Carrier Concentration." http://www.ioffe.ru/SVA/NSM/Semicond/Si/bandstr.html#Basic (accessed 2021).
[104] I. Institute, "Ge Band Structure and Carrier Concentration." [Online]. Available: http://www.ioffe.ru/SVA/NSM/Semicond/Ge/bandstr.html.
[105] D. J. Lockwood and L. Pavesi, "Silicon fundamentals for photonics applications," *Silicon Photonics,* pp. 1-50, 2004.
[106] Thorlabs, "Relationship Between Rise Time and Bandwidth for a Low-Pass System," Technical Resource 2020. [Online]. Available: https://www.thorlabs.com/newgrouppage9.cfm?objectgroup_id=9817.
[107] G. Živanović, "Design considerations for Ge-on-Si waveguide photodetector," Massachusetts Institute of Technology, 2014.
[108] S. M. Sze, Y. Li, and K. K. Ng, *Physics of semiconductor devices*. John wiley & sons, 2021.
[109] C. Hu, *Modern semiconductor devices for integrated circuits*. Prentice Hall Upper Saddle River, NJ, 2010.
[110] R. Kapoor, "Gate Graduate Aptitude Test in Engineering Electronics & Communication Engineering," 2020.
[111] S. Laboratories, "Converting Resistivity to Carrier Concentration," Technical Note 2021. [Online]. Available: http://www.solecon.com/sra/rho2cc.htm.
[112] K.-W. Ang, J. W. Ng, G.-Q. Lo, and D.-L. Kwong, "Impact of field-enhanced band-traps-band tunneling on the dark current generation in germanium p-i-n photodetector," *Applied Physics Letters,* vol. 94, no. 22, p. 223515, 2009.
[113] M. Takenaka, K. Morii, M. Sugiyama, Y. Nakano, and S. Takagi, "Dark current reduction of Ge photodetector by GeO 2 surface passivation and gas-phase doping," *Optics express,* vol. 20, no. 8, pp. 8718-8725, 2012.

[114] H. Chen *et al.*, "Dark current analysis in high-speed germanium pin waveguide photodetectors," *Journal of Applied Physics,* vol. 119, no. 21, p. 213105, 2016.
[115] D. Ahn, L. C. Kimerling, and J. Michel, "Efficient evanescent wave coupling conditions for waveguide-integrated thin-film Si/Ge photodetectors on silicon-on-insulator/germanium-on-insulator substrates," *Journal of Applied Physics,* vol. 110, no. 8, p. 083115, 2011.
[116] O. Optoelectronics, "Optical Communication Photodiodes and Receivers," Application Note 2021.
[117] E. Säckinger, *Broadband circuits for optical fiber communication*. John Wiley & Sons, 2005.
[118] M. Integrated, "Optical Signal-to-Noise Ratio and the Q-factor in Fiber-Optic Communication Systems," Application Note 2008.
[119] D. Knipp, "Optical Signal to Noise Ratio (OSNR)," Presentation 2005. [Online]. Available: https://optiwave.com/wp-content/uploads/2015/10/TC-Optical-Signal-to-Noise-Ratio-OSNR.pdf.
[120] M. Barnoski and S. Jensen, "Fiber waveguides: a novel technique for investigating attenuation characteristics," *Applied optics,* vol. 15, no. 9, pp. 2112-2115, 1976.
[121] S. Stopiński, K. Anders, S. Szostak, and R. Piramidowicz, "Optical Time Domain Reflectometer Based on Application Specific Photonic Integrated Circuit," in *The European Conference on Lasers and Electro-Optics*, 2019: Optical Society of America, p. ch_p_38.
[122] G. Bolognini, J. Park, M. A. Soto, N. Park, and F. Di Pasquale, "Analysis of distributed temperature sensing based on Raman scattering using OTDR coding and discrete Raman amplification," *Measurement Science and Technology,* vol. 18, no. 10, p. 3211, 2007.
[123] Y. Koyamada, M. Imahama, K. Kubota, and K. Hogari, "Fiber-optic distributed strain and temperature sensing with very high measurand resolution over long range using coherent OTDR," *Journal of Lightwave Technology,* vol. 27, no. 9, pp. 1142-1146, 2009.
[124] G. Tu, X. Zhang, Y. Zhang, F. Zhu, L. Xia, and B. Nakarmi, "The Development of an $\Phi $-OTDR System for Quantitative Vibration Measurement," *IEEE Photonics Technology Letters,* vol. 27, no. 12, pp. 1349-1352, 2015.
[125] L. Zhou *et al.*, "Distributed strain and vibration sensing system based on phase-sensitive OTDR," *IEEE Photonics Technology Letters,* vol. 27, no. 17, pp. 1884-1887, 2015.
[126] S. Mikhailov, L. Zhang, T. Geernaert, F. Berghmans, and L. Thévenaz, "Distributed hydrostatic pressure measurement using Phase-OTDR in a highly birefringent photonic crystal fiber," *Journal of Lightwave Technology,* vol. 37, no. 18, pp. 4496-4500, 2019.
[127] M. R Fernández-Ruiz, L. Costa, and H. F Martins, "Distributed acoustic sensing using chirped-pulse phase-sensitive OTDR technology," *Sensors,* vol. 19, no. 20, p. 4368, 2019.
[128] Z. Wang *et al.*, "Distributed acoustic sensing based on pulse-coding phase-sensitive OTDR," *IEEE Internet of Things Journal,* vol. 6, no. 4, pp. 6117-6124, 2018.
[129] JDSU, "Reference Guide to Fiber Optic Testing," Guide vol. Second Edition, Volume 1.
[130] X. Liu, B. Jin, Q. Bai, Y. Wang, D. Wang, and Y. Wang, "Distributed fiber-optic sensors for vibration detection," *Sensors,* vol. 16, no. 8, p. 1164, 2016.

[131] K. Miah and D. K. Potter, "A review of hybrid fiber-optic distributed simultaneous vibration and temperature sensing technology and its geophysical applications," *Sensors,* vol. 17, no. 11, p. 2511, 2017.
[132] J. E. Bowers, M. Piels, A. Ramaswamy, and T. Yin, "High Power Waveguide Ge/Si Photodiodes," *ECS Transactions,* vol. 33, no. 6, p. 729, 2010.
[133] D. R. J. G. J. Rydning, "The digitization of the world from edge to core," *Framingham: International Data Corporation,* 2018.
[134] H. Li, G. Balamurugan, J. Jaussi, and B. Casper, "A 112 Gb/s PAM4 linear TIA with 0.96 pJ/bit energy efficiency in 28 nm CMOS," in *ESSCIRC 2018-IEEE 44th European Solid State Circuits Conference (ESSCIRC)*, 2018: IEEE, pp. 238-241.
[135] J. D'Ambrosia, "IEEE P802. 3bs baseline summary," in *IEEE P802. 3bs 400GbE Task Force*, 2015.
[136] A. Ghiasi, "400GBase-LR8: A proposal for 10 km objective Using 50 Gb/s PAM4 Signaling," *IEEE P802. 3bs 400GbE Task Force,* 2015.
[137] Accton, "The New World of 400 Gbps Ethernet," 2021. [Online]. Available: https://www.accton.com/Technology-Brief/the-new-world-of-400-gbps-ethernet/.
[138] Keysight, "Using Eye Diagrams," 2020. [Online]. Available: https://na.support.keysight.com/plts/help/WebHelp/Analyzing/Analyzing_Data_using_Eye_Diagrams.html.
[139] G. N. Brian Welch, Keith Conroy, Jeff Maki, David Lewis, "400G-PSM4: A Proposal for the 500m Objective using 100 Gb/s per Lane Signaling," 2015. [Online]. Available: https://www.ieee802.org/3/bs/public/15_07/welch_3bs_01a_0715.pdf.
[140] E. O. Solutions, "400G-QSFP-DD-500," 2021. [Online]. Available: https://edgeoptic.com/products/400g-qsfp-dd/400g-qsfp-dd-500/.
[141] L. Virot *et al.*, "High-performance waveguide-integrated germanium PIN photodiodes for optical communication applications," *Photonics Research,* vol. 1, no. 3, pp. 140-147, 2013.
[142] H. Guo, "Electrical Properties of Junction Structure in Silicon Devices," University of Pittsburgh, 2018.
[143] imec, "Library Handbook," 2020.
[144] T. F. O. A. Inc., "Reference Guide," 2021. [Online]. Available: https://www.thefoa.org/tech/ref/testing/test/dB.html.
[145] M. Khaouani, H. Bencherif, Z. Kourdi, L. Dehimi, A. Hamdoune, and M. Abdi, "An ultrafast multi-layer Graphene/InGaAs/InAlAs/InAs PIN photodetector with 100 GHz bandwidth," *Optik,* vol. 227, p. 165429, 2021.
[146] K. Kato, "Ultrawide-band/high-frequency photodetectors," *IEEE transactions on Microwave Theory and Techniques,* vol. 47, no. 7, pp. 1265-1281, 1999.
[147] B. M. Onat, M. Gokkavas, E. Ozbay, E. Ata, E. Towe, and M. Unlu, "100-GHz resonant cavity enhanced Schottky photodiodes," *IEEE Photonics technology letters,* vol. 10, no. 5, pp. 707-709, 1998.
[148] A. Beling, H.-G. Bach, G. G. Mekonnen, R. Kunkel, and D. Schmidt, "Miniaturized waveguide-integrated pin photodetector with 120-GHz bandwidth and high responsivity," *IEEE Photonics Technology Letters,* vol. 17, no. 10, pp. 2152-2154, 2005.
[149] J. Gosciniak and M. Rasras, "High-bandwidth and high-responsivity waveguide-integrated plasmonic germanium photodetector," *JOSA B,* vol. 36, no. 9, pp. 2481-2491, 2019.

[150] Q. Ding, S. Sant, and A. Schenk, "Design strategy for monolithically integrated photodetector and improvement using plasmonics," in *2019 International Conference on Numerical Simulation of Optoelectronic Devices (NUSOD)*, 2019: IEEE, pp. 155-156.
[151] M. Gould, T. Baehr-Jones, R. Ding, and M. Hochberg, "Bandwidth enhancement of waveguide-coupled photodetectors with inductive gain peaking," *Optics express,* vol. 20, no. 7, pp. 7101-7111, 2012.
[152] H. T. J. Meier, "Design, characterization and simulation of avalanche photodiodes," ETH Zurich, 2011.
[153] P. Vines *et al.*, "High performance planar germanium-on-silicon single-photon avalanche diode detectors," *Nature communications,* vol. 10, no. 1, pp. 1-9, 2019.
[154] Q. Ding, S. Sant, and A. Schenk, "Scaling Effects on the Plasmonic Enhancement of Butt-Coupled Waveguide Photodetectors," in *2020 International Conference on Numerical Simulation of Optoelectronic Devices (NUSOD)*, 2020: IEEE, pp. 29-30.
[155] J. Cui, T. Li, F. Yang, W. Cui, and H. Chen, "The dual-injection Ge-on-Si photodetectors with high saturation power by optimizing light field distribution," *Optics Communications,* vol. 480, p. 126467, 2021.
[156] S. Cho, S. S. Cheung, Y. H. Jung, S.-K. Kang, and B.-G. Park, "Ge-on-Si Photodetector with Enhanced Optical Responsivity by Advanced Metallization Geometry," *JOURNAL OF SEMICONDUCTOR TECHNOLOGY AND SCIENCE,* vol. 20, no. 4, pp. 366-371, 2020.
[157] X. Luo *et al.*, "Ultrasensitive flexible broadband photodetectors achieving pA scale dark current," *npj Flexible Electronics,* vol. 1, no. 1, p. 6, 2017/10/16 2017, doi: 10.1038/s41528-017-0005-x.
[158] A. Mondal, M. K. Yadav, S. Shringi, and A. Bag, "Extremely low dark current and detection range extension of Ga2O3 UV photodetector using Sn alloyed nanostructures," *Nanotechnology,* vol. 31, no. 29, p. 294002, 2020/05/01 2020, doi: 10.1088/1361-6528/ab82d4.
[159] I. Åberg *et al.*, "A low dark current and high quantum efficiency monolithic germanium-on-silicon CMOS imager technology for day and night imaging applications," in *2010 International Electron Devices Meeting*, 2010: IEEE, pp. 14.4. 1-14.4. 4.
[160] M. Maksimovic, "Quantum dot infrared photodetector as an element for free-space optics communication systems," in *Proceedings of the Xi Telekomunikacioni Forum Telfor, Beograd, Sava Centar*, 2003, pp. 25-27.
[161] L. Augel *et al.*, "Optofluidic sensor system with Ge PIN photodetector for CMOS-compatible sensing," *Microfluidics and Nanofluidics,* vol. 21, no. 11, pp. 1-5, 2017.
[162] X. Wang and J. Liu, "Step-coupler for efficient waveguide coupling to Ge/Si avalanche photodetectors," *IEEE Photonics Technology Letters,* vol. 23, no. 3, pp. 146-148, 2010.
[163] K. F. Mak and J. Shan, "Photonics and optoelectronics of 2D semiconductor transition metal dichalcogenides," *Nature Photonics,* vol. 10, no. 4, pp. 216-226, 2016/04/01 2016, doi: 10.1038/nphoton.2015.282.
[164] Y. Zhang *et al.*, "Direct observation of a widely tunable bandgap in bilayer graphene," *Nature,* vol. 459, no. 7248, pp. 820-823, 2009/06/01 2009, doi: 10.1038/nature08105.

[165] P. O'Brien, L. Carrol, C. Eason, and J. S. Lee, "Packaging of Silicon Photonic Devices," in *Silicon Photonics III: Systems and Applications*, L. Pavesi and D. J. Lockwood Eds. Berlin, Heidelberg: Springer Berlin Heidelberg, 2016, pp. 217-236.
[166] J. S. Lee *et al.*, "Meeting the Electrical, Optical, and Thermal Design Challenges of Photonic-Packaging," *IEEE Journal of Selected Topics in Quantum Electronics,* vol. 22, no. 6, pp. 409-417, 2016, doi: 10.1109/JSTQE.2016.2543150.
[167] H. Chen, L. Su, M. Jiang, and X. Fang, "Highly desirable photodetectors derived from versatile plasmonic nanostructures," *Advanced Functional Materials,* vol. 27, no. 45, p. 1704181, 2017.
[168] A. Shevlyagin, D. Goroshko, E. Chusovitin, and N. Galkin, "VIS-NIR-SWIR multicolor avalanche photodetector originating from quantum-confined Stark effect in Si/β-FeSi2/Si structure," *Applied Physics Letters,* vol. 109, no. 17, p. 171101, 2016.
[169] S. R. Shriram *et al.*, "Study on inter band and inter sub-band optical transitions with varying InAs/InGaAs sub-monolayer quantum dot heterostructure stacks grown by molecular beam epitaxy," *IEEE Transactions on Nanotechnology,* vol. 19, pp. 601-608, 2020.
[170] H. Chen *et al.*, "Infrared camera using a single nano-photodetector," *IEEE Sensors Journal,* vol. 13, no. 3, pp. 949-958, 2012.
[171] C. B. Morrison, A. P. Glinz, Z. Zhu, J. H. Bechtel, S. M. Frimel, and K. P. Roenker, "Wide-area thin film metal-semiconductor-metal photodetectors for lidar applications," in *Photodetectors: Materials and Devices III*, 1998, vol. 3287: International Society for Optics and Photonics, pp. 40-47.
[172] A. A. Lisenko, G. G. Matvienko, and V. S. Shamanaev, "Evaluation of the capabilities of a SPAD photodetector for hyperspectral registration of LIF," in *25th International Symposium on Atmospheric and Ocean Optics: Atmospheric Physics*, 2019, vol. 11208: International Society for Optics and Photonics, p. 112084N.
[173] S. D. Gedney, "Introduction to the finite-difference time-domain (FDTD) method for electromagnetics," *Synthesis Lectures on Computational Electromagnetics,* vol. 6, no. 1, pp. 1-250, 2011.
[174] D. M. Sullivan, *Electromagnetic simulation using the FDTD method*. John Wiley & Sons, 2013.
[175] A. Taflove and S. C. Hagness, "Computational electromagnetics: the finite-difference time-domain method," *Artech House,* vol. 3, 2000.
[176] Lumerical, "Finite Difference Time Domain (FDTD) solver," 2021. [Online]. Available: https://support.lumerical.com/hc/en-us/articles/360034914633-Finite-Difference-Time-Domain-FDTD-solver-introduction.
[177] Lumerical, "CHARGE solver introduction," 2021. [Online]. Available: https://support.lumerical.com/hc/en-us/articles/360034917693-CHARGE-solver-introduction.
[178] Lumerical, "Circuit Simulation with INTERCONNECT," 2021. [Online]. Available: https://support.lumerical.com/hc/en-us/articles/360045467493-Introduction-to-INTERCONNECT-Circuit-Simulation-with-INTERCONNECT.
[179] Lumerical, "INTERCONNECT product reference manual," 2021. [Online]. Available: https://support.lumerical.com/hc/en-us/articles/360037304774-INTERCONNECT-product-reference-manual.

APPENDIX A: MODELLING TECHNIQUES

Running simulations is faster and less expensive than manufacturing prototypes and then taking experimental measurements, especially if findings are needed for a variety of designs. Before producing actual devices, simulations are an excellent tool to test and optimize design characteristics. Simulations can also be used to validate results achieved via experimentation. In this section, using Lumerical simulation tools for photodetector modeling is introduced. The FDTD and CHARGE solvers in the DEVICE multi-physics environment are required to simulate a photodetector. Testing the performance of a photodetector after it has been designed is essential. The INTERCONNECT circuit modeling tool is used to assess the device performance in an optical circuit.

FDTD Solver

FDTD stands for Finite-Difference Time Difference. For photonic device simulations with wavelength scale characteristics, the time-domain technique is widely used [8, 9, 19, 39]. FDTD is a time-domain approach for calculating the change of electromagnetic fields on a rectangular finite difference grid by solving Maxwell's equations [173-175]. Throughout the photodetector modelling part of this thesis, FDTD solver is used for optical calculations such as optical generation rate.

The Maxwell's equations are numerically solved in both space and time on a discrete grid, and derivatives are obtained using finite differences [173]. The FDTD approach does not make any system assumptions or approximations. Thus, simulating random structural geometries and nonlinear materials is extremely adaptable and precise [176]. Since FDTD method solves for all vector components of the electric and magnetic fields, it is a completely vectoral simulation approach. Active and passive integrated optics, liquid crystals, nanoparticles, plasmonics, OLEDs / LEDs, photonic crystals, solar cells, CMOS image sensors, and many other applications uses FDTD to create devices [176].

FDTD solves Maxwell's equations for arbitrarily complex geometries where device performance may remain unknown. In these circumstances, analytical approaches to anticipate device behavior are insufficient [174]. The FDTD approach is particularly useful for modeling devices with feature sizes that are less than or equal to wavelength

[176]. Broadband results can be acquired from a single simulation due to the time domain aspect of FDTD. Finally, because the FDTD technique scales well with parallelization, it is ideally suited for application in current multi-core and multiprocessor computers, as well as HPC clusters [176].

According to standard workflow in Lumerical FDTD, if the material data is not already present in the default material database, the first step in setting up a new simulation is to specify the materials that are used in the simulation. The structures and FDTD simulation area are all defined after the specification of materials. The boundary conditions, mesh, and simulation time are all defined in the simulation area. The light sources and recording monitors are also required to be added for the simulation. Checks should be conducted before conducting the simulation to ensure that the material characteristics are appropriately simulated, and that the computer has enough memory to perform the simulation. After the simulation is completed, the data from the monitors is gathered, and the findings may be evaluated by graphing the data directly or using additional scripts to post-process the data. All simulation processes in the design of a device can be repeated several times as the device shape changes until the best suited settings are identified. The simulation program provides a built-in parameter sweeping and optimization tool to help to automate this procedure.

FDTD Solver Physics

The finite-difference time-domain (FDTD) approach is used to solve Maxwell's equation in the time domain, as previously described. The equations are solved numerically in both space and time on a discrete grid, which means that the electric and magnetic fields, E and H, are discrete in both space and time. Maxwell's Equations in a differential form can be expressed as [173]:

Gauss's Laws:

$$\vec{\nabla} \cdot \vec{D} = \rho \qquad \vec{\nabla} \cdot \vec{B} = 0 \tag{1}$$

Faraday's Law:
$$\vec{\nabla} \times \vec{E} = -\frac{\partial \vec{B}}{\partial t} \tag{2}$$

Ampere's Law:
$$\vec{\nabla} \times \vec{H} = \vec{J} + \frac{\partial \vec{D}}{\partial t} \tag{3}$$

If the fields are discretized in time and space the equation can be represented as in follows where i and n are integers [176]:

$$\vec{E}(x,t) = \vec{E}\left(\left(i + \frac{1}{2}\right)\Delta x, \left(n + \frac{1}{2}\right)\Delta t\right) \tag{4}$$

The grid step in space is usually denoted Δx (or $\Delta y, \Delta z$) and in time as Δt. For ease of notation, instead of Δx and Δt, the spatial grid can be simply referred as i (or j, k) and the time step as n. Furthermore, it is practical to use subscript and superscript notation for the spatial position and time step where Δx and Δt are implied [176]:

$$\vec{E}\left(\left(i + \frac{1}{2}\right)\Delta x, \left(n + \frac{1}{2}\right)\Delta t\right) = \vec{E}_{i+\frac{1}{2}}^{n+\frac{1}{2}} \tag{5}$$

The electric fields are solved at time $n + \frac{1}{2}$ while the magnetic fields are solved at time n. The derivatives in both time and space are handled with finite differences and are second order accurate when the grid is uniform. Below, the finite difference derivatives on a uniform grid is given [176]:

$$\begin{aligned} \frac{\partial}{\partial t}\vec{E}^n &= \frac{\vec{E}^{n+\frac{1}{2}} - \vec{E}^{n-\frac{1}{2}}}{\Delta t} + O(\Delta t^2) \\ \frac{\partial}{\partial x}\vec{E}_i &= \frac{\vec{E}_{i+\frac{1}{2}} - \vec{E}_{i-\frac{1}{2}}}{\Delta x} + O(\Delta x^2) \end{aligned} \tag{6}$$

At the beginning of the simulation, the $\vec{E}$ and $\vec{H}$ fields are typically zero. From there, $\vec{E}$ at time $\left(n+\frac{1}{2}\right)$ is updated by the $\vec{E}$ at previous timestep plus a term proportional to the curl of $\vec{H}$ at time step n. Once the updated $\vec{E}$ field at time $\left(n+\frac{1}{2}\right)$ is obtained, then $\vec{H}$ at time $(n+1)$ can be calculated. In this way, $\vec{E}$ and $\vec{H}$ fields are updated in order until the simulation is stopped [174].

$$
\begin{gathered}
\vec{E}^{-\frac{1}{2}} = 0, \qquad \vec{H}^{0} = 0 \\
\vec{E}^{n+\frac{1}{2}} = \vec{E}^{n-\frac{1}{2}} + \frac{\Delta t}{\varepsilon} \vec{\nabla} \times \vec{H}^{n} \\
\vec{H}^{n+1} = \vec{H}^{n} - \frac{\Delta t}{\mu} \vec{\nabla} \times \vec{E}^{n+\frac{1}{2}} \\
\vec{H}^{0} \rightarrow \vec{E}^{\frac{1}{2}} \rightarrow \vec{H}^{1} \rightarrow \vec{E}^{\frac{3}{2}} \rightarrow \vec{H}^{2} \rightarrow \vec{E}^{\frac{5}{2}} \rightarrow \cdots
\end{gathered}
\tag{7}
$$

This leapfrog approach has the advantage of converging to second order accuracy in time, which means that the error between the electromagnetic fields calculated by FDTD and the correct solution scales with the time step squared [173]. Thus, if the time step is halved, the simulation error rate is reduced to one fourth.

The components of the electric and magnetic fields are spread in space across a unit cell known as the Yee cell as shown in Figure 68. Within the Yee cell, components of the E and H fields are positioned at different locations. On a uniform mesh, this allows for the computation of spatial derivatives using finite differences at the ideal spatial locations and gives second-order precision in space [173]. It is also worth noting that the E and H components are never known at the same geographic position, which might have implications for a variety of calculations, including energy density. Monitors that record these fields by default interpolate all field components to the corner of the Yee cell so that the results may be seen and analyzed in the same spatial place. This interpolation, however, may be turned off and is beneficial for advanced computations such estimating the optical absorption in a metal at a metal/dielectric contact [176].

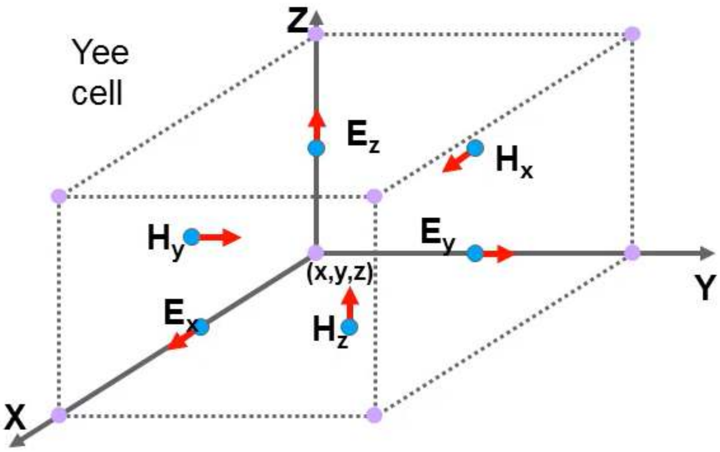

Figure 68: Yee cell representation [176].

FDTD simulations are performed in either 3D or 2D. It is important that the structure in the third dimension is limitless in 2D simulations [176]. 2D simulations can be an approximation giving a rapid result in certain circumstances.

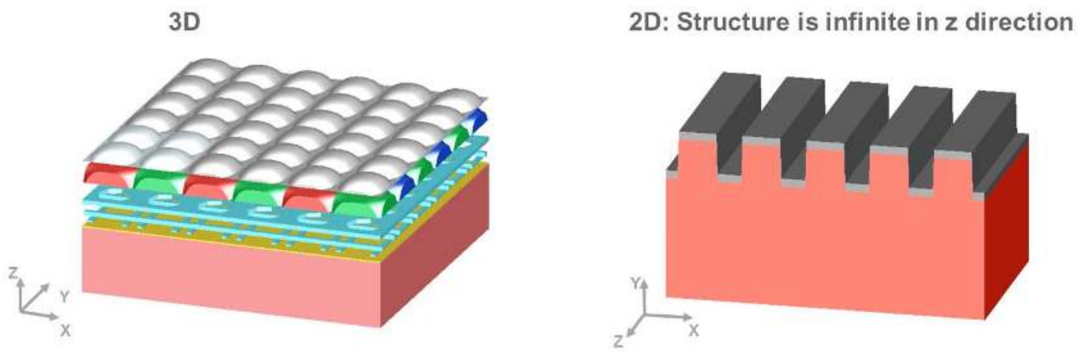

Figure 69: Example of 2D and 3D structures in FDTD simulations [176].

Simulating line gratings illuminated by plane waves, such as the one illustrated in Figure 69 is a good example for 2D simulation. The permittivity and fields are the same for all values of z in 2D FDTD simulations because the structure is infinite in the z dimension. This permits Maxwell's equations to be separated into two distinct polarization states: transverse electric (TE) with fields E_x, E_y, and H_z, and transverse magnetic (TM) with fields E_z, H_x, and H_y [176].

It is also important that as the grid size grows, so does the memory and simulation time. Assuming the spatial grid size is uniform and equal for Δx, Δy and Δz, then the memory requirements for 3D simulations scale with $(\lambda/\Delta x)^3$ and $(\lambda/\Delta x)^2$ for 2D simulations, where λ is the wavelength [173]. For 3D and 2D simulations, however, the simulation duration rises by $(\lambda/\Delta x)^4$ and $(\lambda/\Delta x)^3$, respectively [173]. This is due to the fact that reducing the spatial grid size without reducing the time step (Δt) is impossible. As a result, there is a big penalty for using too small grid step. If the grid size is halved, then the simulation time will increase by a factor of 16.

The ratio of wavelength to the grid size $(\lambda/\Delta x)$, which can also be called as number of grid points per wavelength, is a key factor determining the accuracy of the FDTD simulation [173]. As a general rule, 6 points per wavelength is adequate for many FDTD simulation results, such as transmission and reflection, to be correct with a 10 to 20 percent error rate [176]. Many results will be within 1 to 2 percent of the correct result when points per wavelength are increased up to 10, and most simulations do not require more than 20 points per wavelength. The FDTD tool from Lumerical has a basic mesh accuracy parameter that establishes a minimum number of points per wavelength in all simulation zones. It also adjusts automatically to the refractive index of different materials, because materials with a higher refractive index require a smaller grid size to keep the same precision level. The mesh accuracy ranges from 1 to 8, with targets of 6, 10, 14, 18, and so on up to 34 points per wavelength. The mesh accuracy option is set to 2 by default, which is suitable for most simulations. Increasing the mesh accuracy settings value beyond 3 or 4 is seldom effective because something else is usually limiting the simulation accuracy at that point [176].

CHARGE Solver

The charge solver is a physics-based electrical modeling tool that is used to analyze photodetectors, modulators, and image sensors in steady-state, transient, and small-signal modes. It solves the Poisson’s and drift-diffusion equations, which are used to characterize the electrostatic potential and density of free charge carriers in semiconductor devices [177]. Throughout the photodetector modelling part of this thesis, CHARGE solver is used for electrical calculations in Lumerical DEVICE tool.

CHARGE Solver Physics

Each carrier (electron or hole) in a semiconductor device moves under the influence of two opposing processes: drift owing to the applied electric field and diffusion owing to the carrier density gradient [108]. These processes are represented in the drift-diffusion equations as the sum of two terms where J_n and J_p are current densities due to electron and hole, q is unit charge, μ_n and μ_p are electron and hole mobility, E corresponds to electric field, n and p are electron and hole density, D_n and D_p are electron and hole diffusivity, ∇n and ∇p are density gradients of electron and holes, respectively.

$$J_n = q\mu_n nE + qD_n \nabla \mathrm{n}$$
$$J_p = q\mu_p pE - qD_p \nabla \mathrm{p} \tag{8}$$

The electric field must be known in order to solve the drift-diffusion equations. For the same device, the Poisson's equation may be used to calculate the electric field [177]. Poisson’s equation can be written as in below where ε is dielectric permittivity, ∇V is electrostatic potential and ρ is the net charge density.

$$-\nabla \cdot (\varepsilon \nabla V) = q\rho \tag{9}$$

In a 2D or 3D mesh grid, the CHARGE solver discretizes and solves the drift-diffusion and Poisson's equations [177]. Along the borders of materials with different physical characteristics, the simulation region is separated into various domains. Insulators, semiconductors, and conductors are the three types of materials employed in the simulations. There is a model for each type of material that specifies the charge transport behaviors of each material. Drift-diffusion equations are not solved in the insulator-conductor areas, instead, these areas serve as boundary conditions for the semiconductor domains.

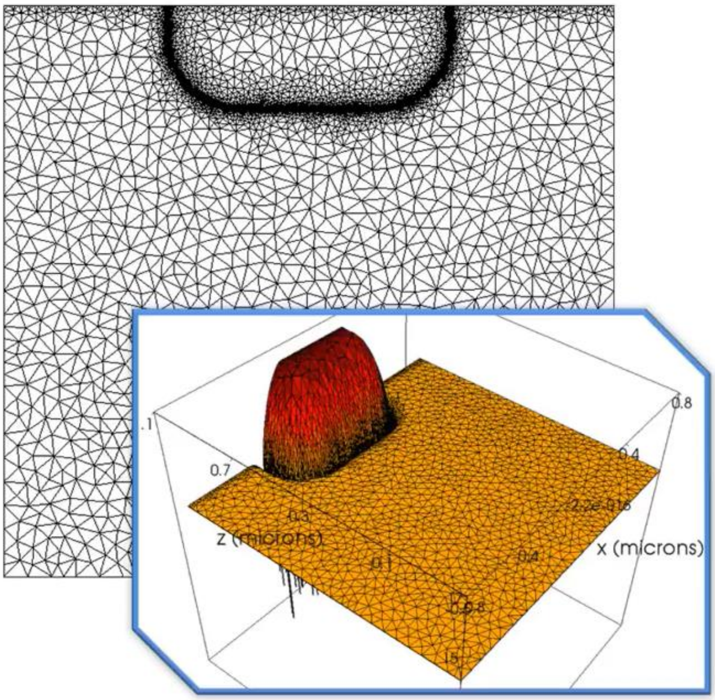

Figure 70: Finite-element mesh in the form of triangles or tetrahedra in 2D and 3D simulations [177].

In 2D and 3D simulations, the charge solver uses a finite-element mesh in the shape of triangles or tetrahedra, as illustrated in Figure 70. The physical quantities that are approximated from the discrete formulation of those equations are determined using the solution to the system of equations. At each mesh vertex, fundamental simulation characteristics including geometry, material characteristics, temperature, and electrostatic potential are determined [177]. The precise solution to the system of equations can be better approximated with a finer mesh (with shorter edge lengths and smaller components), but at a significant expense in simulation performance. The simulation time and memory needs increase as the mesh features get smaller.

Similar to FDTD, the Lumerical DEVICE tool has an automated and user-defined mesh refinement feature, which allows for accurate simulation results with minimal computing effort. Automatic mesh refinement is a feature that employs a finer mesh to resolve places more correctly when there is a quick change in attributes such as doping and heat production [177]. Figure 70 shows an example of automated mesh refinement at the edges where a rapid change in the value of a certain attribute is identified.

INTERCONNECT

The Lumerical INTERCONNECT is a photonic integrated circuit design program that allows for the time and frequency domain design, simulation, and analysis of integrated circuits, silicon photonics components, and optical interconnects [178].

The INTERCONNECT's frequency domain solver is used to calculate the overall frequency response of a circuit. This is accomplished by solving a sparse matrix which simulates the circuit as a series of linked scattering matrices, each of which reflects the frequency response of a single element. Circuit behavior is analyzed in terms of amplitude, phase, group delay, and dispersion using advanced analysis and visualization techniques [178].

The INTERCONNECT employs a data flow system simulator for time domain simulations, which provides greater flexibility than typical discrete time or time-driven simulators [179]. Each element's time domain waveform signals are calculated and bidirectionally propagated by the dynamic data flow scheduler. As shown in Figure 71, eye diagrams and figures of merit, such as the bit error rate, may be easily extracted using the analytical tools. Bi-directional and multimode circuit topologies are supported by the INTERCONNECT's frequency and time domain solvers. The optical components, such as sources and analyzers, are all available in the element library. Electrical elements for active component simulation are also included.

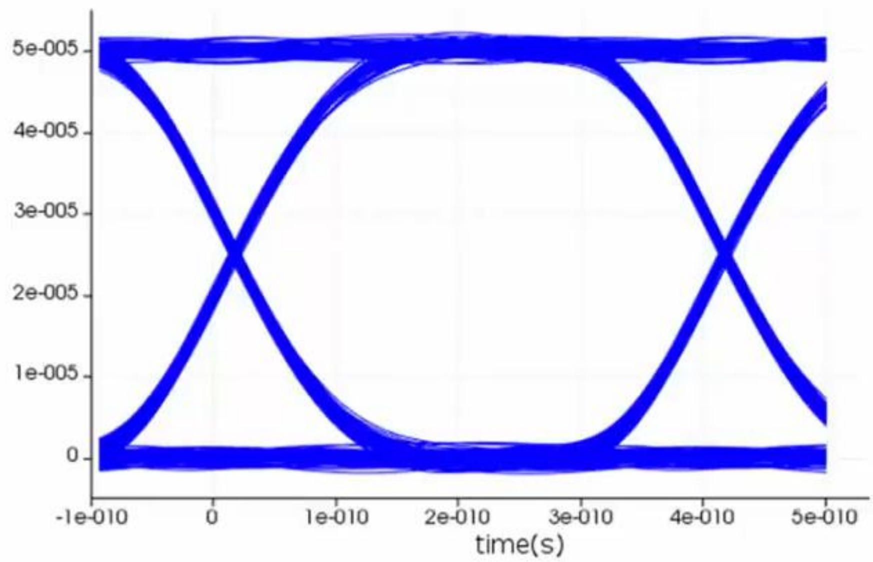

Figure 71: Eye diagram example generated by INTERCONNECT.

INTERCONNECT software is used to create, publish, and maintain compact model libraries. Both component-level simulation results and experimental data may be used to create compact models. Interoperability with Lumerical's optical, electrical, and thermal computer-aided-design (CAD) tools like FDTD and DEVICE helps with this.

Circuit Simulation Workflow

In constructing a circuit in INTERCONNECT, the fundamental workflow starts with adding schematic circuit components and specifying their attributes. For example, inserting a waveguide element and configuring its characteristics such as the length, effective index, group index, and dispersion to describe the waveguide.

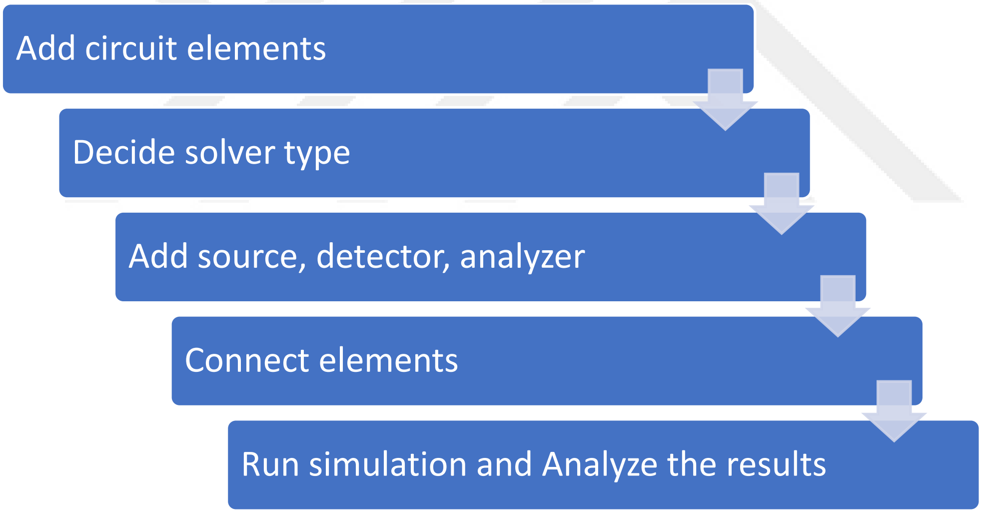

Figure 72: Basic circuit design workflow in INTERCONNECT.

Waveguides, phase shifters, splitters, and other popular generic circuit elements are added via the Element Library. The simulation procedure continues by choosing a solver type. This might be a frequency domain solver to obtain the circuit's steady-state response or a time domain solver to obtain the transient response. It is necessary to include the appropriate sources, detectors, and analyzers for the type of simulation based on the type of solver. For example, for a frequency domain simulation, using an optical network analyzer, also called an ONA, is necessary to get the transmission spectrum from a circuit, whereas for a time-domain simulation, using an oscilloscope is required to measure the output signal over time. An example circuit is shown in Figure 73.

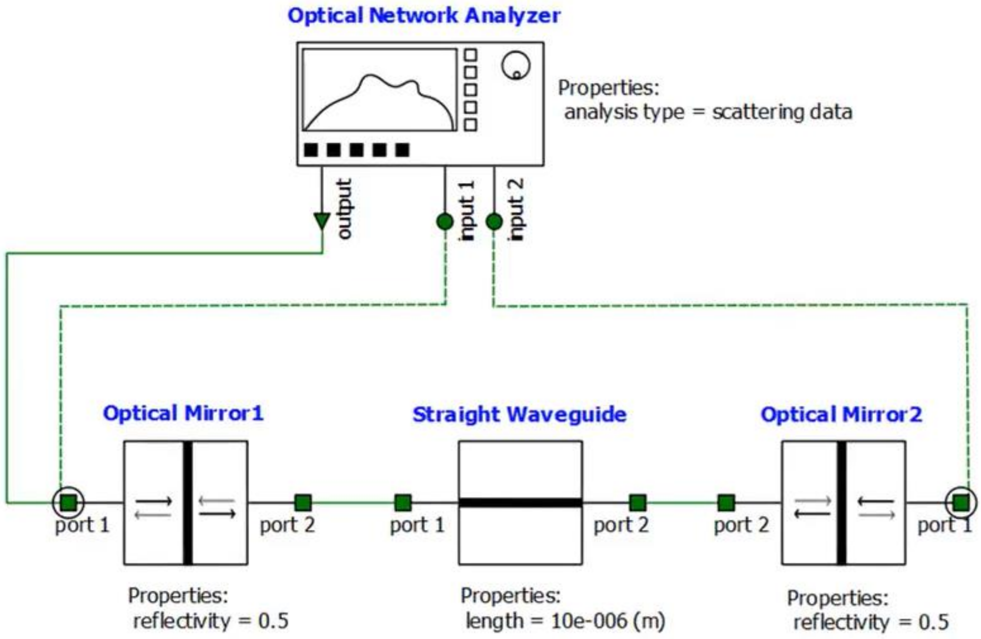

Figure 73: An example optical circuit in INTERCONNECT [179].

The simulation is performed once all of the circuit elements, sources, analyzers, and detectors have been included and the connections between them have been accurately connected in the circuit diagram. After the simulation has finished running, it is moved from layout mode to analysis mode, where analysis may be done by visualizing findings from analyzers and detectors, exporting data, and utilizing the script to gather and post-process data. Modifying the circuit design to maximize the circuit behavior is a frequent method. To do that it is required switching to layout mode to make the desired changes and running the simulation recurrently.

APPENDIX B: LUMERICAL SCRIPTS

The scripts used in this thesis can be accessed via GitHub using the web link below.

https://github.com/firatyildiz22/Ge-Detectors